Sub-diurnal methane variations on Mars driven by barometric pumping and planetary boundary layer evolution

John P Ortiz[1], Harihar Rajaram[2], Philip H. Stauffer[1], Kevin W. Lewis[2], Roger C. Wiens[3], and Dylan Robert Harp[4]

[1]Los Alamos National Laboratory (DOE)
[2]Johns Hopkins University
[3]Purdue University
[4]The Freshwater Trust

August 9, 2023

Abstract

In recent years, the Sample Analysis at Mars (SAM) instrument on board the Mars Science Laboratory (MSL) *Curiosity* rover has detected methane variations in the atmosphere at Gale crater. Methane concentrations appear to fluctuate seasonally as well as sub-diurnally, which is difficult to reconcile with an as-yet-unknown transport mechanism delivering the gas from underground to the atmosphere. To potentially explain the fluctuations, we consider barometrically-induced transport of methane from an underground source to the surface, modulated by temperature-dependent adsorption. The subsurface fractured-rock seepage model is coupled to a simplified atmospheric mixing model to provide insights on the pattern of atmospheric methane concentrations in response to transient surface methane emissions, as well as to predict sub-diurnal variation in methane abundance for the northern summer period, which is a candidate time frame for *Curiosity*'s potentially final sampling campaign. The best-performing scenarios indicate a significant, short-lived methane pulse just prior to sunrise, the detection of which by SAM-TLS would be a potential indicator of the contribution of barometric pumping to Mars' atmospheric methane variations.

Sub-diurnal methane variations on Mars driven by barometric pumping and planetary boundary layer evolution

J. P. Ortiz[1,2], H. Rajaram[2], P. H. Stauffer[1], K. W. Lewis[3], R. C. Wiens[4], D. R. Harp[5]

[1]Energy and Natural Resources Security, Los Alamos National Laboratory, Los Alamos, NM, USA
[2]Dept. of Environmental Health and Engineering, The Johns Hopkins University, Baltimore, MD, USA
[3]Dept. of Earth and Planetary Sciences, The Johns Hopkins University, Baltimore, MD, USA
[4]Earth, Atmospheric, and Planetary Sciences, Purdue University, West Lafayette, IN, USA
[5]The Freshwater Trust, Portland, OR 97205, USA

Key Points:

- Barometrically-driven atmospheric methane abundance timing controlled by fracture topology and planetary boundary layer (PBL) dynamics
- There is a lower limit to fracture density that can produce observed methane patterns
- A late morning or early evening SAM-TLS sample could constrain diurnal methane pattern and transport processes

Corresponding author: John P. Ortiz, `jportiz@lanl.gov`

Abstract

In recent years, the Sample Analysis at Mars (SAM) instrument on board the Mars Science Laboratory (MSL) *Curiosity* rover has detected methane variations in the atmosphere at Gale crater. Methane concentrations appear to fluctuate seasonally as well as sub-diurnally, which is difficult to reconcile with an as-yet-unknown transport mechanism delivering the gas from underground to the atmosphere. To potentially explain the fluctuations, we consider barometrically-induced transport of methane from an underground source to the surface, modulated by temperature-dependent adsorption. The subsurface fractured-rock seepage model is coupled to a simplified atmospheric mixing model to provide insights on the pattern of atmospheric methane concentrations in response to transient surface methane emissions, as well as to predict sub-diurnal variation in methane abundance for the northern summer period, which is a candidate time frame for *Curiosity*'s potentially final sampling campaign. The best-performing scenarios indicate a significant, short-lived methane pulse just prior to sunrise, the detection of which by SAM-TLS would be a potential indicator of the contribution of barometric pumping to Mars' atmospheric methane variations.

Plain Language Summary

One of the outstanding goals of current Mars missions is to detect and understand biosignatures (signs of life) such as methane. Methane has been detected multiple times in Mars' atmosphere by the *Curiosity* rover, and its abundance appears to fluctuate seasonally and on a daily time scale. With the source of methane on Mars most likely located underground, it is difficult to reconcile these atmospheric variations with an as-yet-unknown transport mechanism delivering the gas to the atmosphere. In this paper, we simulate methane transport to the atmosphere from underground fractured rock driven by atmospheric pressure fluctuations. We also model adsorption of methane molecules onto the surface of pores in the rock, which is a temperature-dependent process that may contribute to the seasonality of methane abundance. We simulated methane emitted from the subsurface mixing into a simulated atmospheric column, which provides insight into the sub-diurnal methane concentrations in the atmosphere. Our simulations predict short-lived methane pulses prior to sunrise for Mars' upcoming northern summer period, which is a candidate time frame for *Curiosity*'s next (and possibly final) sampling campaign.

1 Introduction

The potential presence of methane on Mars is a topic of significant interest in planetary science because of the potential for organic/microbial sources (e.g., methanogenic microbes). Since the early days of NASA's Mars Science Laboratory (MSL) mission, the Tunable Laser Spectrometer (TLS) instrument onboard *Curiosity* rover has made numerous measurements reporting methane in Mars' atmosphere (Webster et al., 2015, 2018a, 2021). Several papers (Webster et al., 2015, 2018a, 2021) document the apparent seasonality of background atmospheric methane concentrations, reporting methane levels that vary in time between 0.25 to 0.65 ppbv.

In addition to seasonal fluctuations in methane, some evidence suggests that atmospheric methane varies on a sub-diurnal time scale as well. SAM-TLS primarily conducts experiments at night due to mission operational constraints, and in fact all TLS detections of methane thus far have been from nighttime measurements. Two lone non-detections in 2019 were reported from daytime measurements (Webster et al., 2021) during northern summer at Gale crater. These daytime non-detections occurred on either side of a normal background methane value collected at night, implying a diurnal to sub-diurnal variability in atmospheric methane. Confirming and characterizing this apparent diurnal variability of methane has been highlighted by the SAM-TLS team as the next key step to understanding methane abundance and circulation at Gale crater (Webster et al., 2021; Moores, Gough, et al., 2019).

The primary goal of this work is to facilitate the science goals of ongoing and future sample collection missions by determining an optimal intra-sol timing for atmospheric sample collection on Mars. *Curiosity* is currently heading into its last northern summer (southern winter) season with a normal pace of operations. Soon, reduced electrical power in conjunction with SAM pump life will likely place limits on scientific operations. It is therefore important to maximize the scientific return of whatever remaining SAM-TLS measurements there may be, especially with regard to characterizing the apparent diurnal variability in methane. Recent models (Giuranna et al., 2019; Yung et al., 2018; Luo et al., 2021; Viúdez-Moreiras, 2021; Viúdez-Moreiras et al., 2021; Webster et al., 2018a, 2015; Pla-García et al., 2019) suggest a local source of methane within Gale crater, with circulation trapping methane at night and dissipating it during the day. Characterizing the diurnal variability of methane provides insight into the underlying mechanisms driving the methane fluctuations. The logical time of year to make relevant measurements is in the northern Summer period between solar longitude (L_s) 120-140°, coincident with the time of year of the previous measurements indicating diurnal variations. At the time of writing, this period is approaching in the months of September-October 2023, which may be the last opportunity for collecting *in situ* atmospheric methane data at Gale crater for the foreseeable future.

Running SAM-TLS experiments at strategically optimal times will improve the probability of gathering useful atmospheric data to answer key questions about methane at Gale crater. Numerical models of methane emissions and mixing within the atmosphere have the potential to inform this goal of determining ideal times to collect samples. The general consensus in the planetary science community is that if methane is present in Mars' atmosphere, its source is most likely located underground. This presents the question of how methane from deep underground can reach the surface rapidly enough to generate the observed short-term atmospheric variations. Some of the possibilities that have been proposed include: a relatively fast methane-destruction mechanism, modulation mechanisms that change the amount of free methane in the atmosphere and near-surface (e.g., regolith adsorption), and rapid transport mechanisms capable of delivering gases from depth (e.g., barometric pumping). This paper focuses on the latter two of these, and uses simulations driven by high resolution pressure and temperature data resolution and as forcing in order to provide insight on the timing of sub-diurnal methane fluxes driven by barometric pumping.

Barometric pumping is an advective transport mechanism wherein atmospheric pressure fluctuations greatly enhance vertical gas transport in the subsurface (Nilson et al., 1991). Low atmospheric pressure draws gases upwards from the subsurface, with air and tracer movement taking place primarily in the higher-permeability fractures rather than the surrounding, relatively low-permeability rock matrix (Figure 1). High atmospheric pressure pushes gases deeper into the subsurface, with some molecules diffusing into the rock matrix, in which the barometric pressure variations do not propagate efficiently. Over multiple cycles of pressure variations, this fracture-matrix exchange produces a ratcheting mechanism (Figure 1) that can greatly enhance upward gas transport relative to diffusion alone (Neeper & Stauffer, 2012a; Nilson et al., 1991; Massmann & Farrier, 1992; Takle et al., 2004; Harp et al., 2018). Barometric pumping has been studied in a variety of terrestrial contexts, such as: CO_2 leakage from carbon sequestration sites (Carroll et al., 2014; Dempsey et al., 2014; Pan et al., 2011; Viswanathan et al., 2008) and deep geological stores (Rey et al., 2014; Etiope & Martinelli, 2002), methane leakage from hydraulic fracturing operations (Myers, 2012), radon gas entry into buildings (Tsang & Narasimhan, 1992), contaminant monitoring (Stauffer et al., 2018, 2019), and radionuclide gas seepage from underground nuclear explosions and waste storage facilities (Bourret et al., 2019, 2020; Harp et al., 2020; Carrigan et al., 1996, 1997; Jordan et al., 2014, 2015; Sun & Carrigan, 2014). In the context of Mars, barometric pumping in fractures was first hypothesized as a potentially effective transport mechanism for underground methane by Etiope and Oehler (2019). Although two modeling papers (Viúdez-Moreiras et al., 2020; Klusman et al., 2022) have investigated barometric pumping in the context of methane transport on Mars, our recent paper (Ortiz et al., 2022) is, to our knowledge, the first to consider the explicit role of subsurface fractures and the ratcheting mechanism. In that paper, we demonstrated that barometric pumping in fractured rock is capable of producing significant surface fluxes of methane from depths of 200 m, and that the timing and magnitude of those fluxes was reasonably consistent with the timing of high-methane periods measured by *Curiosity*. The emphasis on timing in that paper was on reproducing the observed seasonality of surface fluxes. We highlighted in our discussion that the timing of surface fluxes could be further modulated by processes that retard gas transport and therefore included adsorption in shallow regolith to produce a more complete transport model.

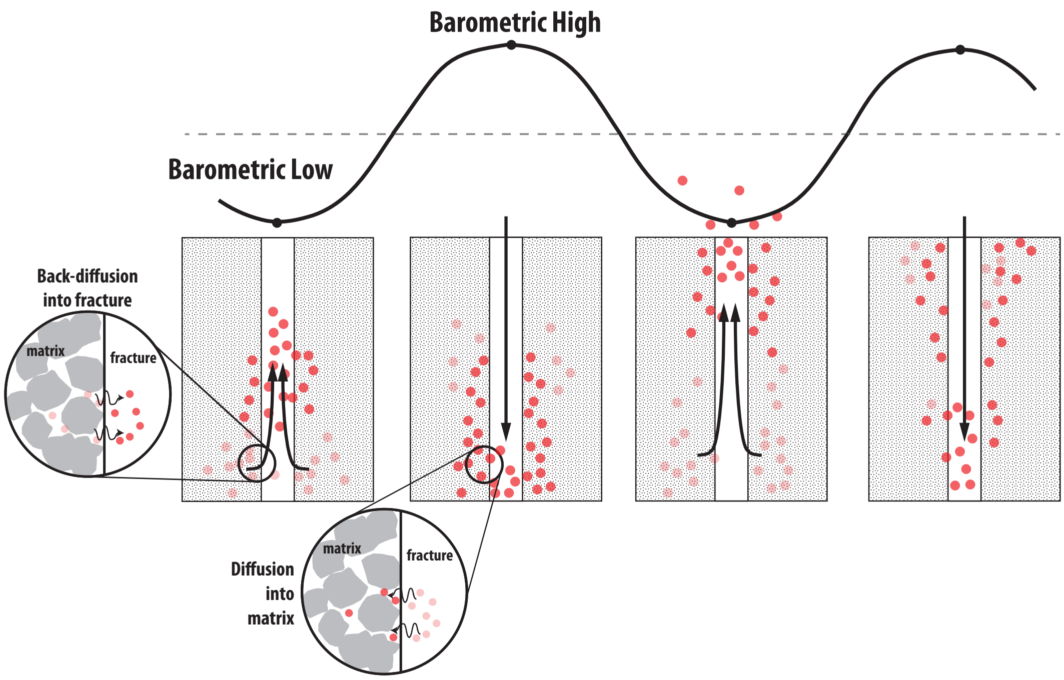

Figure 1. Schematic of the barometric pumping mechanism, which has ratcheting enhanced gas transport due to temporary immobile storage. The upward advance of the gas during barometric lows is not completely reversed during subsequent barometric highs due to temporary storage of gas tracer into rock matrix via diffusion. Adapted from Figure 1 in Harp et al. (2018).

Adsorption is a reversible phenomenon in which gas or liquid molecules (the “adsorbate”) adhere to the surface of another material (the “adsorbent”). Particle transport (e.g., methane) through porous media (e.g., martian regolith), is retarded by adsorption onto the pore walls. Adsorption is aided by adsorbents with high specific surface area, which have more sites onto which the particles can adsorb. It is believed that much of the martian regolith consists of fine mineral dust particles (Ballou et al., 1978), which have a large specific surface area (Meslin et al., 2011), making the regolith relatively amenable to adsorption. Furthermore, adsorption reactions are generally temperature-dependent, with lower temperatures favoring adsorption and higher temperatures favoring desorption. Specifically, both the rate of adsorption and the equilibrium surface coverage are higher at lower temperatures for many systems (Adamson, 1979; Pick, 1981).

Several previous papers have investigated whether the temperature dependence of regolith adsorption could explain the seasonal variations in methane in the martian atmosphere because of this temperature dependence. Work by Gough et al. (2010) used laboratory-derived constants to determine the seasonal variation of methane across Mars due to adsorptive transfer to and from the regolith. Extrapolating to martian ground temperatures, the adsorption coefficient measured for methane gas was relatively low, though the authors concluded that the mechanism could still be capable of contributing to rapid methane loss. Meslin et al. (2011) used a global circulation model to determine the seasonal variation of methane due to adsorptive transfer into and out of the regolith, finding that at Gale's latitude, this seasonal variation in methane was less than a few percent, and therefore not likely the cause of the methane fluctuations. Another paper (Moores, Gough, et al., 2019) investigated regolith adsorption, but with methane provided by a shallow (30 m) microseepage source, and found that their one-dimensional adsorptive-diffusive numerical model was able to produce the observed seasonal variation. More recently, research by Klusman et al. (2022) followed the analysis of Moores, Gough, et al. (2019) pertaining to adsorption, while also considering the role of barometric pumping as the primary transport mechanism for the shallow subsurface, and were able to produce the seasonal variation of methane when invoking high regolith permeabilities (10^{-10} m^2).

In this paper, we consider the barometrically-induced transport of a subsurface methane source to the surface that is modulated by temperature-dependent adsorption/desorption. Our two-dimensional simulations consider the explicit role of discrete, interconnected fractures in promoting advective transport, with additional seasonal modulation provided by temperature-dependent regolith adsorption. To elucidate the effects of subsurface architecture (i.e., the degree of fracturing in the rock, quantitatively represented in terms of fracture density, and defined as the ratio of fracture volume to total bulk rock volume), we simulate gas flow and transport through rocks with fracture density ranging from 0% (unfractured), to 0.035% (highly fractured). The subsurface seepage model is coupled to an atmospheric mixing model to provide insights on the pattern of atmospheric concentrations of methane in response to transient surface methane emissions, as well as to predict sub-diurnal variation in methane abundance for the northern summer season.

2 Methods: Fractured-Rock Heat and Mass Transport Simulations with Coupled Atmospheric Mixing

We used fractured-rock heat and mass transport simulations to determine the approximate timing of transient methane surface fluxes driven by barometric fluctuations throughout the Mars year. Calculations are performed within the Finite-Element Heat and Mass (FEHM) simulator, a well-tested multiphase code (Zyvoloski et al., 1999, 2021, 2017). FEHM has been used extensively in terrestrial barometric pumping studies (Stauffer et al., 2019; Bourret et al., 2019, 2020; Jordan et al., 2014, 2015; Neeper & Stauffer, 2012a, 2012b), and was previously modified by the author to adapt to conditions at Mars in a related paper examining barometric pumping of methane (Ortiz et al., 2022). We have made a simplifying assumption that there is no water in the domain, which would reduce available air-filled porosity (as ice) and cause temporary immobile storage due to phase partitioning (as liquid). Gravity and atmospheric gas properties are modified for this study to replicate Mars conditions.

Our simulations require several steps: (1) heat flow simulations to generate the subsurface temperature profiles, (2) subsurface mass flow and transport simulations of Mars air and methane driven by barometric fluctuations, with regolith adsorption terms dictated by the subsurface temperature changes from step 1, and (3) atmospheric mixing of methane emitted from the subsurface into a transient planetary boundary layer (PBL) column in order to calculate CH_4 mixing ratios.

Initial testing of a coupled energy and mass transport model indicated that due to conduction dominance (the fracture volume fraction is very small), the temperature field can be adequately described using a decoupled 1-D conductive heat transfer model. We therefore run the heat transport simulations to generate time-dependent temperature profiles with depth. We then run the 2-D, fractured-rock mass flow and transport simulations to calculate the fluxes of martian air and CH_4 driven by barometric fluctuations. The flow model assumes isothermal conditions, while the transport model considers temperature variations in its calculation of adsorption coefficients. The assumption of isothermal conditions in the flow model is justified based on verification tests, which indicated that the martian air flow properties were not significantly modified by ignoring temperature effects (Supporting Information 2.4). Mass flow and transport equations in the fractures are coupled to transport equations in the rock matrix to simulate the overall behavior of gases in fractured rock. These approaches are standard in subsurface hydrogeology – the governing equations and computational approach are described in detail below in section 2.2. Finally, we simulate the atmospheric mixing of methane by coupling the surface methane emissions to a diffusive transport model within a PBL column of time-varying height (section 2.4). This step allows us to infer atmospheric methane concentrations generated in response to the time history of surface fluxes emitted in the subsurface seepage model.

2.1 Heat Flow Model

Although the mass flow and transport simulations use a 2-D domain, we found that simple matrix conduction dominated over fracture convection, which had a negligible influence over subsurface temperatures (Supporting Information section 2.3), justifying the simulation of transient subsurface heat transport using a 1-D model. The 1-D approach also facilitates computational efficiency due to the high degree of mesh refinement required to accurately simulate subsurface temperatures (Supporting Information section 2.1). The single-phase heat conduction equation (Carslaw & Jaeger, 1959) is as follows:

$$\frac{\partial T}{\partial t} = \alpha \nabla^2 T \tag{1}$$

where T is the temperature [K], t is time [s], and α is the thermal diffusivity coefficient [$m^2\ s^{-1}$] ($\alpha = \frac{\kappa}{c\rho}$, where κ is the thermal conductivity of the material [W m^{-1} K^{-1}], c is the specific heat capacity [J K^{-1} kg^{-1}], and ρ is the density of the material [kg m^{-3}]).

We use the following subsurface heat flow properties in the heat flow model: $\kappa =$ 2.0 W m^{-1} K^{-1} (Parro et al., 2017; Klusman et al., 2022), intrinsic rock density = 2900 kg m^{-3} (Parro et al., 2017), rock specific heat capacity = 800 J $(kg \cdot K)^{-1}$ (Jones et al., 2011; Gloesener, 2019; Putzig & Mellon, 2007), geothermal gradient = 0.012908 °C m^{-1} (Klusman et al., 2022).

2.1.1 Boundary and Initial Conditions: Heat Flow Model

We prescribe an initial surface temperature of -46.93 °C (226.22 K), which is the mean surface temperature at Gale crater (Klusman et al., 2022). Ground surface temperatures fluctuate about this mean value, so this temperature is also used as the reference temperature for CO_2 properties (Mars atmosphere is 95% CO_2) in the equation of state for the mass flow model. At ground surface, we prescribe temperature as a time-varying Dirichlet boundary condition. We generated a synthetic temperature record representative of the surface temperatures collected by *Curiosity*. We extended the time series of generated temperatures so that the simulations can spin up with a sufficiently long record. At the bottom of the domain, we prescribe temperature as a constant Dirichlet boundary condition assigned based on the geothermal gradient and depth of the domain being considered.

2.2 Subsurface Mass Flow & Methane Transport Model

The flow and transport simulations are set up similarly to those presented in Ortiz et al. (2022), with some exceptions listed in the subsequent paragraph. Transient barometric pressures are prescribed at the ground surface and serve as the primary forcing condition. Methane is produced at a constant rate within a 5-m-thick zone at variable depths within the domain depending on the scenario, and is allowed to escape the subsurface domain only at the ground surface boundary.

In contrast to the simulations previously published (Ortiz et al., 2022), these simulations include the effects of temperature-dependent regolith adsorption. We model regolith adsorption as a Langmuir adsorption process, following Gough et al. (2010) and Moores, Gough, et al. (2019), described in greater detail in the following subsection (section 2.2.1). The martian air, which is $\sim 95\%$ CO_2, and the tracer gas (methane, CH_4) have properties consistent with the mean ambient pressure and temperature conditions at Gale crater.

As in the heat flow model, we extracted the dominant frequency and amplitude components of the barometric pressure record collected by the *Curiosity* Mars Science Laboratory Rover Environmental Monitoring Station (MSL-REMS; `https://pds.nasa.gov/`) using Fourier analysis. We then generated a synthetic barometric pressure record using these components, which allows us to treat the problem in a more general way while extending the time series of the pressure forcing to achieve cyclical steady-state in the surface fluxes.

2.2.1 Governing Equations and Boundary Conditions

Flow The governing flow equations for single-phase flow of martian air in the fracture network are given by:

$$b\frac{\partial \rho}{\partial t} + \nabla \cdot (\rho \vec{Q}_f) = \sum (-\rho \vec{q} \cdot \vec{n})_{\mathrm{I}}, \text{ where} \tag{2}$$

$$\vec{Q}_f = -\frac{b^3}{12\mu}\nabla(P_f + \rho g z) = -\frac{b k_f}{\mu}\nabla(P_f + \rho g z) \tag{3}$$

where ∇ is the 2-D gradient operator (operating in the fracture plane), ρ is the air density [kg m^{-3}], t is time [s], $\vec{Q}_f$ is the in-plane aperture-integrated fracture flux [m^2 s^{-1}], $\vec{q}$ is the volumetric flux [m^3/(m^2 s)] of air in the rock matrix, $\vec{n}$ denotes the normal at the fracture-matrix interfaces pointing out of the fracture (I), b is the fracture aperture [m], μ is the dynamic viscosity of air [Pa s], P_f is air pressure within the fracture [Pa], k_f is fracture permeability [m^2], g is gravitational acceleration [m s^{-2}], and z is elevation [m]. The right-hand side of (2) represents the fluxes across the fracture-matrix interface, where positive $\vec{q}\cdot\vec{n}$ is flux into the fracture. Note that (2) is an aperture-integrated two-dimensional equation for fracture flow and (3) is the local cubic law for laminar fracture flow (Zimmerman & Bodvarsson, 1996).

Governing equations for flow in the matrix are given by:

$$\phi\frac{\partial \rho}{\partial t} + \nabla \cdot (\rho \vec{q}) = 0, \text{ where} \tag{4}$$

$$\vec{q} = -\frac{k_m}{\mu}\nabla(P_m + \rho g z) \tag{5}$$

where ∇ is the 3-D gradient operator, ϕ is the porosity [– ; m^3/m^3], k_m is matrix permeability [m^2], and P_m is the air pressure in the rock matrix [Pa]. Note that $P_f = P_m$ on the fracture-matrix interface (I), and the pressure gradients ∇P_m at the fracture-matrix interface control the right-hand side of (2). We make the assumption that the bulk movement of air through the rock matrix behaves according to Darcy's law (5). In the case of a low-permeability rock matrix, the pressure gradients and fluxes induced in the matrix by barometric pressure variations are typically small.

Transport The governing equations for transport of a tracer gas (e.g., methane) in a fracture are given by:

$$b\frac{\partial(\rho C_f)}{\partial t} + \nabla \cdot (\rho \vec{Q}_f C_f) - \nabla \cdot (b\rho D \nabla C_f) = \sum \left[(-\rho \vec{q} C_m + k_{eq}\phi\rho D \nabla C_m) \cdot \vec{n}\right]_{\mathrm{I}} + \dot{m}_f \quad (6)$$

where C_f and C_m are tracer concentrations [mol kg_{air}^{-1}] in the fracture and matrix, respectively; D is the molecular diffusion coefficient of the tracer [$\mathrm{m}^2\ \mathrm{s}^{-1}$]; k_{eq} is the Langmuir equilibrium distribution coefficient; $\vec{n}$ is the normal at the fracture-matrix interfaces pointing out of the fracture (I); and $\dot{m}_f$ is the tracer source in the fracture plane [mol $\mathrm{m}^{-2}\ \mathrm{s}^{-1}$]. The first term on the right-hand side of (6) represents the tracer mass fluxes across the fracture-matrix interfaces. Note that the mass fluxes across fracture-matrix interfaces include advective and diffusive fluxes. Even in the absence of significant air flow in the matrix, diffusive flux exchanges between the fracture and matrix persist and are included in our formulation.

Governing equations for transport in the rock matrix with adsorption are given by:

$$\phi\frac{\partial \rho C_m}{\partial t}\left[1 + \frac{(1-\phi)\rho_r s_{max} k_{eq}}{(1 + k_{eq}C_m)^2}\right] + \nabla \cdot (\rho \vec{q} C_m) - \nabla \cdot (k_{eq}\phi\rho D \nabla C_m) = \dot{m}_m \quad (7)$$

where ρ_r is the rock density [kg m^{-3}], s_{max} is the maximum adsorptive capacity of the adsorbent [$\mathrm{kg}_{CH_4}/\mathrm{kg}_{rock}$], k_{eq} is the Langmuir equilibrium distribution coefficient, and $\dot{m}_m$ is the tracer source in the matrix [mol $\mathrm{m}^{-3}\ \mathrm{s}^{-1}$], and $C_f = C_m$ on the fracture-matrix interface. The distribution coefficient k_{eq} is temperature-dependent, and its formulation in the model is described in more detail in section 2.2.1.

Boundary and Initial Conditions The flow and transport simulations use martian air ($\sim$ 95% CO_2) and methane properties consistent with the mean surface temperature at Gale crater (-46.93°C). The bottom of the domain is a no-flux boundary. The left and right lateral boundaries are no-flux boundaries. The top/surface boundary is forced by the synthetic barometric pressure record we generated using frequency and amplitude components representative of the pressure record collected by MLS-REMS (see Supporting Information section 1). Vapor-phase methane and martian air are allowed to escape the domain from the top boundary. We prescribe a continuous methane production rate (9.6×10^{-7} mg CH_4 m^{-3} sol^{-1}) within a 5-m-thick zone at the bottom spanning the lateral extent of the domain (Figure 2a). This rate is consistent with measurements of methanogenic microbes at depth in Mars-analog terrestrial settings (Onstott et al., 2006; Colwell et al., 2008) in addition to liberal estimates of the maximum methane production rate by serpentinization reactions on Mars (Stevens et al., 2015). Our model assumes direct source rock-to-seepage pathway similar to that described in Etiope et al. (2013), rather than a source-reservoir-seepage system. We considered a range of methane source depths (labeled as "methane production zone" in Figure 2a) from 5 - 500 m below ground surface. For source depths $\leq$ 200 m, a standard 200 m depth model domain was used. For the cases with source depth 500 m, we used a model domain of depth 500 m.

The flow and transport simulations are performed in three steps: (1) initialization, (2) "spin-up", and (3) the main flow and transport runs. We initialize the flow model using a constant surface pressure for 10^8 years to create a martian air-static equilibrium gradient throughout the subsurface. This duration is chosen because it is sufficiently long; after 10^8 years, we can confidently assert that no pressure changes occur to the martian air-static gradient that develops. The initialization simulation is run without methane in the domain. We used this martian air-static pressure equilibrium as the initial state for the flow and transport simulations.

We then run a spin-up simulation lasting 50,100 sols, equivalent to 75 Mars Years (MY). The purpose of the spin-up simulation is to establish the memory of surface pressure and temperature fluctuation periodicity in the subsurface. Additionally, it allows

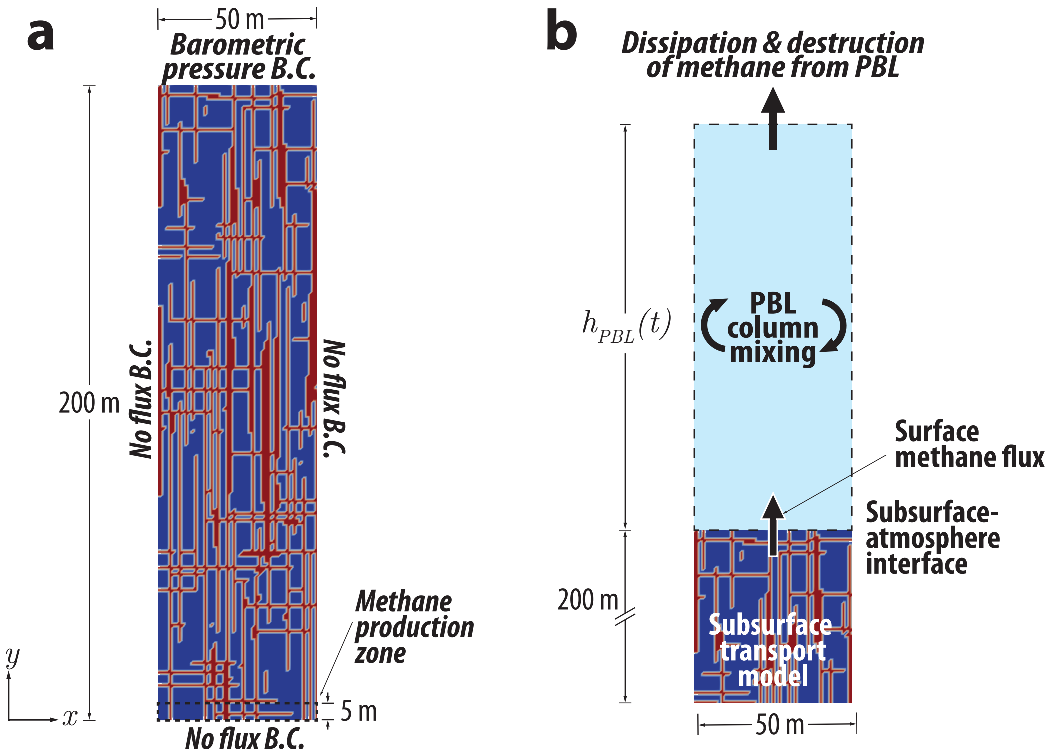

Figure 2. Schematics of model domains used in flow and transport simulations. (a) The subsurface fracture-rock flow and transport model. Fracture network generated using the Lévy-Lee algorithm. Fractures are shown in red, with rock matrix in blue. A methane source located in the methane production zone produces methane at a constant rate. (b) Schematic of the coupled subsurface-atmospheric mixing model. Methane is emitted into the atmosphere from the subsurface fractured-rock transport model. Mixing of methane occurs via 1-D vertical diffusion within the atmospheric column (light blue region), the volume of which varies seasonally and hourly based on the evolution of the planetary boundary layer (PBL) height, $h_{PBL}(t)$. The atmospheric mixing model is described in detail in section 2.4.

for the methane generated in the source zone to sufficiently populate the subsurface and reach a cyclical steady-state in terms of surface flux. We verify in each case that the system in each case has reached a cyclical steady-state equilibrium by identifying a linear trend in cumulative surface mass outflow. The domain is initially populated with a uniform concentration of methane gas ($C_0 = 9.6 \times 10^{-5}$ mol kg_{air}^{-1}) to allow the subsurface to more efficiently reach a quasi-equilibrium by pumping out excess methane from the system in the early stages of the simulation. Adsorbed methane concentration is initially zero everywhere. Finally, we run the flow and transport simulations starting from the conditions established in the initialization and spin-up runs. The final simulations are run for 75 MY, and implement the same mechanisms as the spin-up simulations.

2.2.2 Temperature-Dependent Langmuir Adsorption Model Implementation

The Langmuir adsorption isotherm can be used to adequately describe the adsorption/desorption process on Mars analogs (Moores, Gough, et al., 2019). This is partly due to the fact that for methane at the low average temperatures on Mars, the surface coverage θ (i.e., the fraction of of the adsorption sites occupied at equilibrium), is estimated to be quite low (of order 10^{-10}), so that the Brunauer-Emmett-Teller (BET) formulation is unnecessary. The equilibrium rate constant k_{eq} (ratio of sorbed phase to gas phase concentration) for the adsorption isotherm is defined as:

$$k_{eq} = \frac{s_i}{C_i} = \frac{k_a}{P_i k_d} = \frac{k_a}{C_i k_d} = \frac{R_a/(1-\theta)P_i}{R_d/P_i} \tag{8}$$

where k_{eq} is the equilibrium rate constant, s_i is the sorbed-phase concentration of tracer gas i (which in this case can be assumed to be CH_4), C_i is the concentration of the tracer gas i, k_a is the adsorption rate constant, k_d is the desorption rate constant, P_i is the partial pressure of the tracer gas, R_a and R_d are the absolute rates of adsorption and desorption, and θ is the surface coverage. The equilibrium surface coverage θ_{eq} can be approximated using the k_{eq} at a given partial pressure of methane P_{CH_4} (or concentration C_{CH4}) and temperature T:

$$\theta_{eq} = \frac{k_{eq} P_{CH_4}}{1 + k_{eq} P_{CH_4}} = \frac{k_{eq} C_{CH_4}}{1 + k_{eq} C_{CH_4}} \tag{9}$$

The equilibrium constant can be adapted to a partial-pressure basis:

$$k_{eq} = \frac{\gamma}{\eta} \frac{\nu h}{4\mathrm{ML}_{CH_4}} \left(\frac{1}{k_B T}\right)^2 \exp\left(\Delta H/RT\right) \tag{10}$$

where γ is the uptake coefficient (determined experimentally), η is the evaporation coefficient, ν is the mean molecular speed, ML_{CH_4} is the number of methane molecules per m^2 of adsorptive surface required to form a monolayer, h is Planck's constant, and k_B is Boltzmann's constant. The monolayer coverage variable ML_{CH_4} is calculated as 5.21×10^{18} molecules m^{-2} based on the size of an adsorbed methane molecule (19.18 Å) (Chaix & Dominé, 1997).

Implementation of temperature-dependent adsorption in FEHM is relatively straightforward. Because the simulation time is quite long, it is more computationally efficient to sequentially couple the temperature field to the mass flow and transport simulations. We performed several verification tests to ensure that the martian air flow properties were not significantly modified by ignoring temperature effects (Supporting Information 2.4). Using the subsurface temperatures acquired from the heat flow simulation, at each node we assign a distribution coefficient for the adsorption reaction that varies with depth and time. In this way, the flow and transport simulations are non-isothermal insofar as they account for temperature-dependent adsorption.

Gough et al. (2010) reported on the results of laboratory studies of methane adsorption onto JSC-Mars-1, a martian soil simulant, and determined the ΔH methane adsorption using experimentally determined values of the uptake coefficient (γ), which is the ratio between the adsorption rate and gas molecule collision rate. They found that the observed energy change, ΔH_{obs}, for methane adsorption onto JSC-Mars-1 is 18 ± 1.7 kJ mol^{-1}. Although not identical to the overall adsorption enthalpy, ΔH_{tot}, it is a lower limit for this process that is similar to the overall adsorption enthalpies reported by others for similar systems (Gough et al., 2010). From this, we have calculated the values of k_{eq} as it varies with temperature and tabulated them into a format usable by FEHM.

Because the surface temperature perturbations do not propagate very far into the subsurface (Figure S7), we actively calculate the time-dependent Langmuir distribution coefficient k_{eq} only for the upper 5 meters of regolith, and we assign a temporally- and spatially- constant average k_{eq} value for the remainder of the subsurface. This has the added benefit of reducing the computational costs of the simulation.

2.3 Geologic Framework and Numerical Mesh

We assigned the background rock matrix a porosity (ϕ_m) of 35%, which is in the range estimated by Lewis et al. (2019) based on consideration of the low bedrock density at Gale crater. We set the background rock permeability (k_m) to 1×10^{-14} m^2 (0.01 Darcies). This is slightly more permeable than the conservative 3×10^{-15} m^2 prescribed by previous research modeling hydrothermal circulation on Mars (Lyons et al., 2005), which is reasonable, as permeability tends to decrease with depth (Manning & Ingebritsen, 1999) and our domain (200-500 m) is much shallower than the domain considered there ($\sim$ 10 km). We assumed a fracture porosity (ϕ_f) of 100% (i.e., open fractures); we calculated fracture permeability (k_f) as $k_f = b^2/12 = 8.3 \times 10^{-8}$ m^2 assuming a fracture aperture (b) of 1 mm for all fractures in the domain. Rover photographs of bedrock fractures often show fracture apertures in the range of 1-2 cm (Figures S12, S13). However, these photographs are nearly always of fractures expressed at the planet's surface, where they are potentially exposed to freeze-thaw cycles and dehydration of the surrounding rocks, which will cause the fracture apertures to expand. These processes are not as active below the surface, so fracture apertures at depth will be comparatively narrower. Furthermore, at least in the shallow subsurface, fractures tend to be somewhat infilled by dust and/or unconsolidated material (Figure S12) such that the effective permeability of the fracture is less than that predicted by the cubic law ($k_f = \frac{b^2}{12}$, where k_f is fracture permeability [m^2]). These factors combined with the fact that lithostatic pressure, a force that tends to close fractures, increases with depth, lead us to prescribe uniform 1 mm fracture apertures as an approximate value for Mars' subsurface.

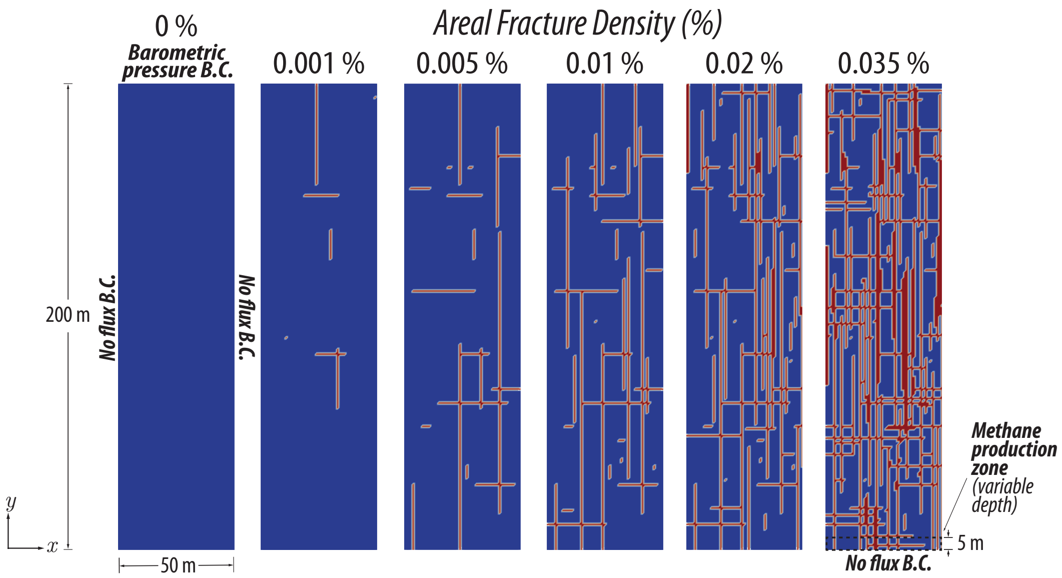

Figure 3. Schematic of the subsurface model domain showing subsurface architectures (i.e., fracture densities) used in this study.

2.3.1 Numerical Mesh and Fracture Generation Algorithm

We generated the fracture networks in our scenarios to be somewhat representative of Mars' subsurface. Because the subsurface on Mars is so poorly characterized, we estimate the fracture density (i.e., the ratio of fracture volume to bulk rock volume) based on rover photographs depicting surface expression of fracture networks at Gale crater (Figure S13) and extrapolated their distribution into the subsurface. To address the likelihood of variable subsurface architecture, we consider the following range of fracture densities: 0% (unfractured), 0.001%, 0.05%, 0.01%, 0.02%, and 0.035%, shown in Figure 3.

The model is set up in FEHM as a two-dimensional planar domain 50 m wide and with variable domain depth. For scenarios with methane source depth $\leq$200 m, we use a mesh with domain depth 200 m. For the scenario with source depth 500 m, we use a mesh of depth 500 m. The computational mesh was generated using the LANL developed software GRIDDER (`https://github.com/lanl/gridder`, 2018). Mesh discretization is uniform in the x and y directions such that $\Delta x = \Delta y = 1$ m. We randomly generated orthogonal discrete fractures using the 2-D Lévy-Lee algorithm (Clemo & Smith, 1997), a fractal-based fracture model (Geier et al., 1988) produced by random walk. An orthogonal fracture network is a general case, though it can be a reasonable assumption since in mildly deformed (i.e., less tectonically active) bedded rocks, fractures are commonly oriented nearly vertically, with either two orthogonal azimuths or a single preferred azimuth (National Research Council, 1997). The Lévy-Lee model generates a fracture network with a continuum of scales for both fracture length and spacing between fractures. A more detailed description of the algorithm can be found in Supporting Information section 6.1.

This mesh was then mapped onto a 3-D grid and extended across the width of the domain in the y direction – a single cell across – since FEHM does not solve true 2-D problems. This mapping essentially embeds the fractures in the rock matrix via upscaling of properties (see Section 2.3.2), allowing transfer of fluids and tracers to occur at the fracture-matrix interface. This mesh was then mapped onto a uniform grid.

2.3.2 Upscaling of Fracture Properties

Fractures in our model domain are embedded in the rock matrix via upscaling of permeability and porosity. Fracture permeability k_f is upscaled using:

$$k_f = \frac{b^3}{12\Delta x} \tag{11}$$

where b is the assumed fracture aperture (m) and Δx is the grid/cell block size (m). Upscaled to the grid dimensions of the numerical mesh, the modeled (effective) fracture permeability was 8.3×10^{-11} m^2. We upscale fracture porosity using a flow-weighted scheme (Birdsell et al., 2015):

$$\phi_f = \frac{b}{\Delta x} \tag{12}$$

giving a model (effective) fracture porosity of 0.001 (0.1%) at the scale of the computational grid ($\Delta x = \Delta y = \Delta z = 1$ m). The upscaled relationships (11) and (12) consistently allow the simulation of the governing equations (2 - 7) for fractures and matrix using a porous media simulator such as FEHM. This approach is widely used for simulation of flow and transport in fractured rock (Chaudhuri et al., 2013; Fu et al., 2016; Pandey & Rajaram, 2016; Haagenson & Rajaram, 2021).

2.4 Atmospheric Column Mixing Model

Methane vented from the subsurface of Mars mixes within the lower atmosphere, where it can be collected as an atmospheric sample by the SAM-TLS instrument. We simulate atmospheric mixing of methane using a one-dimensional, vertical column diffusive transport finite-difference model in order to make general observations about how the instantaneous surface flux translates to atmospheric abundance of methane (Figure 2b). The atmospheric mixing model is sequentially coupled to the subsurface model as a post-processing step. We then use an optimization routine to determine the range of atmospheric transport parameters that minimize the error of calculated CH_4 abundance compared to the SAM-TLS background measurements. This routine is performed for each fracture density case.

We represent the atmospheric mixing using a 1-dimensional vertical (z-axis) diffusive transport model (13). Surface flux from the subsurface transport model is specified as a time varying flux boundary condition in the atmospheric transport model at the ground surface ($z = 0$ m). The methane diffuses within the atmospheric column, the height of which is equal to the height of the planetary layer (PBL), which varies in thickness hourly and seasonally in 30° increments of solar longitude L_s (Newman et al., 2017).

At night, the PBL height is largely suppressed (< 300 m), approximately constant in height, and experiences relatively quiescent conditions. As the ground surface and atmosphere heats up during the day, the PBL rapidly expands to heights of several kilometers and undergoes a much greater amount of vertical mixing. In our atmospheric mixing model, we therefore conceptualize the PBL at Gale crater as belonging in either one of two states: "collapsed" or "expanded", each having its own set of atmospheric mixing parameters (Figure S10a). In this way, our approach is conceptually similar to the non-local mixing scheme formulated in Holtslag and Boville (1993), which is implemented in the GEOS-Chem model (*GEOS-Chem*, 2023; Lin & McElroy, 2010). The governing equations are as follows:

$$\frac{\partial C}{\partial t} = D_{c,e} \frac{\partial^2 C}{\partial z^2} - k_{c,e} C \tag{13}$$

where C is the atmospheric methane concentration [kg m^{-3}], t is time [s], $D_{c,e}$ is the turbulent/eddy diffusion coefficient [m^2 s^{-1}] with the subscript representing a PBL state of either c (collapsed) or e (expanded), z is the vertical coordinate [m], $k_{c,e}$ is a first-order loss term [s^{-1}]. The PBL state is defined as collapsed when $h_{PBL} < h_{thresh}$, and expanded when $h_{PBL} \geq h_{thresh}$, where h_{PBL} is the height of the PBL, and h_{thresh} is the threshold PBL height [m] marking the transition between collapsed and expanded states (chosen to be 300 m). The loss rate parameter $k_{c,e}$ in this case implicitly combines the effects of photochemical loss (assuming a lifetime of methane in Mars' atmosphere of $\sim$ 300 years; Atreya et al. (2007)) and horizontal advection away from the atmospheric column. This loss rate parameter is conceptually identical to the reciprocal of the effective atmospheric dissipation timescale (EADT) term used in the atmospheric mixing model described by Moores, Gough, et al. (2019).

The diffusive transport equation is solved numerically in Python using a backward Euler finite-difference method (FDM) scheme, which is implicit in time. The domain is discretized spatially such that $\Delta z = 1$ m, and discretized temporally such that each time step $\Delta t = 0.04$ sols. For comparison with SAM-TLS methane abundance measurements, modeled abundances are calculated everywhere and recorded at a height of $z =$ 1 m above ground surface to represent the concentration at the height of the SAM-TLS inlet (Mahaffy et al., 2012).

Computation of the transient concentration profiles is complicated slightly by the fact that the model dimensions vary in time via PBL expansion/contraction. At each time step, we modify the number of nodes based on $h_{PBL}(t)$. The methane concentration profile $C(z)$ at the previous time step is translated to the current time step as an initial condition by compressing/extending the profile in proportion to the change in column height such that mass is conserved. For example, when the model domain expands, the vertical concentration profile likewise expands, causing the maximum concentration to be reduced since the profile is spread over a larger area with mass conserved (Figure S10b). This expansion and contraction of $C(z)$ during PBL state transitions can be conceptualized as vertical advection of the tracer within the atmospheric column induced by PBL extension and collapse.

Independent of the state of the PBL (collapsed/expanded), the specified flux boundary conditions are as follow:

$$-D_{c,e}\frac{\partial C}{\partial z} = j(t) \quad \text{on } z = 0 \text{ m}, \tag{14}$$

$$-D_{c,e}\frac{\partial C}{\partial z} = 0 \quad \text{on } z = h_{PBL}(t) \tag{15}$$

where $j(t)$ is the time-varying surface mass flux emitted [kg m^{-2} s^{-1}] from the subsurface transport model, and the subscripts represent either indicate collapsed (c) or expanded (e) PBL states.

Atmospheric mixing simulations were run with a spin-up period of 3 MY in order to reach a cyclical steady-state with regard to atmospheric CH_4 abundance. Atmospheric mixing was then simulated for 1 MY, with concentrations recorded at the height of the SAM-TLS inlet ($z = 1$ m) in order to compare to background methane abundances observed by *Curiosity* (Webster et al., 2021). Simulations were set up within a differential evolution optimization routine to determine the range of atmospheric transport parameter combinations that best match the observed abundances. Error was quantified in terms of the reduced chi-squared statistic, χ^2_ν (Press et al., 2007). The parameters optimized were the diffusion coefficients for the collapsed and expanded states (D_c and D_e, respectively), as well as the methane loss terms for the collapsed and expanded states (k_c and k_e, respectively). Intuitively, we expect that $D_e \geq D_c$ since the expanded state of the PBL is characterized by increased heating and turbulent eddies, which which will tend to mix atmospheric tracers more rapidly than would conditions in the more stable collapsed state (Lin et al., 2008). Similarly, we also would expect $k_e \geq k_c$, which accounts for the fact that horizontal advection out of the atmospheric column should be greater in the expanded state than in the collapsed state. We therefore constrained the optimization routine such that:

$$\begin{aligned} 10^{-4} \leq \quad & D_c & \leq 10^{1.2} \\ 1.0 \leq \quad & D_e/D_c & \leq 1000 \\ k_{photochemical} \leq \quad & k_c & \leq 0.1 \\ 1.0 \leq \quad & k_e/k_c & \leq 10^6 \end{aligned}$$

where $k_{photochemical}$ is the assumed photochemical loss rate of 1/300 years ($\sim 10^{-10}$ s^{-1}). The collapsed-state diffusion coefficient D_c has a lower bound on the order of magnitude of free-air methane diffusion in Mars' atmosphere. This lower bound is, in fact, rather conservative, as the binary diffusivity of CH_4-CO_2 at overnight pressures (800 Pa) and temperatures (180K) at Gale crater (G. M. Martínez et al., 2017) is approximately 9.4×10^{-4} m^2 s^{-1} (Moores, King, et al., 2019). The upper bound is chosen conservatively as double the diffusion coefficient required for methane to fully mix across the depth of the PBL ($h_{PBL} \approx 250$ m when in a collapsed state) in 1 hour, which we presume to be the shortest reasonable length of time this condition could be reached. Diffusivity in the expanded state (D_e) is assumed to always be greater than or equal to D_c, with an implied maximum value of 10^4 m^2 s^{-1}. This is a conservative upper bounds considering the estimated eddy diffusivity at higher altitudes in Mars' atmosphere (30-100 km), which are of order 2×10^3 m^2 s^{-1} (Rodrigo et al., 1990) and likely greater than the average diffusivity in the lower atmosphere.

2.4.1 Non-Uniqueness of the Solution

The lack of high-frequency methane abundance data means that this problem is rather poorly constrained. In the analysis described above, we arrive at an optimal solution that minimizes error of the simulated abundances compared to the sparsely collected observations by modifying four atmospheric transport variables: D_c, D_e, k_c, and k_e. The magnitude of the eddy diffusion coefficient ($D_{c,e}$) controls how rapidly methane released from the ground surface will mix upwards across the atmospheric column, thereby diluting itself. One can intuit that for the fluxes produced in each subsurface fracture density case, there might be a range of combinations of parameter values that would produce similar annual/seasonal atmospheric abundance patterns, but that would look quite different at the diurnal time scale. We attempt to address this non-uniqueness below in order to provide a more holistic view of the potential diurnal methane abundance patterns dependent on atmospheric mixing rates.

For the fractured subsurface cases that produce the best overall fit to the observed methane abundances in the differential evolution algorithm, we analyze the surrounding parameter spaces that produce similar results with regard to overall reduced χ^2_ν value. The reduced χ^2_ν statistic is used extensively in goodness of fit testing, and has been applied previously by Moores, Gough, et al. (2019) and Webster et al. (2018b) for comparing modeled methane abundance to SAM-TLS measurements (see Press et al. (2007) for a full definition of χ^2_ν). The reduced χ^2_ν takes in the observed SAM-TLS abundance values, modeled abundance values, and the standard error of mean (SEM) uncertainties of the SAM-TLS data (Table 2 in Webster et al., 2021). A value of χ^2_ν around 1 indicates that the match between modeled values and observations is in accord with the measurement error variance (here, the SEM of SAM-TLS data). A $\chi^2_\nu \gg 1$ indicates a poor model fit, and $\chi^2_\nu > 1$ indicates that the fit does not fully capture the data variance (Bevington, 1969).

The "best" fit in each fracture density case is characterized by $\chi^2_\nu = \min \chi^2_\nu$. For a given fracture density case, we subset the simulation outcomes to the parameter combinations with error in the range: $\chi^2_\nu \leq (\min \chi^2_\nu)+0.5$. The 0.5 was arbitrarily chosen to provide a reasonable sample size of candidate solutions, and corresponds to an approximately 8% change in goodness-of-fit probability as calculated by the χ^2_ν statistic. Candidate solutions in this range therefore have similar levels of fit to the "best" scenario, and generally sample a wide range of parameter values and combinations. We then divide this parameter space into 4 scenarios: (a) lowest D_c, (b) highest D_c, (c) smallest k_e/k_c ratio, and (d) largest k_e/k_c ratio. The actual parameters used in these scenarios are detailed in Table 1. The end-member scenarios for diffusivity are conceptually similar to the transport end-members investigated by Moores, King, et al. (2019), in which they considered both a completely static, stably stratified near-surface air layer, in addition to a well-mixed near-surface air layer.

3 Results and Discussion

We present numerical simulations of transient methane flux caused by barometric pressure-pumping into Mars' atmosphere from a constant underground source. We simulated this transport mechanism acting in a range of subsurface architectures by varying the fracture density in our domain (Figure 3). We then translate methane flux (i.e., surface emissions) into atmospheric abundance (i.e., mixing ratio, in ppbv) by supplying the computed methane fluxes to the atmospheric diffusion model described in Section 2.4.

We assess our simulations by comparing their fit to MSL's observed background methane abundance fluctuations (Webster et al., 2021), which included two non-detections at mid-sol measurements in northern summer. We identify the best-fitting simulations by computing the reduced chi squared (χ^2_ν) statistic for the modeled methane abundance variation over one Mars year (L_s 0-360°). Note that the SAM-TLS measurements were taken over multiple Mars years (MY). The parameter optimization approach proceeds based on the overall χ^2_ν value (Table 1), which is calculated using all background SAM-TLS measurements. The optimization approach therefore inherently selects scenarios that best match both the seasonal and sub-diurnal variations. However, due to the paucity of measurements taken at different times of day (i.e., those that would be indicative of

Table 1. Description of parameters used in various atmospheric mixing scenarios for the three best-performing fracture densities. D_c and D_e are in units of [m^2 s^{-1}], and k_c and k_e are in units of [s^{-1}]. Scenarios are described as follows according to the parameter space discussed in section 2.4.1: (best) parameters with overall best fit to SAM-TLS data, (a) lowest D_c, (b) highest D_c, (c) smallest k_e/k_c ratio, and (d) largest k_e/k_c ratio.

Fracture Density [%]	**Scenario**	D_c	D_e	D_e/D_c	k_c ($\times 10^{-7}$)	k_e ($\times 10^{-7}$)	k_e/k_c	**Overall** χ^2_ν	**Summer** χ^2_ν	**Fig.**
0.010	Best	6.9	3186.3	460	3.68	3.72	1.01	2.18	1.19	4e, 5e
	a	0.1	33.3	380	2.63	5.56	2.11	2.61	1.44	4a, 5a
	b	10.0	5559	553	3.58	3.99	1.12	2.20	1.31	4b, 5b
	c	5.8	1081	185	4.29	4.33	1.01	2.66	4.21	4c, 5c
	d	0.5	42.6	91	2.00	6.42	3.21	2.59	1.25	4d, 5d
0.020	Best	0.4	307.2	860	4.03	4.07	1.01	3.33	12.18	S17e, S17e
	a	0.1	53.6	867	4.31	4.55	1.06	3.45	12.57	S17a, S19a
	b	1.2	981.8	852	3.61	3.67	1.01	3.61	19.29	S17b, S19b
	c	0.5	463.5	859	3.95	3.96	1.00	3.34	13.21	S17c, S19c
	d	0.2	179.4	868	3.54	5.39	1.53	3.62	10.79	S17d, S19d
0.035	Best	1.1	688.6	646	3.76	4.01	1.07	3.13	10.44	S18e, S20e
	a	0.1	60.2	590	3.58	4.18	1.17	3.33	12.67	S18a, S20a
	b	1.4	805.3	591	3.89	4.12	1.06	3.15	8.49	S18b, S20b
	c	0.2	105.7	626	3.97	4.06	1.02	3.20	8.94	S18c, S20c
	d	0.3	262.3	960	2.85	4.73	1.66	3.63	17.62	S18d, S20d

sub-diurnal methane variations), the optimization approach is more likely to select parameter combinations that more closely match the seasonal variations observed rather than the sub-diurnal variations. To address this, we pick out the fracture density cases that match the seasonality well (Overall χ^2_ν in Table 1), and examine the surrounding parameter space to observe changes in sub-diurnal methane variations that were measured in northern summer (Summer χ^2_ν in Table 1). We do not explicitly optimize the parameter space to reduce error of sub-diurnal variations in the northern summer period.

Though we investigated a range of methane source depths, because our simulations reach a cyclical steady-state, there was negligible variance in the timing of surface fluxes caused by varying source depth since the subsurface becomes equivalently populated with methane gas. Therefore, the primary source of variance in the timing of surface flux pulses was the fracture density. The best-fitting cases had a fracture density of 0.01% (Figures 4, 5), followed closely by cases with fracture density 0.035% (Figures S18, S20 and 0.02% (Figures S17, S17). The main focus of this paper is on characterizing the timing of methane variations, so the source depth does not matter for the rest of the analysis presented here. The effect of source depth would be more pronounced in the case of a source term that produces methane episodically instead of continuously, such that subsurface concentrations were not at cyclical steady-state.

For each fracture density case, the optimization algorithm arrives at a "best" solution using some combination of atmospheric transport parameters. However, due to the non-uniqueness of potential solutions generated by combinations of atmospheric transport parameters, the "best" result is often nearly indistinguishable from solutions generated by other parameter combinations in terms of error (χ^2_ν). Therefore, we investigate several atmospheric transport end-members in the candidate parameter space for each of the fracture density cases, the three best of which (fracture density 0.01, 0.02, and 0.035%) are presented in Table 1. These scenarios are described in Section 2.4.1, with parameter values detailed in Table 1. It is worth noting that the subsurface cases we investigate with low fracture density (0, 0.001, and 0.005%) produce methane abundance patterns that are almost completely out of phase with the observed abundance pattern, regardless of the choice of atmospheric transport parameters. These results are included in the Supporting Information.

As a general discussion related to evaluating the appropriateness of the modeled diffusivities, atmospheric mixing time is one metric by which we can estimate whether a given set of parameters is realistic. The approximate time required for a system to reach a fully-mixed state in response to an instantaneous point source located on a boundary (Fischer et al., 1979) is described by:

$$t_{ss} = 0.536\frac{L^2}{D} \tag{16}$$

where t_{ss} is the time [s] of full mixing (i.e., when maximum deviation from the steady-state concentration profile is $< 1\%$), L is the length of the domain [m], and D is the diffusion coefficient [m^2 s^{-1}]. Three-dimensional atmospheric modeling performed by Pla-García et al. (2019) determined that the mixing time scale for martian air within Gale crater is approximately 1 sol. Applied to the present model, this implies a collapsed-state diffusion coefficient $D_c \approx 0.4$ m^2 s^{-1} (where $L \approx 250$ m), a minimum expanded-state value of $D_e = 25.2$ m^2 s^{-1} occurring at $L_s = 130°$ (where $\max L = 2045$ m), and a maximum expanded-state value of $D_e = 219$ m^2 s^{-1} (where $\max L = 6017$ m). The implied value of D_c calculated above additionally is of the same order of magnitude as the eddy diffusion coefficient at $z = 1.3$ m estimated by G. Martínez et al. (2009). We therefore give preference in the discussion to parameter-space solutions in our mixing model that have diffusivities of similar orders of magnitude ($0.1 \leq D_c \leq 1.0$ m^2 s^{-1} and $25 \leq D_e \leq 500$ m^2 s^{-1}).

3.1 Seasonal Methane Variation

The best overall fit to SAM-TLS measurements arose in the case where fracture density was 0.01%. Several features are apparent in the abundance plots (Figure 4a-e) showing seasonal atmospheric abundance changes on Mars. Note that the gray band apparent in the plot is the result of large diurnal variations in the simulated abundance. The black line represents the night-time average abundance (calculated between 0:00 and 2:00 LMST) for the sake of visualization, since a significant majority of measurements were performed in this window. It should be noted that the error is calculated based on the simulated instantaneous methane abundance values rather than this night-time average.

Generally, the "best" fit scenario (Figure 4e) represents the seasonal methane variations well throughout the Mars year, especially the elevated abundances in northern summer (L_s 90-180°) and gradual decline in northern autumn (L_s 180-270°). However, exceptions occur in several time periods. The first occasion is from L_s 32-70°, marking the approximate middle of northern spring. Over this interval, the simulated values generally overestimate atmospheric abundance. Secondly, the simulation underpredicts abundance at $L_s \sim 216°$, in northern autumn. The difference between simulated and observed abundances at this point is less pronounced, as the simulated diurnal abundance (shown in gray) falls very nearly within one standard error of the mean (SEM) for this measurement, as indicated by the error bars on the plot. Thirdly, the simulations also underpredict atmospheric abundance at $L_s = 331°$, the middle of northern winter.

The results composite in Figure 4a-d shows the effect of the atmospheric transport end-members investigated for fracture density 0.01%. The general character of the seasonal methane abundance variation remains in each scenario, though the details vary somewhat. Scenarios with smaller D_c (such as scenarios a,d) have a greater range of diurnal abundance (grey band). Smaller D_c in general means that the mixing of methane across the depth of the atmospheric column takes longer. This allows methane concentrations near the emission surface (e.g., at $z = 1$ m, where the SAM-TLS inlet is located) to build to higher values before subsequent mixing. Scenarios with smaller D_c also seem to produce a more pronounced increase in atmospheric methane abundance during northern winter. Scenarios with higher diffusivity (e.g., scenario b) begin to approach an instantaneous mixing condition. Instantaneous mixing may be a reasonable approximation under conditions where the PBL is extremely unstable (such as during a hot, stormy day), but under most conditions it will tend to overestimate vertical mixing (Lin & McElroy, 2010). We initially used a more simplified instantaneous mixing approach similar to what done in Moores, Gough, et al. (2019), but opted for a diffusive mixing model as being more realistic of general atmospheric conditions (discussed in more detail in Supporting Information 4).

3.2 Sub-diurnal Methane Variation

With the goal of determining useful timing of SAM-TLS measurements, we also examined our simulations over shorter time scales, looking at the diurnal variations in methane abundance in northern summer (Figure 5e). Northern summer is the only season in which SAM-TLS has performed daytime enrichment method measurements, generally collected around noon (Webster et al., 2021). All other measurements have been collected close to midnight, so this is therefore the only season in which we have clues as to the possible sub-diurnal shape of methane variations. Direct observation of a sub-diurnal shape has not been possible due to instrument operational constraints of SAM-TLS, which cannot make multiple measurements on the same sol. The defining characteristic of these results (Figure 5e) is the sharp drop-off in atmospheric abundance that occurs between approximately 8:00 and 16:00 local time (LMST), which coincides with the elevated planetary boundary layer height seen in the bottom panel of the same figure. Note that we use a 24-hour time convention for the remainder of the discussion, where 0:00 - 11:59 LMST represent the morning from midnight to just before noon. In our model, the drop-off in abundance is controlled largely by the mid-day extension of PBL height, and also the generally 2-3 order of magnitude difference between D_e and D_c (Table 1). When the PBL collapses in the early evening ($\sim$17:00 LMST), it remains relatively shallow (i.e., atmospherically quiescent) through the night until early the next morning. The atmospheric mixing ratio responds accordingly by rebounding somewhat after the PBL collapse, after which point it holds relatively steady into the following morning.

The “best” scenario shown in Figure 5e generally reproduces the observed summer methane abundances. The model slightly underpredicts methane abundance relative to that observed at $L_s = 158.6°$ (yellow circle), though the modeled concentration is within one SEM of the measured value. The mid-day non-detections (L_s 120.7 and 134°) are generally captured by the model, as well as the positive SAM-TLS detection that was collected between them (L_s 126.3° at 23:56 LMST). The latter point distinguishes this case from the higher-fracture-density cases (0.035% and 0.02%), which where not able to match this intermediate observation regardless of the scenario considered (Figures S20, S19). An accurate match to the observed abundances is thus controlled by both the assumed subsurface architecture and the parameters in the atmospheric transport model.

For the case shown in Figure 5f, elevated daytime fluxes have a somewhat bimodal pattern (i.e., two primary methane flux pulses). The first occurs between 4:00 and 6:00 LMST, and has substantially greater magnitude (by a factor of 5 - 11) for the dates with non-detections (L_s = 120.7, 134°) and at L_s 158.6° than it does on the dates of the other measurements. The second primary methane pulse occurs between 15:30 and 17:00 for L_s = 103.4, 126.3, and 142.4°, and less strongly (by a factor of 1.4 - 5) between 16:00 and 18:00 for the L_s = 120.7, 134° (non-detects) and L_s = 158.6°. The timing of the

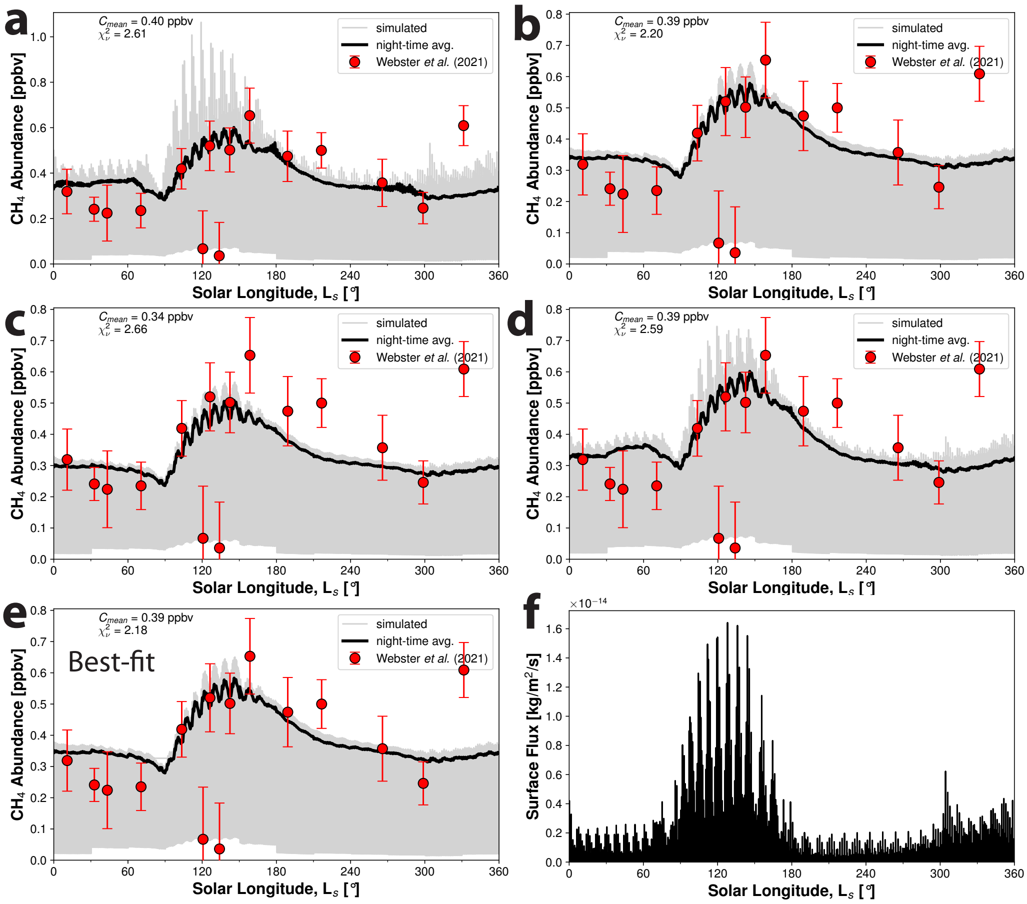

Figure 4. Composite of atmospheric mixing end-member scenarios simulating atmospheric methane abundance for the case with fracture density 0.010% showing seasonal methane variation. Panels **a-e** compare simulated (stars, lines) to measured (circles) atmospheric methane abundance values plotted against solar longitude, L_s [°]. Night-time averages of the simulated abundance (thick black line) are plotted to aid visualization because of the large diurnal variations present (gray band). Measured abundances are from Webster et al. (2021). Note that some measurements were collected in different Mars years. Panel letters **a-d** correspond to lettering of atmospheric transport parameter end-member scenarios described in Table 1 and Section 2.4.1. Panel **e** is the "best" fitting scenario (corresponds to top row in Table 1), and panel **f** is the surface methane flux.

surface flux pulses varies by fracture density case, dictated entirely by the subsurface architecture; i.e., the fracture topology. The surface flux pulses are produced in response to the small morning barometric pressure drop occurring at approximately 3:00, and the large mid-day pressure drop occurring between 7:40 and 16:00. If the subsurface were a homogeneous medium, we would expect a surface flux pulse roughly coincident with the pressure drop, having a Gaussian shape in time. This is actually observed in our model as fracture density increases: for example, in the case where fracture density = 0.035%, the surface flux has fewer individual spikes, and is characterized by a more "diffuse" flux pattern with center-of-mass near the middle of the large mid-day pressure drop (Figure S20f). The sparse fracture network in the present case (fracture density 0.01%) does not release methane at the surface in sync with the pressure drops – trace gases must work

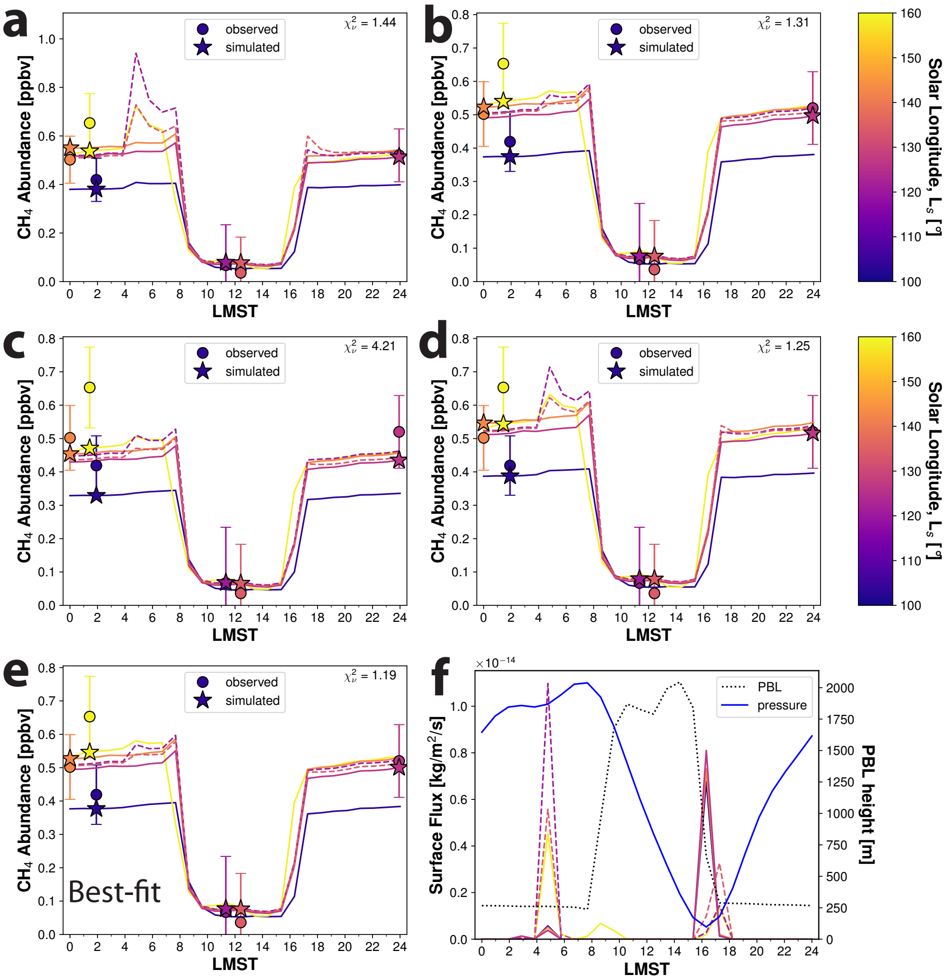

Figure 5. Composite of atmospheric mixing end-member scenarios simulating atmospheric methane abundance for the case with fracture density 0.010%. Panels **a-e** compare simulated (stars, lines) to measured (circles) atmospheric abundance values in local time, LMST, for northern summer, which highlights the day-night difference in abundance largely caused by the elevated planetary boundary layer (PBL) height h_{PBL}. Simulated abundances of the sols with non-detections are indicated by dashed lines. Measured abundances from Webster et al. (2021). Note that all measurements were taken on different sols and, in some cases, different Mars years, with the solar longitude, L_s [°] of the measurement indicated on the plot by its color. Panel letters **a-d** correspond to lettering of end-member scenarios described in Table 1 and Section 2.4.1. Panel **e** is the "best" fitting scenario (corresponds to the top row of Table 1), and panel **f** is the surface methane flux. Surface flux in local time (solid and dashed lines as above) plotted against PBL height (dotted line). Atmospheric pressure (blue line) is plotted without visible scale, but the minimum and maximum values shown are approximately 703 and 781 Pa, respectively. The pressure time series shown is from $L_s = 120.7°$; pressures on the dates of the other measurements are different but similar in shape. Comparison of derived crater mixing times (t_{ss}) calculated from D_c and D_e to estimated $t_{ss} = 1$ sol from Pla-García et al. (2019) indicate that scenarios a and d are likely to be more closely representative of actual conditions.

their way tortuously through individual fractures. The surface pressure wave propagates through the fractures and is attenuated by the rock matrix, leading to varying degrees of phase lag in the subsurface signal. Over multiple barometric pressure cycles, methane gas is brought closer to the surface through different fracture pathways – the variety of travel pathways leads to different surface breakthrough times depending on the pressure propagation and gas transport history within each fracture. This helps explain why the individual flux pulses shown in this case vary so much in magnitude despite being forced by relatively similar atmospheric pressures.

Examination of the end-member scenarios reveals some key differences imbued by the choice of atmospheric transport variables (Figure 5a-d). In terms of χ^2_ν, there is little to distinguish the end-member scenarios examined, although scenario c clearly performed worse than the rest over this time frame. Scenarios a and d used small values of D_c (of order ≤ 0.01 m^2 s^{-1}, which is on the order of magnitude implied by a 1-sol crater mixing time, and 2 orders of magnitude greater than binary CH_4-CO_2 diffusion), the effect of which is apparent in the rapid spike in methane abundance between 4:00 and 7:00 LMST. This spike is a direct result of the methane surface flux pulses occurring between 4:00 and 6:00 LMST; the smaller values of D_c cause the sensor at $z = 1$ m to more readily feel the effects of these pulses before they eventually mix by diffusion into the rest of the atmospheric column. The effect of these early morning methane pulses is greatly muted in scenarios b and c, which had much greater values for these mixing coefficients (of order ≥ 6 m^2 s^{-1}).

Considering these simulations in terms of crater mixing time (t_{ss}) of ~ 1 sol estimated by Pla-García et al. (2019) also favors the scenarios with smaller D_c. For an approximate collapsed-state PBL height of 250 m, mixing times for Table 1 scenarios are as follows: (best) 0.05 sols, (a) 4.3 sols, (b) 0.04 sols, (c) 0.07 sols, and (d) 0.75 sols. However, the collapsed state only accounts for part of each sol. The maximum diurnal PBL height during the expanded state varies from 2045 to 6017 m throughout the Mars year. For $\max h_{PBL} = 2045$ m – which occurs in northern summer – the inferred mixing time t_{ss} is: (best) 0.01 sols, (a) 0.8 sols, (b) 0.004 sols, (c) 0.14 sols, and (d) 0.28 sols. For $\max h_{PBL} =$ 6017 m – which occurs during northern winter – the inferred mixing time t_{ss} is: (best) 0.07 sols, (a) 6.56 sols, (b) 0.04 sols, (c) 1.18 sols, and (d) 2.4 sols. Scenarios a and d most closely approximate the presumed crater mixing time, though it should be noted that there can be significant variation in mixing times throughout the Mars year (Pla-García et al., 2019; Yoshida et al., 2022), and our atmospheric mixing model is not set up to account for these variations due to representing D_e with a single value.

We further interrogated the candidate solution parameter space generated by the differential optimization algorithm in order to understand the interaction between atmospheric mixing parameters, with results in Supporting Information section 7.4. Diffusion coefficients D_c and D_e, unsurprisingly, are positively correlated such that smaller D_c corresponds to a smaller D_e. The candidate solution space contains diffusion coefficient values such that range of the ratio D_e/D_c is between 59 and 678 (Figure S22), with a mean value of 351. We initially provided bounds to the algorithm for this ratio in $1 \leq D_e/D_c \leq 1000$, so the atmospheric mixing model apparently favors comparatively large daytime eddy diffusivities compared to those during the collapsed state, although the absolute magnitudes of these diffusivities do not overly affect the results in terms of error. A linear regression on $D_e = f(D_c)$ yields a slope of 10.8, with an adjusted R^2 value of 0.85. Also unsurprisingly, first-order methane loss rate parameters k_c and k_e are inversely correlated in order to preserve mass balance in time. The range of the ratio k_e/k_c is 1.01 to 3.21 (Table 1) having mean value 1.46, with the overall best scenarios in terms of error coming out of ratios close to unity. A linear regression on $k_e = f(k_c)$ yields a slope of -1.1, with an adjusted R^2 value of 0.67.

Effects of Dust Devil Pressure Drops on Flux Timing As part of making predictions about timing of atmospheric methane measurements, we also considered the effects of dust devil vortices on surface flux of methane in the vicinity of the rover. We considered this because *Curiosity* is currently climbing Aeolis Mons (a.k.a. Mt. Sharp), and will be doing so for the remainder of the mission. Observational data and Mars Weather Research and Forecasting (MarsWRF) General Circulation Model (Richardson et al., 2007) simulations of Gale crater indicate a gradual increase in vortex detections during most seasons as the *Curiosity* rover ascends the slopes of Aeolis Mons (Newman et al., 2019; Ordóñez-Etxeberria et al., 2020). The primary reason for this is related to the increase in topographic elevation, which encourages vortex formation because of the cooler near-surface daytime air temperatures (Newman et al., 2019). More discussion on this is provided in Supporting Information section 5.

We describe these dust devil simulations in the Supporting Information (section 5). We considered pressure drops associated with dust devils over a range of duration and intensity. As expected, the greatest surface flux is caused by dust devils with the longest duration (25 s) and largest pressure drop (5 Pa; Figure S11). However, the total mass of methane emitted in this scenario was 9.4×10^{-10} g, which has a negligible effect on atmospheric methane abundance in our model. Overall, dust devils likely do not make much of a difference in surface methane emissions. This makes sense, as the diurnal pressure variations by comparison have magnitude of order several 10s of Pa, with the primary pressure drop occurring over an interval of several hours. We can therefore likely ignore the effects of dust devils on overall timing of methane variations, which is encouraging since we are unable to predict the occurrence of individual vortices.

3.3 Implications for Future Measurements

Confirming and characterizing the apparent diurnal variability of methane has been highlighted by the SAM-TLS team as the next key step to understanding methane abundance and circulation at Gale crater. At the time of writing, Mars' northern summer period approaches, the timing of which is coincident with prior measurements that suggested subdiurnal methane variations (L_s 120-140°). This makes northern summer a prime candidate for potential corroboration of the hypothesized subdiurnal methane variations. The SAM wide range pumps have performed exceptionally well, and have already exceeded their flight lifetime requirements, but we need to be prudent in planning their use in future measurements. This compels the need to choose strategic sampling times in order to learn as much as possible about methane seepage and circulation patterns at Gale. Strategic atmospheric sampling using SAM-TLS during this upcoming time frame has the potential to validate and contextualize the results of our coupled subsurface-atmospheric mixing model as well as the previous measurements suggesting diurnal methane variations.

With the goal of more robustly characterizing diurnal methane variability, we would propose a set of enrichment runs in the period L_s 120-140°, which occurs September-October 2023. In the interest of conserving SAM pump life, we propose initially performing a minimum of two measurements. The first proposed measurement would establish a baseline for the second in addition to providing comparison to measurements conducted in previous MYs, while the second measurement would aim to extend the current characterization of diurnal methane variability. The measurements we propose would correspond to the approximate time of year of the previous two mid-sol samples, as well as the apparent generally-elevated methane abundance occurring in northern summer. Ideally, the samples would also be coordinated such that they coincide with TGO solar occultations on any of either 25 September, 27 September, 9 October, or 11 October 2023 for potential cross-comparison of measurements. Both enrichment runs should be performed identically to each other with the exception of local time conducted. A version of the dual-enrichment run modified slightly from the procedure of previous measurements (Webster et al., 2018a) would provide better quantification of background CH_4 and better conserve pump life without deviating significantly from previous run procedures (see Supporting Information section 3 for a more complete description of the modified procedure).

The first sample we propose should ideally be performed around L_s 126° to coincide with time-of-year of the previous MY positive detection on sol 2626, which was conducted between the two daytime non-detections in 2019 (Webster et al., 2021). This would serve as a baseline observation, both for the sake of comparison to the following measurement, as well as to the previously established baseline abundance for this period. Performing the measurement within the 23:00 - 3:00 LMST time range would make this measurement immediately comparable to most measurements from previous MYs, and additionally would refresh the baseline for the current MY and second run.

The second measurement would ideally be collected at a previously unmeasured time, and would be chosen to provide new insight into the methane emission and mixing mechanisms at play, in addition to extending the characterization of the apparent diurnal variability. We envision two primary candidate timing windows for this proposed measurement, which we hereafter refer to as I and II. Window I would take place between 6:30 - 10:00 LMST with the goal of further constraining the drop in observed methane abundance that seems to occur between midnight (0:00 LMST) and 11:20 LMST. Prior work using atmospheric transport models (Figure 8 in Viúdez-Moreiras, 2021; Moores, King, et al., 2019), in addition to the present work, predict that this drop occurs some time mid-/late-morning due to the upward extension of the PBL column and reversal of horizontal flows from convergent to divergent. A measurement in Window I would further constrain the timing of the apparent drop in methane abundance; for instance, elevated methane levels late in this window would aid the argument that PBL extension and the accompanying transition to divergent flows are strongly linked to the daytime drop in abundance. Methane abundance noticeably higher than the baseline measurement near midnight would imply additional flux in the intervening morning hours based on our model. However, if the magnitude of the difference is not overly large, it could be difficult to parse out the effects of a morning flux pulse (e.g., Figure 5a,d), gradual overnight methane accumulation, or simply sol-to-sol abundance variation.

Window II encompasses the time between 18:00-21:00 LMST, and a sample therein would serve to characterize the hypothesized rise in methane levels at sunset, post-PBL collapse (∼17:00). A measurement early in this window (18:00-19:00) could provide useful information regarding potential surface release mechanisms. If methane builds up rapidly to concentrations consistent with or above nighttime values, it could be indicative of daytime methane emissions, such as those caused by barometric pumping, though not exclusively due to this mechanism. Along that line, methane abundance noticeably greater than nighttime values (e.g., Figure S19a,d) would suggest either the occurrence of mid-/late-afternoon flux pulses, or that the magnitude of nighttime emissions is less than that estimated in other studies (or is nonexistent), both of which would also be consistent with barometric pumping. Abundances lower than observed nighttime values, on the other hand, could suggest gradual evening/overnight methane accumulation, which may point to an emission mechanism other than barometric pumping, which produces primarily daytime fluxes.

4 Conclusions

This study investigates the transport of subsurface methane in fractured rock into Mars' atmosphere driven by barometric pressure fluctuations at Gale crater. The subsurface seepage model is coupled with an atmospheric mixing model in order to simulate atmospheric concentrations within an evolving planetary boundary layer column in response to transient surface emissions and compares them to MSL abundance measurements. Atmospheric transport variables are chosen by an optimization routine such that they minimize the error compared to SAM-TLS measurements, which include seasonal and sub-diurnal abundance variations. The simulations are evaluated based on how well they represented seasonal and diurnal variations in atmospheric methane concentrations, including daytime non-detections observed by MSL. Part of the investigation involves simulating subsurface transport in rocks covering a range of fracture densities. To that end, a lower bound on subsurface fracture density of 0.01% is established, below which the seasonal atmospheric variations driven by barometric pumping are out-of-phase with observations.

We examine the sub-diurnal atmospheric methane variations produced by our simulations in Mars' northern summer, a time period chosen due to its coincidence with previous measurements suggesting the presence of large diurnal abundance fluctuations. Several key features were identified in the best-performing simulations. Simulations indicated a pre-dawn methane surface flux pulse (4:00-6:00 LMST) that may be detectable before PBL thickness increases and upslope (divergent) circulation develops. Detection of a large methane spike would be suggestive of barometric pumping, and would add to the evidence supporting a localized emission source in the interior of Gale crater, such as the highly fractured Murray outcrops as mentioned in Viúdez-Moreiras et al. (2021). Another feature identified was a large abundance depression during mid-sol between 11:00 - 17:00 coincident with PBL extension and divergent slope flows, followed by a rapid rebound in methane abundance following PBL collapse in the early evening. As a way to test our proposed transport mechanism and extend the current characterization of diurnal methane variation, we propose a set of two SAM-TLS enrichment measurements for the middle of Mars' northern summer (L_s = 120-140°), with the option of either a mid-/late-morning or an early-evening measurement. Each measurement has high potential to better-constrain the current understanding of the timing of either the apparent morning drop in methane or evolution of nighttime methane increase, respectively, and the measurements both have modest potential to incrementally suggest or refute the influence of a barometric pumping mechanism on diurnal methane variations at Gale crater.

The modeled methane abundances presented in this work are controlled by two factors: the subsurface transport pattern driven by barometric pumping and the PBL dynamics. Though driven by the same barometric signal, surface methane flux patterns in our model varied significantly with subsurface architecture (i.e., fracture density). Fracture density controls the degree to which the atmospheric pressure signal propagates into the subsurface, both in terms of overall depth and phase response. So important is the communication of the atmospheric pressures with the subsurface that cases we considered with very low fracture density ($\leq$ 0.005%) produced surface flux and abundance patterns that were almost completely out of phase with SAM-TLS observations. In our coupled atmospheric mixing model, we chose a handful of atmospheric transport parameters to approximately describe the PBL mixing dynamics, which essentially controlled the rate at which mixing from the surface methane emission would occur in the atmospheric column at different times of day. The atmospheric methane abundance was highly sensitive to these parameters, which exerted a great influence on both the seasonal and sub-diurnal abundance patterns. Despite this, our sensitivity analysis showed that no combination of atmospheric transport parameters in our model could generate abundances that were in-phase with the observed patterns for the low fracture density cases ($\leq$ 0.005%). This implies an important interplay between the influence of subsurface geology and atmospheric conditions on methane fluctuations at Gale in that only specific surface flux patterns are capable of producing the observed atmospheric variations, at least in the case where the rover is located within the emission area. Three-dimensional atmospheric dispersion modeling investigating transport from more distant emission areas, such as that in Viúdez-Moreiras et al. (2021), might be able to further contextualize the extent of this relationship.

Acknowledgments

We thank C. R. Webster and D. Lo for their comments regarding technical details of the modified dual-enrichment run procedure.

This research was supported by the Los Alamos National Laboratory (LANL) through its Center for Space and Earth Science (CSES). CSES is funded by LANL's Laboratory Directed Research and Development (LDRD) program under project number 20210528CR.

Pressure and temperature data described in the paper are further described in the supplementary materials and were acquired from NASA's Planetary Data System (PDS) at the following address: `https://atmos.nmsu.edu/PDS/data/mslrem_1001/DATA/`.

Open Research

Data Availability Statement

PDS data products from the Mars Science Laboratory (MSL) Rover Environmental Monitoring Station (REMS) were used for the analysis in this paper. The MSL REMS Models Reduced Data Record (MODRDR) provided the atmospheric pressure measurements for our simulations.

Software Availability Statement

Figures were made with Matplotlib version 3.2.2 (Hunter, 2007) available under the Matplotlib license at `https://matplotlib.org/`. The FEHM software (Zyvoloski, 2007; Zyvoloski et al., 2017) version 3.4.0 (`https://fehm.lanl.gov`) associated with this manuscript for the simulation of gas flow and transport is published on GitHub `https://github.com/lanl/FEHM/tree/v3.4.0`.

References

Adamson, A. A. (1979). *A Textbook of Physical Chemistry (Second Edition)* (Second ed.). Academic Press. doi: 10.1016/B978-0-12-044262-1.50028-1

Atreya, S. K., Mahaffy, P. R., & Wong, A. S. (2007). Methane and related trace species on Mars: Origin, loss, implications for life, and habitability. *Planetary and Space Science*, *55*(3), 358–369. doi: 10.1016/j.pss.2006.02.005

Ballou, E. V., Wood, P. C., Wydeven, T., Lehwalt, M. E., & Mack, R. E. (1978). Chemical interpretation of Viking Lander 1 life detection experiment. *Nature*, *271*(5646), 644–645. doi: 10.1038/271644a0

Bevington, P. R. (1969). *Data Reduction and Error Analysis for the Physical Sciences.* New York: McGraw-Hill.

Birdsell, D. T., Rajaram, H., Dempsey, D., & Viswanathan, H. S. (2015). Hydraulic fracturing fluid migration in the subsurface: A review and expanded modeling results. *Water Resources Research*, *51*(9), 7159–7188. doi: 10.1002/2015WR017810

Bourret, S. M., Kwicklis, E. M., Harp, D. R., Ortiz, J. P., & Stauffer, P. H. (2020). Beyond Barnwell: Applying lessons learned from the Barnwell site to other historic underground nuclear tests at Pahute Mesa to understand radioactive gas-seepage observations. *Journal of Environmental Radioactivity*, *222*, 1–14. doi: 10.1016/j.jenvrad.2020.106297

Bourret, S. M., Kwicklis, E. M., Miller, T. A., & Stauffer, P. H. (2019). Evaluating the Importance of Barometric Pumping for Subsurface Gas Transport Near an Underground Nuclear Test Site. *Vadose Zone Journal*, *18*(1), 1–17. doi: 10.2136/vzj2018.07.0134

Carrigan, C. R., Heinle, R. A., Hudson, G. B., Nitao, J. J., & Zucca, J. J. (1996). Trace gas emissions on geological faults as indicators of underground nuclear testing. *Nature*, *382*(6591), 528–531. doi: 10.1038/382528a0

Carrigan, C. R., Heinle, R. A., Hudson, G. B., Nitao, J. J., & Zucca, J. J. (1997). *Barometric Gas Transport Along Faults and Its Application to Nuclear Test-Ban Monitoring* (Tech. Rep. No. May). Lawrence Radiation Laboratory.

Carroll, S. A., Keating, E., Mansoor, K., Dai, Z., Sun, Y., Trainor-Guitton, W., ... Bacon, D. (2014). Key factors for determining groundwater impacts due to leakage from geologic carbon sequestration reservoirs. *International Journal of Greenhouse Gas Control*, *29*, 153–168.

Carslaw, H. S., & Jaeger, J. C. (1959). *Conduction of Heat in Solids* (2nd ed.). Oxford: Clarendon Press.

Chaix, L., & Dominé, F. (1997). Effect of the thermal history of ice crushed at 77 K on its surface structure as determined by adsorption of CH4 at low surface coverage. *Journal of Physical Chemistry B*, *101*(32), 6105–6108. doi: 10.1021/jp963247k

Chaudhuri, A., Rajaram, H., & Viswanathan, H. (2013). Early-stage hypogene karstification in a mountain hydrologic system: A coupled thermohydrochemical model incorporating buoyant convection. *Water Resources Research*, *49*(9), 5880–5899. doi: 10.1002/wrcr.20427

Clemo, T. M., & Smith, L. (1997). A hierarchical model for solute transport in fractured media. *Water Resources Research*, *33*(8), 1763–1783.

Colwell, F. S., Boyd, S., Delwiche, M. E., Reed, D. W., Phelps, T. J., & Newby, D. T. (2008). Estimates of biogenic methane production rates in deep marine sediments at Hydrate Ridge, Cascadia margin. *Applied and Environmental Microbiology*, *74*(11), 3444–3452. doi: 10.1128/AEM.02114-07

Dempsey, D., Kelkar, S., & Pawar, R. (2014). Passive injection: A strategy for mitigating reservoir pressurization, induced seismicity and brine migration in geologic CO2 storage. *International Journal of Greenhouse Gas Control*, *28*, 96–113.

Etiope, G., Drobniak, A., & Schimmelmann, A. (2013). Natural seepage of shale gas and the origin of " eternal flames" in the Northern Appalachian Basin, USA. *Marine and Petroleum Geology*, *43*, 178–186. doi: 10.1016/j.marpetgeo.2013.02.009

Etiope, G., & Martinelli, G. (2002, feb). Migration of carrier and trace gases in the geosphere: An overview. *Physics of the Earth and Planetary Interiors*, *129*(3-4), 185–204. doi: 10.1016/S0031-9201(01)00292-8

Etiope, G., & Oehler, D. Z. (2019). Methane spikes, background seasonality and non-detections on Mars: A geological perspective. *Planetary and Space Science*, *168*(February), 52–61. doi: 10.1016/j.pss.2019.02.001

Fischer, H. B., List, E. J., Koh, R. C., Imberger, J., & Brooks, N. H. (1979). *Mixing in Inland and Coastal Waters*. San Diego: Academic Press.

Fu, P., Hao, Y., Walsh, S. D., & Carrigan, C. R. (2016). Thermal Drawdown-Induced Flow Channeling in Fractured Geothermal Reservoirs. *Rock Mechanics and Rock Engineering*, *49*(3), 1001–1024. doi: 10.1007/s00603-015-0776-0

Geier, J. E., Lee, K., & Dershowitz, W. S. (1988). Field validation of conceptual models for fracture geometry. *Transactions of American Geophysical Union*, *69*(44), 1177.

GEOS-Chem. (2023). [Software]. doi: 10.5281/zenodo.7696632

Giuranna, M., Viscardy, S., Daerden, F., Neary, L., Etiope, G., Oehler, D., ... Amoroso, M. (2019). Independent confirmation of a methane spike on Mars and a source region east of Gale Crater. *Nature Geoscience*, *12*(5), 326–335. doi: 10.1038/s41561-019-0331-9

Gloesener, E. (2019). *Methane clathrate hydrate stability in the martian subsurface and outgassing scenarios* (PhD thesis). Université Catholique de Louvain.

Gough, R. V., Tolbert, M. A., McKay, C. P., & Toon, O. B. (2010). Methane adsorption on a martian soil analog: An abiogenic explanation for methane variability in the martian atmosphere. *Icarus*, *207*(1), 165–174. Retrieved from http://dx.doi.org/10.1016/j.icarus.2009.11.030 doi: 10.1016/j.icarus.2009.11.030

Haagenson, R., & Rajaram, H. (2021). Seismic Diffusivity and the Influence of Heterogeneity on Injection-Induced Seismicity. *Journal of Geophysical Research: Solid Earth*, *126*(6). doi: 10.1029/2021JB021768

Harp, D. R., Bourret, S. M., Stauffer, P. H., & Kwicklis, E. M. (2020). Discriminating Underground Nuclear Explosions Leading To Late-Time Radionuclide Gas Seeps. *Geophysical Research Letters*, *47*(13), 1–8. doi: 10.1029/2019GL086654

Harp, D. R., Ortiz, J. P., Pandey, S., Karra, S., Anderson, D. N., Bradley, C. R., ... Stauffer, P. H. (2018). Immobile Pore-Water Storage Enhancement and Retardation of Gas Transport in Fractured Rock. *Transport in Porous Media*, 26. doi: 10.1007/s11242-018-1072-8

Holtslag, A. A. M., & Boville, B. A. (1993). Local versus nonlocal boundary-layer diffusion in a global climate model. *Journal of climate*, *6*(10), 1825–1842. doi: https://doi.org/10.1175/1520-0442(1993)006⟨1825:LVNBLD⟩2.0.CO;2

Hunter, J. D. (2007). Matplotlib: A 2D graphics environment [Software]. *Computing in Science & Engineering*, *9*(3), 90–95. doi: 10.5281/zenodo.3898017

Jones, E. G., Lineweaver, C. H., & Clarke, J. D. (2011). An extensive phase space for the potential Martian biosphere. *Astrobiology*, *11*(10), 1017–1033. doi: 10.1089/ast.2011.0660

Jordan, A. B., Stauffer, P. H., Knight, E. E., Rougier, E., & Anderson, D. N. (2015). Radionuclide Gas Transport through Nuclear Explosion-Generated Fracture Networks. *Nature Scientific Reports*, *5*(December), 1–10. doi: 10.1038/srep18383

Jordan, A. B., Stauffer, P. H., Zyvoloski, G. A., Person, M. A., MacCarthy, J. K., & Anderson, D. N. (2014). Uncertainty in Prediction of Radionuclide Gas Migration from Underground Nuclear Explosions. *Vadose Zone Journal*, *13*(10), 1–13. doi: 10.2136/vzj2014.06.0070

Klusman, R. W., Luo, Y., Chen, P., Yung, Y. L., & Tallapragada, S. (2022). Seasonality in Mars atmospheric methane driven by microseepage, barometric pumping, and adsorption. *Icarus*, *383*(May), 115079. Retrieved from https://doi.org/10.1016/j.icarus.2022.115079 doi: 10.1016/j.icarus.2022.115079

Lewis, K. W., Peters, S., Gonter, K., Morrison, S., Schmerr, N., Vasavada, A. R., & Gabriel, T. (2019). A surface gravity traverse on Mars indicates low bedrock density at Gale crater. *Science*, *363*(6426), 535–537. doi: 10.1126/science.aat0738

Lin, J. T., & McElroy, M. B. (2010). Impacts of boundary layer mixing on pollutant vertical profiles in the lower troposphere: Implications to satellite remote sensing. *Atmospheric Environment*, *44*(14), 1726–1739. Retrieved from http://dx.doi.org/10.1016/j.atmosenv.2010.02.009 doi: 10.1016/j.atmosenv.2010.02.009

Lin, J. T., Youn, D., Liang, X. Z., & Wuebbles, D. J. (2008). Global model simulation of summertime U.S. ozone diurnal cycle and its sensitivity to PBL mixing, spatial resolution, and emissions. *Atmospheric Environment*, *42*(36), 8470–8483. Retrieved from http://dx.doi.org/10.1016/j.atmosenv.2008.08.012 doi: 10.1016/j.atmosenv.2008.08.012

Luo, Y., Mischna, M. A., Lin, J. C., Fasoli, B., Cai, X., & Yung, Y. L. (2021). Mars Methane Sources in Northwestern Gale Crater Inferred From Back Trajectory Modeling. *Earth and Space Science*, *8*(11). doi: 10.1029/2021EA001915

Lyons, J. R., Manning, C. E., & Nimmo, F. (2005). Formation of methane on Mars by fluid-rock interaction in the crust. *Geophysical Research Letters*, *32*(13), 1–4. doi: 10.1029/2004GL022161

Mahaffy, P. R., Webster, C. R., Cabane, M., Conrad, P. G., Coll, P., Atreya, S. K., ... Others (2012). The sample analysis at Mars investigation and instrument suite. *Space Science Reviews*, *170*(1-4), 401–478.

Manning, C. E., & Ingebritsen, S. E. (1999). Permeability of the Continental Crust: Implications of Geothermal Data and Metamorphic Systems. *Reviews of Geophysics*, *37*(1), 127–150.

Martínez, G., Valero, F., & Vázquez, L. (2009). Characterization of the Martian surface layer. *Journal of the Atmospheric Sciences*, *66*(1), 187–198. doi: 10.1175/2008JAS2765.1

Martínez, G. M., Newman, C. N., De Vicente-Retortillo, A., Fischer, E., Renno, N. O., Richardson, M. I., … Vasavada, A. R. (2017). The Modern Near-Surface Martian Climate: A Review of In-situ Meteorological Data from Viking to Curiosity. *Space Science Reviews*, *212*(1-2), 295–338. Retrieved from `http://dx.doi.org/10.1007/s11214-017-0360-x` doi: 10.1007/s11214-017-0360-x

Massmann, J., & Farrier, D. F. (1992). Effects of atmospheric pressures on gas transport in the vadose zone. *Water Resources Research*, *28*(3), 777–791. doi: 10.1029/91WR02766

Meslin, P. Y., Gough, R., Lefvre, F., & Forget, F. (2011). Little variability of methane on Mars induced by adsorption in the regolith. *Planetary and Space Science*, *59*(2-3), 247–258. doi: 10.1016/j.pss.2010.09.022

Moores, J. E., Gough, R. V., Martinez, G. M., Meslin, P. Y., Smith, C. L., Atreya, S. K., … Webster, C. R. (2019). Methane seasonal cycle at Gale Crater on Mars consistent with regolith adsorption and diffusion. *Nature Geoscience*, *12*(5), 321–325. doi: 10.1038/s41561-019-0313-y

Moores, J. E., King, P. L., Smith, C. L., Martinez, G. M., Newman, C. E., Guzewich, S. D., … Schuerger, A. C. (2019, aug). The Methane Diurnal Variation and Microseepage Flux at Gale Crater, Mars as Constrained by the ExoMars Trace Gas Orbiter and Curiosity Observations. *Geophysical Research Letters*, *46*(16), 9430–9438. doi: 10.1029/2019GL083800

Myers, T. (2012). Potential contaminant pathways from hydraulically fractured shale to aquifers. *Groundwater*, *50*(6), 872–882.

National Research Council. (1997). *Rock fractures and fluid flow: contemporary understanding and applications.* National Academies Press. doi: 10.1029/97eo00345

Neeper, D. A., & Stauffer, P. H. (2012a). Transport by Oscillatory Flow in Soils with Rate-Limited Mass Transfer: 1. Theory. *Vadose Zone Journal*, *11*(2), 1–14. doi: 10.2136/vzj2011.0093

Neeper, D. A., & Stauffer, P. H. (2012b). Transport by Oscillatory Flow in Soils with Rate-Limited Mass Transfer: 2. Field Experiment. *Vadose Zone Journal*, *11*(2), 1–12. doi: 10.2136/vzj2011.0093

Newman, C. E., Gómez-Elvira, J., Marin, M., Navarro, S., Torres, J., Richardson, M. I., … Bridges, N. T. (2017). Winds measured by the Rover Environmental Monitoring Station (REMS) during the Mars Science Laboratory (MSL) rover's Bagnold Dunes Campaign and comparison with numerical modeling using MarsWRF. *Icarus*, *291*(December 2016), 203–231. Retrieved from `http://dx.doi.org/10.1016/j.icarus.2016.12.016` doi: 10.1016/j.icarus.2016.12.016

Newman, C. E., Kahanpää, H., Richardson, M. I., Martínez, G. M., Vicente-Retortillo, A., & Lemmon, M. T. (2019). MarsWRF Convective Vortex and Dust Devil Predictions for Gale Crater Over 3 Mars Years and Comparison With MSL-REMS Observations. *Journal of Geophysical Research: Planets*, *124*(12), 3442–3468. doi: 10.1029/2019JE006082

Nilson, R. H., Peterson, E. W., Lie, K. H., Burkhard, N. R., & Hearst, J. R. (1991). Atmospheric Pumping: A Mechanism Causing Vertical Transport of Contaminated Gases Through Fractured Permeable Media. *Journal of Geophysical Research: Solid Earth*, *96*(B13), 933–948. doi: 10.2752/147597509112541

Onstott, T. C., McGown, D., Kessler, J., Lollar, B. S., Lehmann, K. K., & Clifford, S. M. (2006). Martian CH4: Sources, Flux, and Detection. *Astrobiology*, *6*(2), 377–395.

Ordóñez-Etxeberria, I., Hueso, R., & Sánchez-Lavega, A. (2020). Strong increase in dust devil activity at Gale crater on the third year of the MSL mission and suppression during the 2018 Global Dust Storm. *Icarus*, *347*(February). doi: 10.1016/j.icarus.2020.113814

Ortiz, J. P., Rajaram, H., Stauffer, P. H., Harp, D. R., Wiens, R. C., & Lewis, K. W. (2022). Barometric pumping through fractured rock: A mechanism for venting deep methane to Mars' atmosphere. *Geophysical Research Letters*, *49*(14), e2022GL098946. doi: 10.1029/2022GL098946

Pan, L., Oldenburg, C. M., Pruess, K., & Wu, Y.-S. (2011). Transient CO2 leakage and injection in wellbore-reservoir systems for geologic carbon sequestration. *Greenhouse Gases: Science and Technology*, *1*(4), 335–350.

Pandey, S., & Rajaram, H. (2016). Modeling the influence of preferential flow on the spatial variability and time-dependence of mineral weathering rates. *Water Resources Research*, *52*(12), 9344–9366. doi: 10.1111/j.1752-1688.1969.tb04897.x

Parro, L. M., Jiménez-Díaz, A., Mansilla, F., & Ruiz, J. (2017). Present-day heat flow model of Mars. *Scientific Reports*, *7*(March 2017), 1–9. doi: 10.1038/srep45629

Pick, M. A. (1981). Kinetics of hydrogen absorption-desorption by niobium. *Physical Review B*, *24*(8), 4287.

Pla-García, J., Rafkin, S. C. R., Karatekin, O., & Gloesener, E. (2019). Comparing MSL Curiosity Rover TLS - SAM Methane Measurements With Mars Regional Atmospheric Modeling System Atmospheric Transport Experiments. *Journal of Geophysical Research : Planets*, *124*(8), 2141–2167. doi: 10.1029/2018JE005824

Press, W. H., Teukolsky, S. A., Vetterling, W. T., & Flannery, B. P. (2007). *Numerical Recipes: The Art of Scientific Computing* (3rd ed.). New York: Cambiridge University Press.

Putzig, N. E., & Mellon, M. T. (2007). Apparent thermal inertia and the surface heterogeneity of Mars. *Icarus*, *191*(1), 68–94. doi: 10.1016/j.icarus.2007.05.013

Rey, A., Belelli-Marchesini, L., Etiope, G., Papale, D., Canfora, E., Valentini, R., & Pegoraro, E. (2014, apr). Partitioning the net ecosystem carbon balance of a semiarid steppe into biological and geological components. *Biogeochemistry*, *118*(1-3), 83–101. doi: 10.1007/s10533-013-9907-4

Richardson, M. I., Toigo, A. D., & Newman, C. E. (2007). PlanetWRF: A general purpose , local to global numerical model for planetary atmospheric and climate dynamics. *Journal of Geophysical Research*, *112*(E9), 1–29. doi: 10.1029/2006JE002825

Rodrigo, R., Garcia-Alvarez, E., & Lopez-Gonzalez, M. (1990). Estimates of eddy diffusion coefficient in the Mars' atmosphere. *Atmosfera*, *3*(1), 31–43.

Stauffer, P. H., Rahn, T. A., Ortiz, J. P., Joseph, S. L., Boukhalfa, H., & Snyder, E. E. (2018). *Summary of a Gas Transport Tracer Test in the Deep Cerros Del Rio Basalts, Mesita del Buey, Los Alamos NM* (Tech. Rep.). Los Alamos National Laboratory.

Stauffer, P. H., Rahn, T. A., Ortiz, J. P., Salazar, L. J., Boukhalfa, H., Behar, H. R., & Snyder, E. E. (2019). Evidence for High Rates of Gas Transport in the Deep Subsurface. *Geophysical Research Letters*, *46*, 3773– 3780. doi: 10.1029/2019GL082394

Stevens, A. H., Patel, M. R., & Lewis, S. R. (2015). Numerical modelling of the transport of trace gases including methane in the subsurface of Mars. *Icarus*, *250*, 587–594.

Sun, Y., & Carrigan, C. R. (2014). Modeling Noble Gas Transport and Detection for The Comprehensive Nuclear-Test-Ban Treaty. *Pure and Applied Geophysics*, *171*, 735–750. doi: 10.1007/s00024-012-0514-4

Takle, E. S., Massman, W. J., Brandle, J. R., Schmidt, R. A., Zhou, X., Litvina, I. V., … Rice, C. W. (2004, aug). Influence of high-frequency ambient pressure pumping on carbon dioxide efflux from soil. *Agricultural and Forest Meteorology*, *124*(3-4), 193–206. doi: 10.1016/j.agrformet.2004.01.014

Tsang, Y. W., & Narasimhan, T. N. (1992). Effects of periodic atmospheric pressure variation on radon entry into buildings. *Journal of Geophysical Research: Solid Earth*, *97*(B6), 9161–9170.

Viswanathan, H. S., Pawar, R. J., Stauffer, P. H., Kaszuba, J. P., Carey, J. W., Olsen, S. C., … Guthrie, G. D. (2008). Development of a Hybrid Process and System Model for the Assessment of Wellbore Leakage at a Geologic CO2 Sequestration Site. *Environmental Science & Technology*, *42*(19), 7280–7286. doi: 10.1021/es800417x

Viúdez-Moreiras, D. (2021). A three-dimensional atmospheric dispersion model for Mars. *Progress in Earth and Planetary Science*, *8*(1). Retrieved from `https://doi.org/10.1186/s40645-021-00445-4` doi: 10.1186/s40645-021-00445-4

Viúdez-Moreiras, D., Arvidson, R. E., Gómez-Elvira, J., Webster, C., Newman, C. E., Mahaffy, P., & Vasavada, A. R. (2020). Advective Fluxes in the Martian Regolith as a Mechanism Driving Methane and Other Trace Gas Emissions to the Atmosphere. *Geophysical Research Letters*, *47*(3), 1–8. doi: 10.1029/2019GL085694

Viúdez-Moreiras, D., Richardson, M. I., & Newman, C. E. (2021). Constraints on Emission Source Locations of Methane Detected by Mars Science Laboratory. *Journal of Geophysical Research: Planets*, *126*(12). doi: 10.1029/2021JE006958

Webster, C. R., Mahaffy, P. R., Atreya, S. K., Flesch, G. J., Mischna, M. A., Meslin, P. Y., … Lemmon, M. T. (2015). Mars methane detection and variability at Gale crater. *Science*, *347*(6220), 415–417. doi: 10.1126/science.1261713

Webster, C. R., Mahaffy, P. R., Atreya, S. K., Moores, J. E., Flesch, G. J., Malespin, C., … Navarro-Gonzalez, R. (2018a). Background levels of methane in Mars' atmosphere show strong seasonal variations. *Science*, *360*(6393), 1093–1096.

Webster, C. R., Mahaffy, P. R., Atreya, S. K., Moores, J. E., Flesch, G. J., Malespin, C., … Vasavada, A. R. (2018b). [Supplementary Material] Background levels of methane in Mars' atmosphere show strong seasonal variations. *Science*, *360*(6393), 1093–1096. doi: 10.1126/science.aaq0131

Webster, C. R., Mahaffy, P. R., Pla-Garcia, J., Rafkin, S. C., Moores, J. E., Atreya, S. K., … Vasavada, A. R. (2021). Day-night differences in Mars methane suggest nighttime containment at Gale crater. *Astronomy and Astrophysics*, *650*(December 2019), 1–14. doi: 10.1051/0004-6361/202040030

Yoshida, N., Nakagawa, H., Aoki, S., Erwin, J., Vandaele, A. C., Daerden, F., … Patel, M. (2022). Variations in Vertical CO/CO2 Profiles in the Martian Mesosphere and Lower Thermosphere Measured by the ExoMars TGO/NOMAD: Implications of Variations in Eddy Diffusion Coefficient. *Geophysical Research Letters*, *49*(10), 1–9. doi: 10.1029/2022GL098485

Yung, Y. L., Chen, P., Nealson, K., Atreya, S. K., Beckett, P., Blank, J. G., … Worden, J. (2018). Methane on Mars and Habitability: Challenges and Responses. *Astrobiology*, *18*(10), 1221–1242. doi: 10.1089/ast.2018.1917

Zimmerman, R. W., & Bodvarsson, G. S. (1996). Hydraulic Conductivity of Rock Fractures. *Transport in Porous Media*, *23*(1), 1–30.

Zyvoloski, G. A. (2007). *FEHM: A control volume finite element code for simulating subsurface multi-phase multi-fluid heat and mass transfer* (Tech. Rep.). Los

Alamos, NM: Los Alamos National Laboratory.
Zyvoloski, G. A., Robinson, B. A., Dash, Z. V., Chu, S., & Miller, T. A. (2017). *FEHM: Finite Element Heat and Mass Transfer Code.* [Software] GitHub. Retrieved from `https://github.com/lanl/FEHM/tree/v3.4.0`
Zyvoloski, G. A., Robinson, B. A., Dash, Z. V., Kelkar, S., Viswanathan, H. S., Pawar, R. J., ... Chu, S. (2021). *Software users manual (UM) for the FEHM application version 3.1-3X.* Los Alamos, NM: Los Alamos National Laboratory Report LA-UR-12-24493.
Zyvoloski, G. A., Robinson, B. A., Dash, Z. V., & Trease, L. L. (1999). *Models and Methods Summary for the FEHM Application* (Tech. Rep.). Los Alamos, NM: Los Alamos National Laboratory.

Sub-diurnal methane variations on Mars driven by barometric pumping and planetary boundary layer evolution

J. P. Ortiz[1,2], H. Rajaram[2], P. H. Stauffer[1], K. W. Lewis[3], R. C. Wiens[4], D. R. Harp[5]

[1]Energy and Natural Resources Security, Los Alamos National Laboratory, Los Alamos, NM, USA
[2]Dept. of Environmental Health and Engineering, The Johns Hopkins University, Baltimore, MD, USA
[3]Dept. of Earth and Planetary Sciences, The Johns Hopkins University, Baltimore, MD, USA
[4]Earth, Atmospheric, and Planetary Sciences, Purdue University, West Lafayette, IN, USA
[5]The Freshwater Trust, Portland, OR 97205, USA

Key Points:

- Barometrically-driven atmospheric methane abundance timing controlled by fracture topology and planetary boundary layer (PBL) dynamics
- There is a lower limit to fracture density that can produce observed methane patterns
- A late morning or early evening SAM-TLS sample could constrain diurnal methane pattern and transport processes

Corresponding author: John P. Ortiz, `jportiz@lanl.gov`

Abstract

In recent years, the Sample Analysis at Mars (SAM) instrument on board the Mars Science Laboratory (MSL) *Curiosity* rover has detected methane variations in the atmosphere at Gale crater. Methane concentrations appear to fluctuate seasonally as well as sub-diurnally, which is difficult to reconcile with an as-yet-unknown transport mechanism delivering the gas from underground to the atmosphere. To potentially explain the fluctuations, we consider barometrically-induced transport of methane from an underground source to the surface, modulated by temperature-dependent adsorption. The subsurface fractured-rock seepage model is coupled to a simplified atmospheric mixing model to provide insights on the pattern of atmospheric methane concentrations in response to transient surface methane emissions, as well as to predict sub-diurnal variation in methane abundance for the northern summer period, which is a candidate time frame for *Curiosity*'s potentially final sampling campaign. The best-performing scenarios indicate a significant, short-lived methane pulse just prior to sunrise, the detection of which by SAM-TLS would be a potential indicator of the contribution of barometric pumping to Mars' atmospheric methane variations.

Plain Language Summary

One of the outstanding goals of current Mars missions is to detect and understand biosignatures (signs of life) such as methane. Methane has been detected multiple times in Mars' atmosphere by the *Curiosity* rover, and its abundance appears to fluctuate seasonally and on a daily time scale. With the source of methane on Mars most likely located underground, it is difficult to reconcile these atmospheric variations with an as-yet-unknown transport mechanism delivering the gas to the atmosphere. In this paper, we simulate methane transport to the atmosphere from underground fractured rock driven by atmospheric pressure fluctuations. We also model adsorption of methane molecules onto the surface of pores in the rock, which is a temperature-dependent process that may contribute to the seasonality of methane abundance. We simulated methane emitted from the subsurface mixing into a simulated atmospheric column, which provides insight into the sub-diurnal methane concentrations in the atmosphere. Our simulations predict short-lived methane pulses prior to sunrise for Mars' upcoming northern summer period, which is a candidate time frame for *Curiosity*'s next (and possibly final) sampling campaign.

1 Introduction

The potential presence of methane on Mars is a topic of significant interest in planetary science because of the potential for organic/microbial sources (e.g., methanogenic microbes). Since the early days of NASA's Mars Science Laboratory (MSL) mission, the Tunable Laser Spectrometer (TLS) instrument onboard *Curiosity* rover has made numerous measurements reporting methane in Mars' atmosphere (Webster et al., 2015, 2018a, 2021). Several papers (Webster et al., 2015, 2018a, 2021) document the apparent seasonality of background atmospheric methane concentrations, reporting methane levels that vary in time between 0.25 to 0.65 ppbv.

In addition to seasonal fluctuations in methane, some evidence suggests that atmospheric methane varies on a sub-diurnal time scale as well. SAM-TLS primarily conducts experiments at night due to mission operational constraints, and in fact all TLS detections of methane thus far have been from nighttime measurements. Two lone non-detections in 2019 were reported from daytime measurements (Webster et al., 2021) during northern summer at Gale crater. These daytime non-detections occurred on either side of a normal background methane value collected at night, implying a diurnal to sub-diurnal variability in atmospheric methane. Confirming and characterizing this apparent diurnal variability of methane has been highlighted by the SAM-TLS team as the next key step to understanding methane abundance and circulation at Gale crater (Webster et al., 2021; Moores, Gough, et al., 2019).

The primary goal of this work is to facilitate the science goals of ongoing and future sample collection missions by determining an optimal intra-sol timing for atmospheric sample collection on Mars. *Curiosity* is currently heading into its last northern summer (southern winter) season with a normal pace of operations. Soon, reduced electrical power in conjunction with SAM pump life will likely place limits on scientific operations. It is therefore important to maximize the scientific return of whatever remaining SAM-TLS measurements there may be, especially with regard to characterizing the apparent diurnal variability in methane. Recent models (Giuranna et al., 2019; Yung et al., 2018; Luo et al., 2021; Viúdez-Moreiras, 2021; Viúdez-Moreiras et al., 2021; Webster et al., 2018a, 2015; Pla-García et al., 2019) suggest a local source of methane within Gale crater, with circulation trapping methane at night and dissipating it during the day. Characterizing the diurnal variability of methane provides insight into the underlying mechanisms driving the methane fluctuations. The logical time of year to make relevant measurements is in the northern Summer period between solar longitude (L_s) 120-140°, coincident with the time of year of the previous measurements indicating diurnal variations. At the time of writing, this period is approaching in the months of September-October 2023, which may be the last opportunity for collecting *in situ* atmospheric methane data at Gale crater for the foreseeable future.

Running SAM-TLS experiments at strategically optimal times will improve the probability of gathering useful atmospheric data to answer key questions about methane at Gale crater. Numerical models of methane emissions and mixing within the atmosphere have the potential to inform this goal of determining ideal times to collect samples. The general consensus in the planetary science community is that if methane is present in Mars' atmosphere, its source is most likely located underground. This presents the question of how methane from deep underground can reach the surface rapidly enough to generate the observed short-term atmospheric variations. Some of the possibilities that have been proposed include: a relatively fast methane-destruction mechanism, modulation mechanisms that change the amount of free methane in the atmosphere and near-surface (e.g., regolith adsorption), and rapid transport mechanisms capable of delivering gases from depth (e.g., barometric pumping). This paper focuses on the latter two of these, and uses simulations driven by high resolution pressure and temperature data resolution and as forcing in order to provide insight on the timing of sub-diurnal methane fluxes driven by barometric pumping.

Barometric pumping is an advective transport mechanism wherein atmospheric pressure fluctuations greatly enhance vertical gas transport in the subsurface (Nilson et al., 1991). Low atmospheric pressure draws gases upwards from the subsurface, with air and tracer movement taking place primarily in the higher-permeability fractures rather than the surrounding, relatively low-permeability rock matrix (Figure 1). High atmospheric pressure pushes gases deeper into the subsurface, with some molecules diffusing into the rock matrix, in which the barometric pressure variations do not propagate efficiently. Over multiple cycles of pressure variations, this fracture-matrix exchange produces a ratcheting mechanism (Figure 1) that can greatly enhance upward gas transport relative to diffusion alone (Neeper & Stauffer, 2012a; Nilson et al., 1991; Massmann & Farrier, 1992; Takle et al., 2004; Harp et al., 2018). Barometric pumping has been studied in a variety of terrestrial contexts, such as: CO_2 leakage from carbon sequestration sites (Carroll et al., 2014; Dempsey et al., 2014; Pan et al., 2011; Viswanathan et al., 2008) and deep geological stores (Rey et al., 2014; Etiope & Martinelli, 2002), methane leakage from hydraulic fracturing operations (Myers, 2012), radon gas entry into buildings (Tsang & Narasimhan, 1992), contaminant monitoring (Stauffer et al., 2018, 2019), and radionuclide gas seepage from underground nuclear explosions and waste storage facilities (Bourret et al., 2019, 2020; Harp et al., 2020; Carrigan et al., 1996, 1997; Jordan et al., 2014, 2015; Sun & Carrigan, 2014). In the context of Mars, barometric pumping in fractures was first hypothesized as a potentially effective transport mechanism for underground methane by Etiope and Oehler (2019). Although two modeling papers (Viúdez-Moreiras et al., 2020; Klusman et al., 2022) have investigated barometric pumping in the context of methane transport on Mars, our recent paper (Ortiz et al., 2022) is, to our knowledge, the first to consider the explicit role of subsurface fractures and the ratcheting mechanism. In that paper, we demonstrated that barometric pumping in fractured rock is capable of producing significant surface fluxes of methane from depths of 200 m, and that the timing and magnitude of those fluxes was reasonably consistent with the timing of high-methane periods measured by *Curiosity*. The emphasis on timing in that paper was on reproducing the observed seasonality of surface fluxes. We highlighted in our discussion that the timing of surface fluxes could be further modulated by processes that retard gas transport and therefore included adsorption in shallow regolith to produce a more complete transport model.

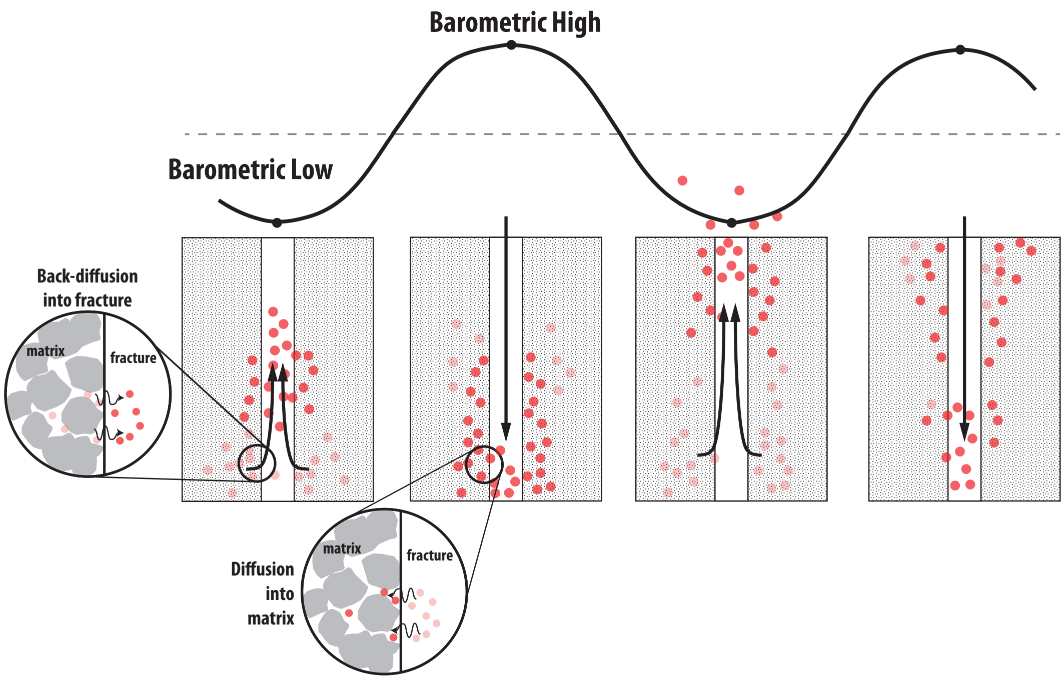

Figure 1. Schematic of the barometric pumping mechanism, which has ratcheting enhanced gas transport due to temporary immobile storage. The upward advance of the gas during barometric lows is not completely reversed during subsequent barometric highs due to temporary storage of gas tracer into rock matrix via diffusion. Adapted from Figure 1 in Harp et al. (2018).

Adsorption is a reversible phenomenon in which gas or liquid molecules (the "adsorbate") adhere to the surface of another material (the "adsorbent"). Particle transport (e.g., methane) through porous media (e.g., martian regolith), is retarded by adsorption onto the pore walls. Adsorption is aided by adsorbents with high specific surface area, which have more sites onto which the particles can adsorb. It is believed that much of the martian regolith consists of fine mineral dust particles (Ballou et al., 1978), which have a large specific surface area (Meslin et al., 2011), making the regolith relatively amenable to adsorption. Furthermore, adsorption reactions are generally temperature-dependent, with lower temperatures favoring adsorption and higher temperatures favoring desorption. Specifically, both the rate of adsorption and the equilibrium surface coverage are higher at lower temperatures for many systems (Adamson, 1979; Pick, 1981).

Several previous papers have investigated whether the temperature dependence of regolith adsorption could explain the seasonal variations in methane in the martian atmosphere because of this temperature dependence. Work by Gough et al. (2010) used laboratory-derived constants to determine the seasonal variation of methane across Mars due to adsorptive transfer to and from the regolith. Extrapolating to martian ground temperatures, the adsorption coefficient measured for methane gas was relatively low, though the authors concluded that the mechanism could still be capable of contributing to rapid methane loss. Meslin et al. (2011) used a global circulation model to determine the seasonal variation of methane due to adsorptive transfer into and out of the regolith, finding that at Gale's latitude, this seasonal variation in methane was less than a few percent, and therefore not likely the cause of the methane fluctuations. Another paper (Moores, Gough, et al., 2019) investigated regolith adsorption, but with methane provided by a shallow (30 m) microseepage source, and found that their one-dimensional adsorptive-diffusive numerical model was able to produce the observed seasonal variation. More recently, research by Klusman et al. (2022) followed the analysis of Moores, Gough, et al. (2019) pertaining to adsorption, while also considering the role of barometric pumping as the primary transport mechanism for the shallow subsurface, and were able to produce the seasonal variation of methane when invoking high regolith permeabilities (10^{-10} m^2).

In this paper, we consider the barometrically-induced transport of a subsurface methane source to the surface that is modulated by temperature-dependent adsorption/desorption. Our two-dimensional simulations consider the explicit role of discrete, interconnected fractures in promoting advective transport, with additional seasonal modulation provided by temperature-dependent regolith adsorption. To elucidate the effects of subsurface architecture (i.e., the degree of fracturing in the rock, quantitatively represented in terms of fracture density, and defined as the ratio of fracture volume to total bulk rock volume), we simulate gas flow and transport through rocks with fracture density ranging from 0% (unfractured), to 0.035% (highly fractured). The subsurface seepage model is coupled to an atmospheric mixing model to provide insights on the pattern of atmospheric concentrations of methane in response to transient surface methane emissions, as well as to predict sub-diurnal variation in methane abundance for the northern summer season.

2 Methods: Fractured-Rock Heat and Mass Transport Simulations with Coupled Atmospheric Mixing

We used fractured-rock heat and mass transport simulations to determine the approximate timing of transient methane surface fluxes driven by barometric fluctuations throughout the Mars year. Calculations are performed within the Finite-Element Heat and Mass (FEHM) simulator, a well-tested multiphase code (Zyvoloski et al., 1999, 2021, 2017). FEHM has been used extensively in terrestrial barometric pumping studies (Stauffer et al., 2019; Bourret et al., 2019, 2020; Jordan et al., 2014, 2015; Neeper & Stauffer, 2012a, 2012b), and was previously modified by the author to adapt to conditions at Mars in a related paper examining barometric pumping of methane (Ortiz et al., 2022). We have made a simplifying assumption that there is no water in the domain, which would reduce available air-filled porosity (as ice) and cause temporary immobile storage due to phase partitioning (as liquid). Gravity and atmospheric gas properties are modified for this study to replicate Mars conditions.

Our simulations require several steps: (1) heat flow simulations to generate the subsurface temperature profiles, (2) subsurface mass flow and transport simulations of Mars air and methane driven by barometric fluctuations, with regolith adsorption terms dictated by the subsurface temperature changes from step 1, and (3) atmospheric mixing of methane emitted from the subsurface into a transient planetary boundary layer (PBL) column in order to calculate CH_4 mixing ratios.

Initial testing of a coupled energy and mass transport model indicated that due to conduction dominance (the fracture volume fraction is very small), the temperature field can be adequately described using a decoupled 1-D conductive heat transfer model. We therefore run the heat transport simulations to generate time-dependent temperature profiles with depth. We then run the 2-D, fractured-rock mass flow and transport simulations to calculate the fluxes of martian air and CH_4 driven by barometric fluctuations. The flow model assumes isothermal conditions, while the transport model considers temperature variations in its calculation of adsorption coefficients. The assumption of isothermal conditions in the flow model is justified based on verification tests, which indicated that the martian air flow properties were not significantly modified by ignoring temperature effects (Supporting Information 2.4). Mass flow and transport equations in the fractures are coupled to transport equations in the rock matrix to simulate the overall behavior of gases in fractured rock. These approaches are standard in subsurface hydrogeology – the governing equations and computational approach are described in detail below in section 2.2. Finally, we simulate the atmospheric mixing of methane by coupling the surface methane emissions to a diffusive transport model within a PBL column of time-varying height (section 2.4). This step allows us to infer atmospheric methane concentrations generated in response to the time history of surface fluxes emitted in the subsurface seepage model.

2.1 Heat Flow Model

Although the mass flow and transport simulations use a 2-D domain, we found that simple matrix conduction dominated over fracture convection, which had a negligible influence over subsurface temperatures (Supporting Information section 2.3), justifying the simulation of transient subsurface heat transport using a 1-D model. The 1-D approach also facilitates computational efficiency due to the high degree of mesh refinement required to accurately simulate subsurface temperatures (Supporting Information section 2.1). The single-phase heat conduction equation (Carslaw & Jaeger, 1959) is as follows:

$$\frac{\partial T}{\partial t} = \alpha \nabla^2 T \tag{1}$$

where T is the temperature [K], t is time [s], and α is the thermal diffusivity coefficient [$m^2\ s^{-1}$] ($\alpha = \frac{\kappa}{c\rho}$, where κ is the thermal conductivity of the material [W m^{-1} K^{-1}], c is the specific heat capacity [J K^{-1} kg^{-1}], and ρ is the density of the material [kg m^{-3}]).

We use the following subsurface heat flow properties in the heat flow model: κ = 2.0 W m^{-1} K^{-1} (Parro et al., 2017; Klusman et al., 2022), intrinsic rock density = 2900 kg m^{-3} (Parro et al., 2017), rock specific heat capacity = 800 J $(kg \cdot K)^{-1}$ (Jones et al., 2011; Gloesener, 2019; Putzig & Mellon, 2007), geothermal gradient = 0.012908 °C m^{-1} (Klusman et al., 2022).

2.1.1 Boundary and Initial Conditions: Heat Flow Model

We prescribe an initial surface temperature of -46.93 °C (226.22 K), which is the mean surface temperature at Gale crater (Klusman et al., 2022). Ground surface temperatures fluctuate about this mean value, so this temperature is also used as the reference temperature for CO_2 properties (Mars atmosphere is 95% CO_2) in the equation of state for the mass flow model. At ground surface, we prescribe temperature as a time-varying Dirichlet boundary condition. We generated a synthetic temperature record representative of the surface temperatures collected by *Curiosity*. We extended the time series of generated temperatures so that the simulations can spin up with a sufficiently long record. At the bottom of the domain, we prescribe temperature as a constant Dirichlet boundary condition assigned based on the geothermal gradient and depth of the domain being considered.

2.2 Subsurface Mass Flow & Methane Transport Model

The flow and transport simulations are set up similarly to those presented in Ortiz et al. (2022), with some exceptions listed in the subsequent paragraph. Transient barometric pressures are prescribed at the ground surface and serve as the primary forcing condition. Methane is produced at a constant rate within a 5-m-thick zone at variable depths within the domain depending on the scenario, and is allowed to escape the subsurface domain only at the ground surface boundary.

In contrast to the simulations previously published (Ortiz et al., 2022), these simulations include the effects of temperature-dependent regolith adsorption. We model regolith adsorption as a Langmuir adsorption process, following Gough et al. (2010) and Moores, Gough, et al. (2019), described in greater detail in the following subsection (section 2.2.1). The martian air, which is $\sim 95\%$ CO_2, and the tracer gas (methane, CH_4) have properties consistent with the mean ambient pressure and temperature conditions at Gale crater.

As in the heat flow model, we extracted the dominant frequency and amplitude components of the barometric pressure record collected by the *Curiosity* Mars Science Laboratory Rover Environmental Monitoring Station (MSL-REMS; `https://pds.nasa.gov/`) using Fourier analysis. We then generated a synthetic barometric pressure record using these components, which allows us to treat the problem in a more general way while extending the time series of the pressure forcing to achieve cyclical steady-state in the surface fluxes.

2.2.1 Governing Equations and Boundary Conditions

Flow The governing flow equations for single-phase flow of martian air in the fracture network are given by:

$$b\frac{\partial \rho}{\partial t} + \nabla \cdot (\rho \vec{Q}_f) = \sum(-\rho \vec{q} \cdot \vec{n})_{\mathrm{I}}, \text{ where} \tag{2}$$

$$\vec{Q}_f = -\frac{b^3}{12\mu}\nabla(P_f + \rho g z) = -\frac{b k_f}{\mu}\nabla(P_f + \rho g z) \tag{3}$$

where ∇ is the 2-D gradient operator (operating in the fracture plane), ρ is the air density [kg m^{-3}], t is time [s], $\vec{Q}_f$ is the in-plane aperture-integrated fracture flux [m^2 s^{-1}], $\vec{q}$ is the volumetric flux [m^3/(m^2 s)] of air in the rock matrix, $\vec{n}$ denotes the normal at the fracture-matrix interfaces pointing out of the fracture (I), b is the fracture aperture [m], μ is the dynamic viscosity of air [Pa s], P_f is air pressure within the fracture [Pa], k_f is fracture permeability [m^2], g is gravitational acceleration [m s^{-2}], and z is elevation [m]. The right-hand side of (2) represents the fluxes across the fracture-matrix interface, where positive $\vec{q}\cdot\vec{n}$ is flux into the fracture. Note that (2) is an aperture-integrated two-dimensional equation for fracture flow and (3) is the local cubic law for laminar fracture flow (Zimmerman & Bodvarsson, 1996).

Governing equations for flow in the matrix are given by:

$$\phi\frac{\partial \rho}{\partial t} + \nabla \cdot (\rho \vec{q}) = 0, \text{ where} \tag{4}$$

$$\vec{q} = -\frac{k_m}{\mu}\nabla(P_m + \rho g z) \tag{5}$$

where ∇ is the 3-D gradient operator, ϕ is the porosity [– ; m^3/m^3], k_m is matrix permeability [m^2], and P_m is the air pressure in the rock matrix [Pa]. Note that $P_f = P_m$ on the fracture-matrix interface (I), and the pressure gradients ∇P_m at the fracture-matrix interface control the right-hand side of (2). We make the assumption that the bulk movement of air through the rock matrix behaves according to Darcy's law (5). In the case of a low-permeability rock matrix, the pressure gradients and fluxes induced in the matrix by barometric pressure variations are typically small.

Transport The governing equations for transport of a tracer gas (e.g., methane) in a fracture are given by:

$$b\frac{\partial(\rho C_f)}{\partial t} + \nabla \cdot (\rho \vec{Q}_f C_f) - \nabla \cdot (b\rho D \nabla C_f) = \sum \left[(-\rho \vec{q} C_m + k_{eq}\phi\rho D \nabla C_m)\cdot \vec{n}\right]_{\mathrm{I}} + \dot{m}_f \quad (6)$$

where C_f and C_m are tracer concentrations [mol kg_{air}^{-1}] in the fracture and matrix, respectively; D is the molecular diffusion coefficient of the tracer [m^2 s^{-1}]; k_{eq} is the Langmuir equilibrium distribution coefficient; $\vec{n}$ is the normal at the fracture-matrix interfaces pointing out of the fracture (I); and $\dot{m}_f$ is the tracer source in the fracture plane [mol m^{-2} s^{-1}]. The first term on the right-hand side of (6) represents the tracer mass fluxes across the fracture-matrix interfaces. Note that the mass fluxes across fracture-matrix interfaces include advective and diffusive fluxes. Even in the absence of significant air flow in the matrix, diffusive flux exchanges between the fracture and matrix persist and are included in our formulation.

Governing equations for transport in the rock matrix with adsorption are given by:

$$\phi\frac{\partial \rho C_m}{\partial t}\left[1 + \frac{(1-\phi)\rho_r s_{max} k_{eq}}{(1+k_{eq}C_m)^2}\right] + \nabla\cdot(\rho\vec{q}C_m) - \nabla\cdot(k_{eq}\phi\rho D\nabla C_m) = \dot{m}_m \quad (7)$$

where ρ_r is the rock density [kg m^{-3}], s_{max} is the maximum adsorptive capacity of the adsorbent [kg_{CH_4}/kg_{rock}], k_{eq} is the Langmuir equilibrium distribution coefficient, and $\dot{m}_m$ is the tracer source in the matrix [mol m^{-3} s^{-1}], and $C_f = C_m$ on the fracture-matrix interface. The distribution coefficient k_{eq} is temperature-dependent, and its formulation in the model is described in more detail in section 2.2.1.

Boundary and Initial Conditions The flow and transport simulations use martian air ($\sim$ 95% CO_2) and methane properties consistent with the mean surface temperature at Gale crater (-46.93°C). The bottom of the domain is a no-flux boundary. The left and right lateral boundaries are no-flux boundaries. The top/surface boundary is forced by the synthetic barometric pressure record we generated using frequency and amplitude components representative of the pressure record collected by MLS-REMS (see Supporting Information section 1). Vapor-phase methane and martian air are allowed to escape the domain from the top boundary. We prescribe a continuous methane production rate (9.6×10^{-7} mg CH_4 m^{-3} sol^{-1}) within a 5-m-thick zone at the bottom spanning the lateral extent of the domain (Figure 2a). This rate is consistent with measurements of methanogenic microbes at depth in Mars-analog terrestrial settings (Onstott et al., 2006; Colwell et al., 2008) in addition to liberal estimates of the maximum methane production rate by serpentinization reactions on Mars (Stevens et al., 2015). Our model assumes direct source rock-to-seepage pathway similar to that described in Etiope et al. (2013), rather than a source-reservoir-seepage system. We considered a range of methane source depths (labeled as "methane production zone" in Figure 2a) from 5 - 500 m below ground surface. For source depths $\leq$ 200 m, a standard 200 m depth model domain was used. For the cases with source depth 500 m, we used a model domain of depth 500 m.

The flow and transport simulations are performed in three steps: (1) initialization, (2) "spin-up", and (3) the main flow and transport runs. We initialize the flow model using a constant surface pressure for 10^8 years to create a martian air-static equilibrium gradient throughout the subsurface. This duration is chosen because it is sufficiently long; after 10^8 years, we can confidently assert that no pressure changes occur to the martian air-static gradient that develops. The initialization simulation is run without methane in the domain. We used this martian air-static pressure equilibrium as the initial state for the flow and transport simulations.

We then run a spin-up simulation lasting 50,100 sols, equivalent to 75 Mars Years (MY). The purpose of the spin-up simulation is to establish the memory of surface pressure and temperature fluctuation periodicity in the subsurface. Additionally, it allows

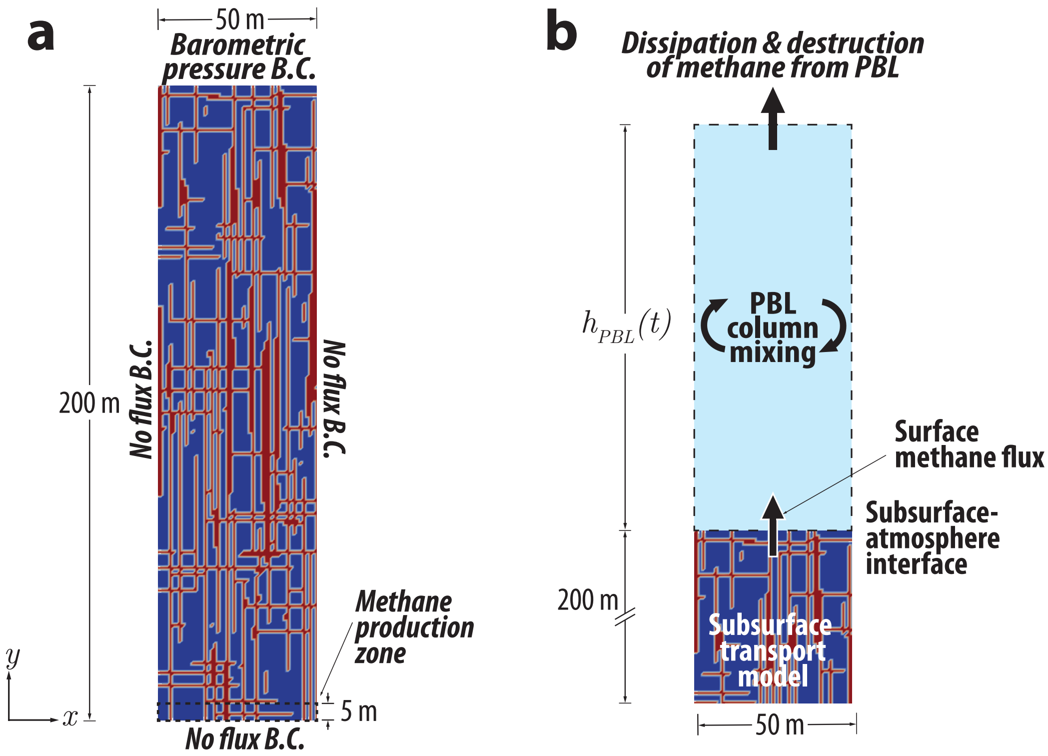

Figure 2. Schematics of model domains used in flow and transport simulations. (a) The subsurface fracture-rock flow and transport model. Fracture network generated using the Lévy-Lee algorithm. Fractures are shown in red, with rock matrix in blue. A methane source located in the methane production zone produces methane at a constant rate. (b) Schematic of the coupled subsurface-atmospheric mixing model. Methane is emitted into the atmosphere from the subsurface fractured-rock transport model. Mixing of methane occurs via 1-D vertical diffusion within the atmospheric column (light blue region), the volume of which varies seasonally and hourly based on the evolution of the planetary boundary layer (PBL) height, $h_{PBL}(t)$. The atmospheric mixing model is described in detail in section 2.4.

for the methane generated in the source zone to sufficiently populate the subsurface and reach a cyclical steady-state in terms of surface flux. We verify in each case that the system in each case has reached a cyclical steady-state equilibrium by identifying a linear trend in cumulative surface mass outflow. The domain is initially populated with a uniform concentration of methane gas ($C_0 = 9.6 \times 10^{-5}$ mol kg$_{air}^{-1}$) to allow the subsurface to more efficiently reach a quasi-equilibrium by pumping out excess methane from the system in the early stages of the simulation. Adsorbed methane concentration is initially zero everywhere. Finally, we run the flow and transport simulations starting from the conditions established in the initialization and spin-up runs. The final simulations are run for 75 MY, and implement the same mechanisms as the spin-up simulations.

2.2.2 Temperature-Dependent Langmuir Adsorption Model Implementation

The Langmuir adsorption isotherm can be used to adequately describe the adsorption/desorption process on Mars analogs (Moores, Gough, et al., 2019). This is partly due to the fact that for methane at the low average temperatures on Mars, the surface coverage θ (i.e., the fraction of of the adsorption sites occupied at equilibrium), is estimated to be quite low (of order 10^{-10}), so that the Brunauer-Emmett-Teller (BET) formulation is unnecessary. The equilibrium rate constant k_{eq} (ratio of sorbed phase to gas phase concentration) for the adsorption isotherm is defined as:

$$k_{eq} = \frac{s_i}{C_i} = \frac{k_a}{P_i k_d} = \frac{k_a}{C_i k_d} = \frac{R_a/(1-\theta)P_i}{R_d/P_i} \tag{8}$$

where k_{eq} is the equilibrium rate constant, s_i is the sorbed-phase concentration of tracer gas i (which in this case can be assumed to be CH_4), C_i is the concentration of the tracer gas i, k_a is the adsorption rate constant, k_d is the desorption rate constant, P_i is the partial pressure of the tracer gas, R_a and R_d are the absolute rates of adsorption and desorption, and θ is the surface coverage. The equilibrium surface coverage θ_{eq} can be approximated using the k_{eq} at a given partial pressure of methane P_{CH_4} (or concentration C_{CH4}) and temperature T:

$$\theta_{eq} = \frac{k_{eq} P_{CH_4}}{1 + k_{eq} P_{CH_4}} = \frac{k_{eq} C_{CH_4}}{1 + k_{eq} C_{CH_4}} \tag{9}$$

The equilibrium constant can be adapted to a partial-pressure basis:

$$k_{eq} = \frac{\gamma}{\eta} \frac{\nu h}{4\mathrm{ML}_{CH_4}} \left(\frac{1}{k_B T}\right)^2 \exp\left(\Delta H/RT\right) \tag{10}$$

where γ is the uptake coefficient (determined experimentally), η is the evaporation coefficient, ν is the mean molecular speed, ML_{CH_4} is the number of methane molecules per m^2 of adsorptive surface required to form a monolayer, h is Planck's constant, and k_B is Boltzmann's constant. The monolayer coverage variable ML_{CH_4} is calculated as 5.21×10^{18} molecules m^{-2} based on the size of an adsorbed methane molecule (19.18 Å) (Chaix & Dominé, 1997).

Implementation of temperature-dependent adsorption in FEHM is relatively straightforward. Because the simulation time is quite long, it is more computationally efficient to sequentially couple the temperature field to the mass flow and transport simulations. We performed several verification tests to ensure that the martian air flow properties were not significantly modified by ignoring temperature effects (Supporting Information 2.4). Using the subsurface temperatures acquired from the heat flow simulation, at each node we assign a distribution coefficient for the adsorption reaction that varies with depth and time. In this way, the flow and transport simulations are non-isothermal insofar as they account for temperature-dependent adsorption.

Gough et al. (2010) reported on the results of laboratory studies of methane adsorption onto JSC-Mars-1, a martian soil simulant, and determined the ΔH methane adsorption using experimentally determined values of the uptake coefficient (γ), which is the ratio between the adsorption rate and gas molecule collision rate. They found that the observed energy change, ΔH_{obs}, for methane adsorption onto JSC-Mars-1 is 18 ± 1.7 kJ mol^{-1}. Although not identical to the overall adsorption enthalpy, ΔH_{tot}, it is a lower limit for this process that is similar to the overall adsorption enthalpies reported by others for similar systems (Gough et al., 2010). From this, we have calculated the values of k_{eq} as it varies with temperature and tabulated them into a format usable by FEHM.

Because the surface temperature perturbations do not propagate very far into the subsurface (Figure S7), we actively calculate the time-dependent Langmuir distribution coefficient k_{eq} only for the upper 5 meters of regolith, and we assign a temporally- and spatially- constant average k_{eq} value for the remainder of the subsurface. This has the added benefit of reducing the computational costs of the simulation.

2.3 Geologic Framework and Numerical Mesh

We assigned the background rock matrix a porosity (ϕ_m) of 35%, which is in the range estimated by Lewis et al. (2019) based on consideration of the low bedrock density at Gale crater. We set the background rock permeability (k_m) to $1{\times}10^{-14}$ m^2 (0.01 Darcies). This is slightly more permeable than the conservative $3{\times}10^{-15}$ m^2 prescribed by previous research modeling hydrothermal circulation on Mars (Lyons et al., 2005), which is reasonable, as permeability tends to decrease with depth (Manning & Ingebritsen, 1999) and our domain (200-500 m) is much shallower than the domain considered there ($\sim$ 10 km). We assumed a fracture porosity (ϕ_f) of 100% (i.e., open fractures); we calculated fracture permeability (k_f) as $k_f = b^2/12 = 8.3 \times 10^{-8}$ m^2 assuming a fracture aperture (b) of 1 mm for all fractures in the domain. Rover photographs of bedrock fractures often show fracture apertures in the range of 1-2 cm (Figures S12, S13). However, these photographs are nearly always of fractures expressed at the planet's surface, where they are potentially exposed to freeze-thaw cycles and dehydration of the surrounding rocks, which will cause the fracture apertures to expand. These processes are not as active below the surface, so fracture apertures at depth will be comparatively narrower. Furthermore, at least in the shallow subsurface, fractures tend to be somewhat infilled by dust and/or unconsolidated material (Figure S12) such that the effective permeability of the fracture is less than that predicted by the cubic law ($k_f = \frac{b^2}{12}$, where k_f is fracture permeability [m^2]). These factors combined with the fact that lithostatic pressure, a force that tends to close fractures, increases with depth, lead us to prescribe uniform 1 mm fracture apertures as an approximate value for Mars' subsurface.

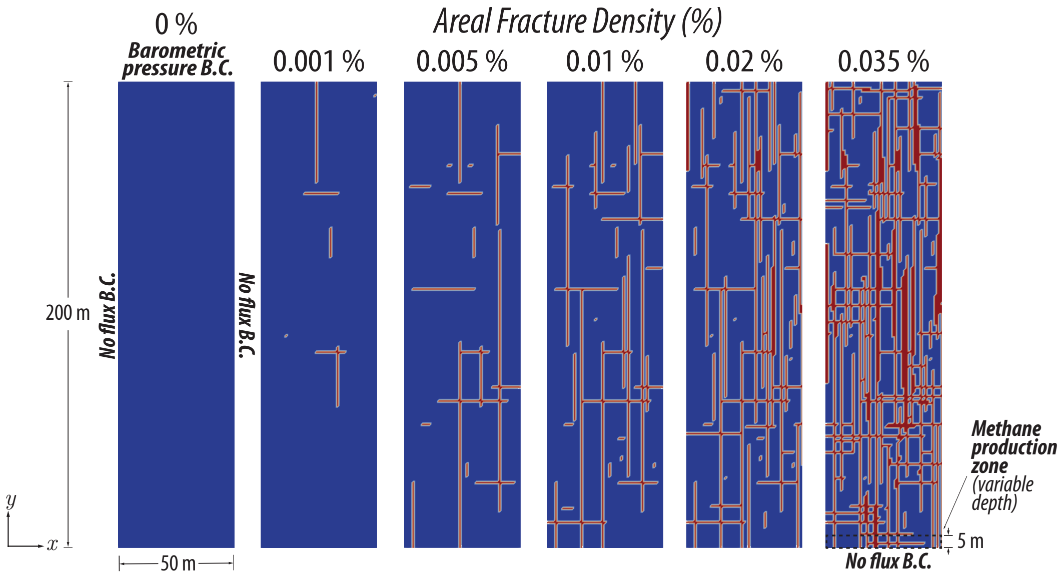

Figure 3. Schematic of the subsurface model domain showing subsurface architectures (i.e., fracture densities) used in this study.

2.3.1 *Numerical Mesh and Fracture Generation Algorithm*

We generated the fracture networks in our scenarios to be somewhat representative of Mars' subsurface. Because the subsurface on Mars is so poorly characterized, we estimate the fracture density (i.e., the ratio of fracture volume to bulk rock volume) based on rover photographs depicting surface expression of fracture networks at Gale crater (Figure S13) and extrapolated their distribution into the subsurface. To address the likelihood of variable subsurface architecture, we consider the following range of fracture densities: 0% (unfractured), 0.001%, 0.05%, 0.01%, 0.02%, and 0.035%, shown in Figure 3.

The model is set up in FEHM as a two-dimensional planar domain 50 m wide and with variable domain depth. For scenarios with methane source depth $\leq$200 m, we use a mesh with domain depth 200 m. For the scenario with source depth 500 m, we use a mesh of depth 500 m. The computational mesh was generated using the LANL developed software GRIDDER (`https://github.com/lanl/gridder`, 2018). Mesh discretization is uniform in the x and y directions such that $\Delta x = \Delta y = 1$ m. We randomly generated orthogonal discrete fractures using the 2-D Lévy-Lee algorithm (Clemo & Smith, 1997), a fractal-based fracture model (Geier et al., 1988) produced by random walk. An orthogonal fracture network is a general case, though it can be a reasonable assumption since in mildly deformed (i.e., less tectonically active) bedded rocks, fractures are commonly oriented nearly vertically, with either two orthogonal azimuths or a single preferred azimuth (National Research Council, 1997). The Lévy-Lee model generates a fracture network with a continuum of scales for both fracture length and spacing between fractures. A more detailed description of the algorithm can be found in Supporting Information section 6.1.

This mesh was then mapped onto a 3-D grid and extended across the width of the domain in the y direction – a single cell across – since FEHM does not solve true 2-D problems. This mapping essentially embeds the fractures in the rock matrix via upscaling of properties (see Section 2.3.2), allowing transfer of fluids and tracers to occur at the fracture-matrix interface. This mesh was then mapped onto a uniform grid.

2.3.2 Upscaling of Fracture Properties

Fractures in our model domain are embedded in the rock matrix via upscaling of permeability and porosity. Fracture permeability k_f is upscaled using:

$$k_f = \frac{b^3}{12\Delta x} \tag{11}$$

where b is the assumed fracture aperture (m) and Δx is the grid/cell block size (m). Upscaled to the grid dimensions of the numerical mesh, the modeled (effective) fracture permeability was 8.3×10^{-11} m^2. We upscale fracture porosity using a flow-weighted scheme (Birdsell et al., 2015):

$$\phi_f = \frac{b}{\Delta x} \tag{12}$$

giving a model (effective) fracture porosity of 0.001 (0.1%) at the scale of the computational grid ($\Delta x = \Delta y = \Delta z = 1$ m). The upscaled relationships (11) and (12) consistently allow the simulation of the governing equations (2 - 7) for fractures and matrix using a porous media simulator such as FEHM. This approach is widely used for simulation of flow and transport in fractured rock (Chaudhuri et al., 2013; Fu et al., 2016; Pandey & Rajaram, 2016; Haagenson & Rajaram, 2021).

2.4 Atmospheric Column Mixing Model

Methane vented from the subsurface of Mars mixes within the lower atmosphere, where it can be collected as an atmospheric sample by the SAM-TLS instrument. We simulate atmospheric mixing of methane using a one-dimensional, vertical column diffusive transport finite-difference model in order to make general observations about how the instantaneous surface flux translates to atmospheric abundance of methane (Figure 2b). The atmospheric mixing model is sequentially coupled to the subsurface model as a post-processing step. We then use an optimization routine to determine the range of atmospheric transport parameters that minimize the error of calculated CH_4 abundance compared to the SAM-TLS background measurements. This routine is performed for each fracture density case.

We represent the atmospheric mixing using a 1-dimensional vertical (z-axis) diffusive transport model (13). Surface flux from the subsurface transport model is specified as a time varying flux boundary condition in the atmospheric transport model at the ground surface ($z = 0$ m). The methane diffuses within the atmospheric column, the height of which is equal to the height of the planetary layer (PBL), which varies in thickness hourly and seasonally in 30° increments of solar longitude L_s (Newman et al., 2017).

At night, the PBL height is largely suppressed (< 300 m), approximately constant in height, and experiences relatively quiescent conditions. As the ground surface and atmosphere heats up during the day, the PBL rapidly expands to heights of several kilometers and undergoes a much greater amount of vertical mixing. In our atmospheric mixing model, we therefore conceptualize the PBL at Gale crater as belonging in either one of two states: "collapsed" or "expanded", each having its own set of atmospheric mixing parameters (Figure S10a). In this way, our approach is conceptually similar to the non-local mixing scheme formulated in Holtslag and Boville (1993), which is implemented in the GEOS-Chem model (*GEOS-Chem*, 2023; Lin & McElroy, 2010). The governing equations are as follows:

$$\frac{\partial C}{\partial t} = D_{c,e}\frac{\partial^2 C}{\partial z^2} - k_{c,e}C \tag{13}$$

where C is the atmospheric methane concentration [kg m^{-3}], t is time [s], $D_{c,e}$ is the turbulent/eddy diffusion coefficient [m^2 s^{-1}] with the subscript representing a PBL state of either c (collapsed) or e (expanded), z is the vertical coordinate [m], $k_{c,e}$ is a first-order loss term [s^{-1}]. The PBL state is defined as collapsed when $h_{PBL} < h_{thresh}$, and expanded when $h_{PBL} \geq h_{thresh}$, where h_{PBL} is the height of the PBL, and h_{thresh} is the threshold PBL height [m] marking the transition between collapsed and expanded states (chosen to be 300 m). The loss rate parameter $k_{c,e}$ in this case implicitly combines the effects of photochemical loss (assuming a lifetime of methane in Mars' atmosphere of $\sim$ 300 years; Atreya et al. (2007)) and horizontal advection away from the atmospheric column. This loss rate parameter is conceptually identical to the reciprocal of the effective atmospheric dissipation timescale (EADT) term used in the atmospheric mixing model described by Moores, Gough, et al. (2019).

The diffusive transport equation is solved numerically in Python using a backward Euler finite-difference method (FDM) scheme, which is implicit in time. The domain is discretized spatially such that $\Delta z = 1$ m, and discretized temporally such that each time step $\Delta t = 0.04$ sols. For comparison with SAM-TLS methane abundance measurements, modeled abundances are calculated everywhere and recorded at a height of $z =$ 1 m above ground surface to represent the concentration at the height of the SAM-TLS inlet (Mahaffy et al., 2012).

Computation of the transient concentration profiles is complicated slightly by the fact that the model dimensions vary in time via PBL expansion/contraction. At each time step, we modify the number of nodes based on $h_{PBL}(t)$. The methane concentration profile $C(z)$ at the previous time step is translated to the current time step as an initial condition by compressing/extending the profile in proportion to the change in column height such that mass is conserved. For example, when the model domain expands, the vertical concentration profile likewise expands, causing the maximum concentration to be reduced since the profile is spread over a larger area with mass conserved (Figure S10b). This expansion and contraction of $C(z)$ during PBL state transitions can be conceptualized as vertical advection of the tracer within the atmospheric column induced by PBL extension and collapse.

Independent of the state of the PBL (collapsed/expanded), the specified flux boundary conditions are as follow:

$$-D_{c,e}\frac{\partial C}{\partial z} = j(t) \quad \text{on } z = 0 \text{ m}, \tag{14}$$

$$-D_{c,e}\frac{\partial C}{\partial z} = 0 \quad \text{on } z = h_{PBL}(t) \tag{15}$$

where $j(t)$ is the time-varying surface mass flux emitted [kg m^{-2} s^{-1}] from the subsurface transport model, and the subscripts represent either indicate collapsed (c) or expanded (e) PBL states.

Atmospheric mixing simulations were run with a spin-up period of 3 MY in order to reach a cyclical steady-state with regard to atmospheric CH_4 abundance. Atmospheric mixing was then simulated for 1 MY, with concentrations recorded at the height of the SAM-TLS inlet ($z = 1$ m) in order to compare to background methane abundances observed by *Curiosity* (Webster et al., 2021). Simulations were set up within a differential evolution optimization routine to determine the range of atmospheric transport parameter combinations that best match the observed abundances. Error was quantified in terms of the reduced chi-squared statistic, χ^2_ν (Press et al., 2007). The parameters optimized were the diffusion coefficients for the collapsed and expanded states (D_c and D_e, respectively), as well as the methane loss terms for the collapsed and expanded states (k_c and k_e, respectively). Intuitively, we expect that $D_e \geq D_c$ since the expanded state of the PBL is characterized by increased heating and turbulent eddies, which which will tend to mix atmospheric tracers more rapidly than would conditions in the more stable collapsed state (Lin et al., 2008). Similarly, we also would expect $k_e \geq k_c$, which accounts for the fact that horizontal advection out of the atmospheric column should be greater in the expanded state than in the collapsed state. We therefore constrained the optimization routine such that:

$$\begin{aligned} 10^{-4} \leq &\quad D_c &\leq 10^{1.2} \\ 1.0 \leq &\quad D_e/D_c &\leq 1000 \\ k_{photochemical} \leq &\quad k_c &\leq 0.1 \\ 1.0 \leq &\quad k_e/k_c &\leq 10^6 \end{aligned}$$

where $k_{photochemical}$ is the assumed photochemical loss rate of 1/300 years ($\sim 10^{-10}$ s^{-1}). The collapsed-state diffusion coefficient D_c has a lower bound on the order of magnitude of free-air methane diffusion in Mars' atmosphere. This lower bound is, in fact, rather conservative, as the binary diffusivity of CH_4-CO_2 at overnight pressures (800 Pa) and temperatures (180K) at Gale crater (G. M. Martínez et al., 2017) is approximately 9.4×10^{-4} m^2 s^{-1} (Moores, King, et al., 2019). The upper bound is chosen conservatively as double the diffusion coefficient required for methane to fully mix across the depth of the PBL ($h_{PBL} \approx 250$ m when in a collapsed state) in 1 hour, which we presume to be the shortest reasonable length of time this condition could be reached. Diffusivity in the expanded state (D_e) is assumed to always be greater than or equal to D_c, with an implied maximum value of 10^4 m^2 s^{-1}. This is a conservative upper bounds considering the estimated eddy diffusivity at higher altitudes in Mars' atmosphere (30-100 km), which are of order 2×10^3 m^2 s^{-1} (Rodrigo et al., 1990) and likely greater than the average diffusivity in the lower atmosphere.

2.4.1 Non-Uniqueness of the Solution

The lack of high-frequency methane abundance data means that this problem is rather poorly constrained. In the analysis described above, we arrive at an optimal solution that minimizes error of the simulated abundances compared to the sparsely collected observations by modifying four atmospheric transport variables: D_c, D_e, k_c, and k_e. The magnitude of the eddy diffusion coefficient ($D_{c,e}$) controls how rapidly methane released from the ground surface will mix upwards across the atmospheric column, thereby diluting itself. One can intuit that for the fluxes produced in each subsurface fracture density case, there might be a range of combinations of parameter values that would produce similar annual/seasonal atmospheric abundance patterns, but that would look quite different at the diurnal time scale. We attempt to address this non-uniqueness below in order to provide a more holistic view of the potential diurnal methane abundance patterns dependent on atmospheric mixing rates.

For the fractured subsurface cases that produce the best overall fit to the observed methane abundances in the differential evolution algorithm, we analyze the surrounding parameter spaces that produce similar results with regard to overall reduced χ^2_ν value. The reduced χ^2_ν statistic is used extensively in goodness of fit testing, and has been applied previously by Moores, Gough, et al. (2019) and Webster et al. (2018b) for comparing modeled methane abundance to SAM-TLS measurements (see Press et al. (2007) for a full definition of χ^2_ν). The reduced χ^2_ν takes in the observed SAM-TLS abundance values, modeled abundance values, and the standard error of mean (SEM) uncertainties of the SAM-TLS data (Table 2 in Webster et al., 2021). A value of χ^2_ν around 1 indicates that the match between modeled values and observations is in accord with the measurement error variance (here, the SEM of SAM-TLS data). A $\chi^2_\nu \gg 1$ indicates a poor model fit, and $\chi^2_\nu > 1$ indicates that the fit does not fully capture the data variance (Bevington, 1969).

The "best" fit in each fracture density case is characterized by $\chi^2_\nu = \min \chi^2_\nu$. For a given fracture density case, we subset the simulation outcomes to the parameter combinations with error in the range: $\chi^2_\nu \leq (\min \chi^2_\nu)+0.5$. The 0.5 was arbitrarily chosen to provide a reasonable sample size of candidate solutions, and corresponds to an approximately 8% change in goodness-of-fit probability as calculated by the χ^2_ν statistic. Candidate solutions in this range therefore have similar levels of fit to the "best" scenario, and generally sample a wide range of parameter values and combinations. We then divide this parameter space into 4 scenarios: (a) lowest D_c, (b) highest D_c, (c) smallest k_e/k_c ratio, and (d) largest k_e/k_c ratio. The actual parameters used in these scenarios are detailed in Table 1. The end-member scenarios for diffusivity are conceptually similar to the transport end-members investigated by Moores, King, et al. (2019), in which they considered both a completely static, stably stratified near-surface air layer, in addition to a well-mixed near-surface air layer.

3 Results and Discussion

We present numerical simulations of transient methane flux caused by barometric pressure-pumping into Mars' atmosphere from a constant underground source. We simulated this transport mechanism acting in a range of subsurface architectures by varying the fracture density in our domain (Figure 3). We then translate methane flux (i.e., surface emissions) into atmospheric abundance (i.e., mixing ratio, in ppbv) by supplying the computed methane fluxes to the atmospheric diffusion model described in Section 2.4.

We assess our simulations by comparing their fit to MSL's observed background methane abundance fluctuations (Webster et al., 2021), which included two non-detections at mid-sol measurements in northern summer. We identify the best-fitting simulations by computing the reduced chi squared (χ^2_ν) statistic for the modeled methane abundance variation over one Mars year (L_s 0-360°). Note that the SAM-TLS measurements were taken over multiple Mars years (MY). The parameter optimization approach proceeds based on the overall χ^2_ν value (Table 1), which is calculated using all background SAM-TLS measurements. The optimization approach therefore inherently selects scenarios that best match both the seasonal and sub-diurnal variations. However, due to the paucity of measurements taken at different times of day (i.e., those that would be indicative of

Table 1. Description of parameters used in various atmospheric mixing scenarios for the three best-performing fracture densities. D_c and D_e are in units of [m^2 s^{-1}], and k_c and k_e are in units of [s^{-1}]. Scenarios are described as follows according to the parameter space discussed in section 2.4.1: (best) parameters with overall best fit to SAM-TLS data, (a) lowest D_c, (b) highest D_c, (c) smallest k_e/k_c ratio, and (d) largest k_e/k_c ratio.

Fracture Density [%]	**Scenario**	D_c	D_e	D_e/D_c	k_c ($\times 10^{-7}$)	k_e ($\times 10^{-7}$)	k_e/k_c	**Overall** χ^2_ν	**Summer** χ^2_ν	**Fig.**
0.010	Best	6.9	3186.3	460	3.68	3.72	1.01	2.18	1.19	4e, 5e
	a	0.1	33.3	380	2.63	5.56	2.11	2.61	1.44	4a, 5a
	b	10.0	5559	553	3.58	3.99	1.12	2.20	1.31	4b, 5b
	c	5.8	1081	185	4.29	4.33	1.01	2.66	4.21	4c, 5c
	d	0.5	42.6	91	2.00	6.42	3.21	2.59	1.25	4d, 5d
0.020	Best	0.4	307.2	860	4.03	4.07	1.01	3.33	12.18	S17e, S17e
	a	0.1	53.6	867	4.31	4.55	1.06	3.45	12.57	S17a, S19a
	b	1.2	981.8	852	3.61	3.67	1.01	3.61	19.29	S17b, S19b
	c	0.5	463.5	859	3.95	3.96	1.00	3.34	13.21	S17c, S19c
	d	0.2	179.4	868	3.54	5.39	1.53	3.62	10.79	S17d, S19d
0.035	Best	1.1	688.6	646	3.76	4.01	1.07	3.13	10.44	S18e, S20e
	a	0.1	60.2	590	3.58	4.18	1.17	3.33	12.67	S18a, S20a
	b	1.4	805.3	591	3.89	4.12	1.06	3.15	8.49	S18b, S20b
	c	0.2	105.7	626	3.97	4.06	1.02	3.20	8.94	S18c, S20c
	d	0.3	262.3	960	2.85	4.73	1.66	3.63	17.62	S18d, S20d

sub-diurnal methane variations), the optimization approach is more likely to select parameter combinations that more closely match the seasonal variations observed rather than the sub-diurnal variations. To address this, we pick out the fracture density cases that match the seasonality well (Overall χ^2_ν in Table 1), and examine the surrounding parameter space to observe changes in sub-diurnal methane variations that were measured in northern summer (Summer χ^2_ν in Table 1). We do not explicitly optimize the parameter space to reduce error of sub-diurnal variations in the northern summer period.

Though we investigated a range of methane source depths, because our simulations reach a cyclical steady-state, there was negligible variance in the timing of surface fluxes caused by varying source depth since the subsurface becomes equivalently populated with methane gas. Therefore, the primary source of variance in the timing of surface flux pulses was the fracture density. The best-fitting cases had a fracture density of 0.01% (Figures 4, 5), followed closely by cases with fracture density 0.035% (Figures S18, S20 and 0.02% (Figures S17, S17). The main focus of this paper is on characterizing the timing of methane variations, so the source depth does not matter for the rest of the analysis presented here. The effect of source depth would be more pronounced in the case of a source term that produces methane episodically instead of continuously, such that subsurface concentrations were not at cyclical steady-state.

For each fracture density case, the optimization algorithm arrives at a "best" solution using some combination of atmospheric transport parameters. However, due to the non-uniqueness of potential solutions generated by combinations of atmospheric transport parameters, the "best" result is often nearly indistinguishable from solutions generated by other parameter combinations in terms of error (χ^2_ν). Therefore, we investigate several atmospheric transport end-members in the candidate parameter space for each of the fracture density cases, the three best of which (fracture density 0.01, 0.02, and 0.035%) are presented in Table 1. These scenarios are described in Section 2.4.1, with parameter values detailed in Table 1. It is worth noting that the subsurface cases we investigate with low fracture density (0, 0.001, and 0.005%) produce methane abundance patterns that are almost completely out of phase with the observed abundance pattern, regardless of the choice of atmospheric transport parameters. These results are included in the Supporting Information.

As a general discussion related to evaluating the appropriateness of the modeled diffusivities, atmospheric mixing time is one metric by which we can estimate whether a given set of parameters is realistic. The approximate time required for a system to reach a fully-mixed state in response to an instantaneous point source located on a boundary (Fischer et al., 1979) is described by:

$$t_{ss} = 0.536\frac{L^2}{D} \tag{16}$$

where t_{ss} is the time [s] of full mixing (i.e., when maximum deviation from the steady-state concentration profile is $< 1\%$), L is the length of the domain [m], and D is the diffusion coefficient [m^2 s^{-1}]. Three-dimensional atmospheric modeling performed by Pla-García et al. (2019) determined that the mixing time scale for martian air within Gale crater is approximately 1 sol. Applied to the present model, this implies a collapsed-state diffusion coefficient $D_c \approx 0.4$ m^2 s^{-1} (where $L \approx 250$ m), a minimum expanded-state value of $D_e = 25.2$ m^2 s^{-1} occurring at $L_s = 130°$ (where $\max L = 2045$ m), and a maximum expanded-state value of $D_e = 219$ m^2 s^{-1} (where $\max L = 6017$ m). The implied value of D_c calculated above additionally is of the same order of magnitude as the eddy diffusion coefficient at $z = 1.3$ m estimated by G. Martínez et al. (2009). We therefore give preference in the discussion to parameter-space solutions in our mixing model that have diffusivities of similar orders of magnitude ($0.1 \leq D_c \leq 1.0$ m^2 s^{-1} and $25 \leq D_e \leq 500$ m^2 s^{-1}).

3.1 Seasonal Methane Variation

The best overall fit to SAM-TLS measurements arose in the case where fracture density was 0.01%. Several features are apparent in the abundance plots (Figure 4a-e) showing seasonal atmospheric abundance changes on Mars. Note that the gray band apparent in the plot is the result of large diurnal variations in the simulated abundance. The black line represents the night-time average abundance (calculated between 0:00 and 2:00 LMST) for the sake of visualization, since a significant majority of measurements were performed in this window. It should be noted that the error is calculated based on the simulated instantaneous methane abundance values rather than this night-time average.

Generally, the "best" fit scenario (Figure 4e) represents the seasonal methane variations well throughout the Mars year, especially the elevated abundances in northern summer (L_s 90-180°) and gradual decline in northern autumn (L_s 180-270°). However, exceptions occur in several time periods. The first occasion is from L_s 32-70°, marking the approximate middle of northern spring. Over this interval, the simulated values generally overestimate atmospheric abundance. Secondly, the simulation underpredicts abundance at $L_s \sim 216°$, in northern autumn. The difference between simulated and observed abundances at this point is less pronounced, as the simulated diurnal abundance (shown in gray) falls very nearly within one standard error of the mean (SEM) for this measurement, as indicated by the error bars on the plot. Thirdly, the simulations also underpredict atmospheric abundance at $L_s = 331°$, the middle of northern winter.

The results composite in Figure 4a-d shows the effect of the atmospheric transport end-members investigated for fracture density 0.01%. The general character of the seasonal methane abundance variation remains in each scenario, though the details vary somewhat. Scenarios with smaller D_c (such as scenarios a,d) have a greater range of diurnal abundance (grey band). Smaller D_c in general means that the mixing of methane across the depth of the atmospheric column takes longer. This allows methane concentrations near the emission surface (e.g., at $z = 1$ m, where the SAM-TLS inlet is located) to build to higher values before subsequent mixing. Scenarios with smaller D_c also seem to produce a more pronounced increase in atmospheric methane abundance during northern winter. Scenarios with higher diffusivity (e.g., scenario b) begin to approach an instantaneous mixing condition. Instantaneous mixing may be a reasonable approximation under conditions where the PBL is extremely unstable (such as during a hot, stormy day), but under most conditions it will tend to overestimate vertical mixing (Lin & McElroy, 2010). We initially used a more simplified instantaneous mixing approach similar to what done in Moores, Gough, et al. (2019), but opted for a diffusive mixing model as being more realistic of general atmospheric conditions (discussed in more detail in Supporting Information 4).

3.2 Sub-diurnal Methane Variation

With the goal of determining useful timing of SAM-TLS measurements, we also examined our simulations over shorter time scales, looking at the diurnal variations in methane abundance in northern summer (Figure 5e). Northern summer is the only season in which SAM-TLS has performed daytime enrichment method measurements, generally collected around noon (Webster et al., 2021). All other measurements have been collected close to midnight, so this is therefore the only season in which we have clues as to the possible sub-diurnal shape of methane variations. Direct observation of a sub-diurnal shape has not been possible due to instrument operational constraints of SAM-TLS, which cannot make multiple measurements on the same sol. The defining characteristic of these results (Figure 5e) is the sharp drop-off in atmospheric abundance that occurs between approximately 8:00 and 16:00 local time (LMST), which coincides with the elevated planetary boundary layer height seen in the bottom panel of the same figure. Note that we use a 24-hour time convention for the remainder of the discussion, where 0:00 - 11:59 LMST represent the morning from midnight to just before noon. In our model, the drop-off in abundance is controlled largely by the mid-day extension of PBL height, and also the generally 2-3 order of magnitude difference between D_e and D_c (Table 1). When the PBL collapses in the early evening (∼17:00 LMST), it remains relatively shallow (i.e., atmospherically quiescent) through the night until early the next morning. The atmospheric mixing ratio responds accordingly by rebounding somewhat after the PBL collapse, after which point it holds relatively steady into the following morning.

The "best" scenario shown in Figure 5e generally reproduces the observed summer methane abundances. The model slightly underpredicts methane abundance relative to that observed at $L_s = 158.6°$ (yellow circle), though the modeled concentration is within one SEM of the measured value. The mid-day non-detections (L_s 120.7 and 134°) are generally captured by the model, as well as the positive SAM-TLS detection that was collected between them (L_s 126.3° at 23:56 LMST). The latter point distinguishes this case from the higher-fracture-density cases (0.035% and 0.02%), which where not able to match this intermediate observation regardless of the scenario considered (Figures S20, S19). An accurate match to the observed abundances is thus controlled by both the assumed subsurface architecture and the parameters in the atmospheric transport model.

For the case shown in Figure 5f, elevated daytime fluxes have a somewhat bimodal pattern (i.e., two primary methane flux pulses). The first occurs between 4:00 and 6:00 LMST, and has substantially greater magnitude (by a factor of 5 - 11) for the dates with non-detections (L_s = 120.7, 134°) and at L_s 158.6° than it does on the dates of the other measurements. The second primary methane pulse occurs between 15:30 and 17:00 for L_s = 103.4, 126.3, and 142.4°, and less strongly (by a factor of 1.4 - 5) between 16:00 and 18:00 for the L_s = 120.7, 134° (non-detects) and $L_s = 158.6°$. The timing of the

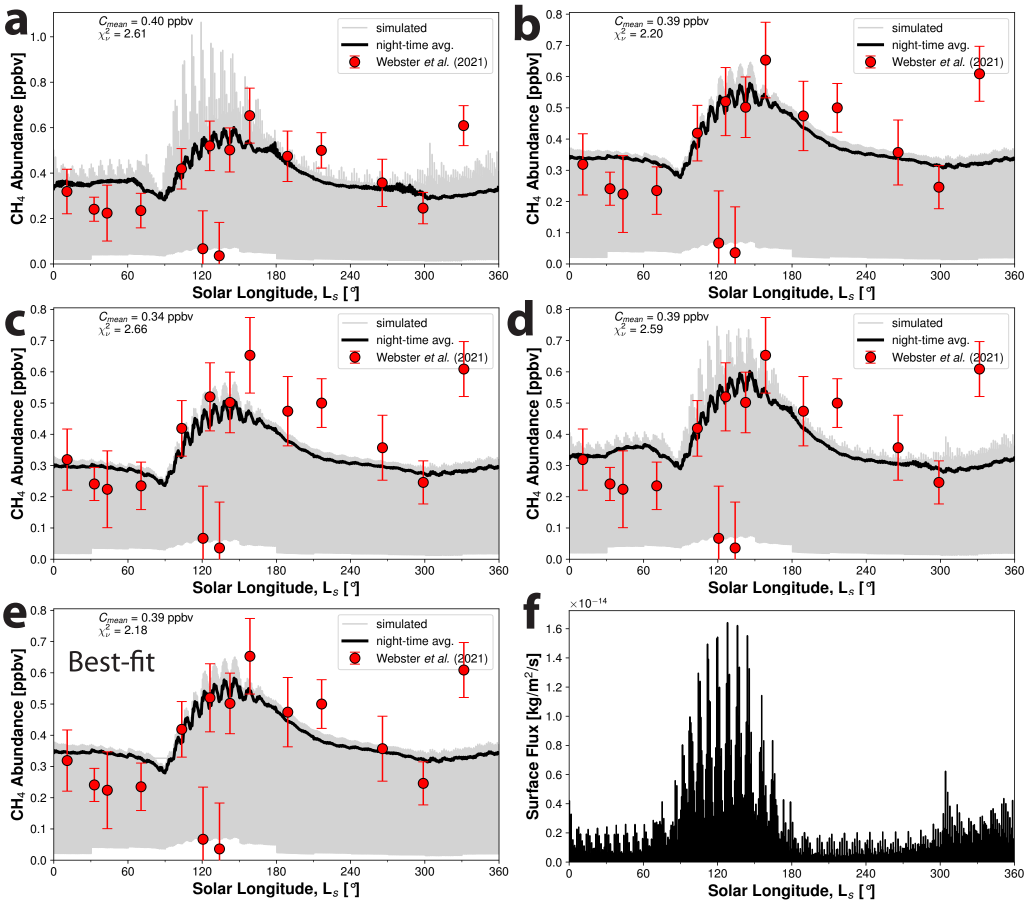

Figure 4. Composite of atmospheric mixing end-member scenarios simulating atmospheric methane abundance for the case with fracture density 0.010% showing seasonal methane variation. Panels **a-e** compare simulated (stars, lines) to measured (circles) atmospheric methane abundance values plotted against solar longitude, L_s [°]. Night-time averages of the simulated abundance (thick black line) are plotted to aid visualization because of the large diurnal variations present (gray band). Measured abundances are from Webster et al. (2021). Note that some measurements were collected in different Mars years. Panel letters **a-d** correspond to lettering of atmospheric transport parameter end-member scenarios described in Table 1 and Section 2.4.1. Panel **e** is the "best" fitting scenario (corresponds to top row in Table 1), and panel **f** is the surface methane flux.

surface flux pulses varies by fracture density case, dictated entirely by the subsurface architecture; i.e., the fracture topology. The surface flux pulses are produced in response to the small morning barometric pressure drop occurring at approximately 3:00, and the large mid-day pressure drop occurring between 7:40 and 16:00. If the subsurface were a homogeneous medium, we would expect a surface flux pulse roughly coincident with the pressure drop, having a Gaussian shape in time. This is actually observed in our model as fracture density increases: for example, in the case where fracture density = 0.035%, the surface flux has fewer individual spikes, and is characterized by a more "diffuse" flux pattern with center-of-mass near the middle of the large mid-day pressure drop (Figure S20f). The sparse fracture network in the present case (fracture density 0.01%) does not release methane at the surface in sync with the pressure drops – trace gases must work

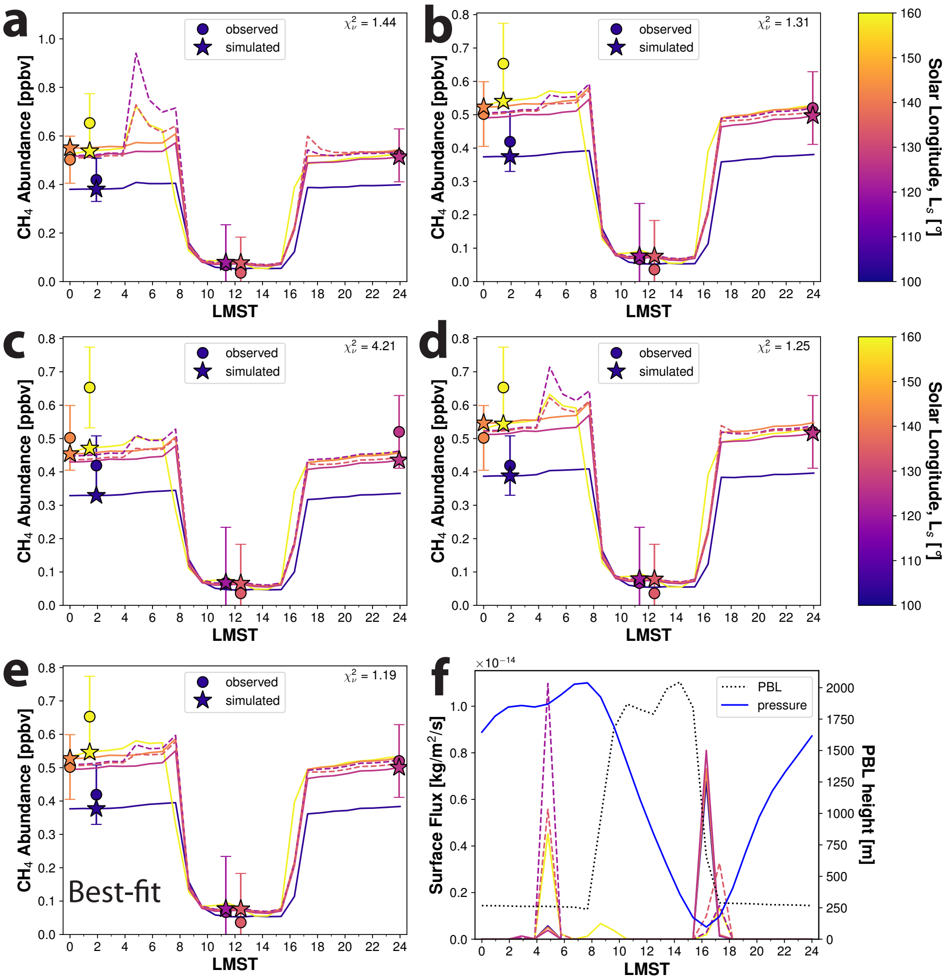

Figure 5. Composite of atmospheric mixing end-member scenarios simulating atmospheric methane abundance for the case with fracture density 0.010%. Panels **a-e** compare simulated (stars, lines) to measured (circles) atmospheric abundance values in local time, LMST, for northern summer, which highlights the day-night difference in abundance largely caused by the elevated planetary boundary layer (PBL) height h_{PBL}. Simulated abundances of the sols with non-detections are indicated by dashed lines. Measured abundances from Webster et al. (2021). Note that all measurements were taken on different sols and, in some cases, different Mars years, with the solar longitude, L_s [°] of the measurement indicated on the plot by its color. Panel letters **a-d** correspond to lettering of end-member scenarios described in Table 1 and Section 2.4.1. Panel **e** is the "best" fitting scenario (corresponds to the top row of Table 1), and panel **f** is the surface methane flux. Surface flux in local time (solid and dashed lines as above) plotted against PBL height (dotted line). Atmospheric pressure (blue line) is plotted without visible scale, but the minimum and maximum values shown are approximately 703 and 781 Pa, respectively. The pressure time series shown is from $L_s = 120.7°$; pressures on the dates of the other measurements are different but similar in shape. Comparison of derived crater mixing times (t_{ss}) calculated from D_c and D_e to estimated $t_{ss} = 1$ sol from Pla-García et al. (2019) indicate that scenarios a and d are likely to be more closely representative of actual conditions.

their way tortuously through individual fractures. The surface pressure wave propagates through the fractures and is attenuated by the rock matrix, leading to varying degrees of phase lag in the subsurface signal. Over multiple barometric pressure cycles, methane gas is brought closer to the surface through different fracture pathways – the variety of travel pathways leads to different surface breakthrough times depending on the pressure propagation and gas transport history within each fracture. This helps explain why the individual flux pulses shown in this case vary so much in magnitude despite being forced by relatively similar atmospheric pressures.

Examination of the end-member scenarios reveals some key differences imbued by the choice of atmospheric transport variables (Figure 5a-d). In terms of χ^2_ν, there is little to distinguish the end-member scenarios examined, although scenario c clearly performed worse than the rest over this time frame. Scenarios a and d used small values of D_c (of order ≤ 0.01 m^2 s^{-1}, which is on the order of magnitude implied by a 1-sol crater mixing time, and 2 orders of magnitude greater than binary CH_4-CO_2 diffusion), the effect of which is apparent in the rapid spike in methane abundance between 4:00 and 7:00 LMST. This spike is a direct result of the methane surface flux pulses occurring between 4:00 and 6:00 LMST; the smaller values of D_c cause the sensor at $z = 1$ m to more readily feel the effects of these pulses before they eventually mix by diffusion into the rest of the atmospheric column. The effect of these early morning methane pulses is greatly muted in scenarios b and c, which had much greater values for these mixing coefficients (of order ≥ 6 m^2 s^{-1}).

Considering these simulations in terms of crater mixing time (t_{ss}) of ~ 1 sol estimated by Pla-García et al. (2019) also favors the scenarios with smaller D_c. For an approximate collapsed-state PBL height of 250 m, mixing times for Table 1 scenarios are as follows: (best) 0.05 sols, (a) 4.3 sols, (b) 0.04 sols, (c) 0.07 sols, and (d) 0.75 sols. However, the collapsed state only accounts for part of each sol. The maximum diurnal PBL height during the expanded state varies from 2045 to 6017 m throughout the Mars year. For $\max h_{PBL} = 2045$ m – which occurs in northern summer – the inferred mixing time t_{ss} is: (best) 0.01 sols, (a) 0.8 sols, (b) 0.004 sols, (c) 0.14 sols, and (d) 0.28 sols. For $\max h_{PBL} =$ 6017 m – which occurs during northern winter – the inferred mixing time t_{ss} is: (best) 0.07 sols, (a) 6.56 sols, (b) 0.04 sols, (c) 1.18 sols, and (d) 2.4 sols. Scenarios a and d most closely approximate the presumed crater mixing time, though it should be noted that there can be significant variation in mixing times throughout the Mars year (Pla-García et al., 2019; Yoshida et al., 2022), and our atmospheric mixing model is not set up to account for these variations due to representing D_e with a single value.

We further interrogated the candidate solution parameter space generated by the differential optimization algorithm in order to understand the interaction between atmospheric mixing parameters, with results in Supporting Information section 7.4. Diffusion coefficients D_c and D_e, unsurprisingly, are positively correlated such that smaller D_c corresponds to a smaller D_e. The candidate solution space contains diffusion coefficient values such that range of the ratio D_e/D_c is between 59 and 678 (Figure S22), with a mean value of 351. We initially provided bounds to the algorithm for this ratio in $1 \leq D_e/D_c \leq 1000$, so the atmospheric mixing model apparently favors comparatively large daytime eddy diffusivities compared to those during the collapsed state, although the absolute magnitudes of these diffusivities do not overly affect the results in terms of error. A linear regression on $D_e = f(D_c)$ yields a slope of 10.8, with an adjusted R^2 value of 0.85. Also unsurprisingly, first-order methane loss rate parameters k_c and k_e are inversely correlated in order to preserve mass balance in time. The range of the ratio k_e/k_c is 1.01 to 3.21 (Table 1) having mean value 1.46, with the overall best scenarios in terms of error coming out of ratios close to unity. A linear regression on $k_e = f(k_c)$ yields a slope of -1.1, with an adjusted R^2 value of 0.67.

Effects of Dust Devil Pressure Drops on Flux Timing As part of making predictions about timing of atmospheric methane measurements, we also considered the effects of dust devil vortices on surface flux of methane in the vicinity of the rover. We considered this because *Curiosity* is currently climbing Aeolis Mons (a.k.a. Mt. Sharp), and will be doing so for the remainder of the mission. Observational data and Mars Weather Research and Forecasting (MarsWRF) General Circulation Model (Richardson et al., 2007) simulations of Gale crater indicate a gradual increase in vortex detections during most seasons as the *Curiosity* rover ascends the slopes of Aeolis Mons (Newman et al., 2019; Ordóñez-Etxeberria et al., 2020). The primary reason for this is related to the increase in topographic elevation, which encourages vortex formation because of the cooler near-surface daytime air temperatures (Newman et al., 2019). More discussion on this is provided in Supporting Information section 5.

We describe these dust devil simulations in the Supporting Information (section 5). We considered pressure drops associated with dust devils over a range of duration and intensity. As expected, the greatest surface flux is caused by dust devils with the longest duration (25 s) and largest pressure drop (5 Pa; Figure S11). However, the total mass of methane emitted in this scenario was 9.4×10^{-10} g, which has a negligible effect on atmospheric methane abundance in our model. Overall, dust devils likely do not make much of a difference in surface methane emissions. This makes sense, as the diurnal pressure variations by comparison have magnitude of order several 10s of Pa, with the primary pressure drop occurring over an interval of several hours. We can therefore likely ignore the effects of dust devils on overall timing of methane variations, which is encouraging since we are unable to predict the occurrence of individual vortices.

3.3 Implications for Future Measurements

Confirming and characterizing the apparent diurnal variability of methane has been highlighted by the SAM-TLS team as the next key step to understanding methane abundance and circulation at Gale crater. At the time of writing, Mars' northern summer period approaches, the timing of which is coincident with prior measurements that suggested subdiurnal methane variations (L_s 120-140°). This makes northern summer a prime candidate for potential corroboration of the hypothesized subdiurnal methane variations. The SAM wide range pumps have performed exceptionally well, and have already exceeded their flight lifetime requirements, but we need to be prudent in planning their use in future measurements. This compels the need to choose strategic sampling times in order to learn as much as possible about methane seepage and circulation patterns at Gale. Strategic atmospheric sampling using SAM-TLS during this upcoming time frame has the potential to validate and contextualize the results of our coupled subsurface-atmospheric mixing model as well as the previous measurements suggesting diurnal methane variations.

With the goal of more robustly characterizing diurnal methane variability, we would propose a set of enrichment runs in the period L_s 120-140°, which occurs September-October 2023. In the interest of conserving SAM pump life, we propose initially performing a minimum of two measurements. The first proposed measurement would establish a baseline for the second in addition to providing comparison to measurements conducted in previous MYs, while the second measurement would aim to extend the current characterization of diurnal methane variability. The measurements we propose would correspond to the approximate time of year of the previous two mid-sol samples, as well as the apparent generally-elevated methane abundance occurring in northern summer. Ideally, the samples would also be coordinated such that they coincide with TGO solar occultations on any of either 25 September, 27 September, 9 October, or 11 October 2023 for potential cross-comparison of measurements. Both enrichment runs should be performed identically to each other with the exception of local time conducted. A version of the dual-enrichment run modified slightly from the procedure of previous measurements (Webster et al., 2018a) would provide better quantification of background CH_4 and better conserve pump life without deviating significantly from previous run procedures (see Supporting Information section 3 for a more complete description of the modified procedure).

The first sample we propose should ideally be performed around L_s 126° to coincide with time-of-year of the previous MY positive detection on sol 2626, which was conducted between the two daytime non-detections in 2019 (Webster et al., 2021). This would serve as a baseline observation, both for the sake of comparison to the following measurement, as well as to the previously established baseline abundance for this period. Performing the measurement within the 23:00 - 3:00 LMST time range would make this measurement immediately comparable to most measurements from previous MYs, and additionally would refresh the baseline for the current MY and second run.

The second measurement would ideally be collected at a previously unmeasured time, and would be chosen to provide new insight into the methane emission and mixing mechanisms at play, in addition to extending the characterization of the apparent diurnal variability. We envision two primary candidate timing windows for this proposed measurement, which we hereafter refer to as I and II. Window I would take place between 6:30 - 10:00 LMST with the goal of further constraining the drop in observed methane abundance that seems to occur between midnight (0:00 LMST) and 11:20 LMST. Prior work using atmospheric transport models (Figure 8 in Viúdez-Moreiras, 2021; Moores, King, et al., 2019), in addition to the present work, predict that this drop occurs some time mid-/late-morning due to the upward extension of the PBL column and reversal of horizontal flows from convergent to divergent. A measurement in Window I would further constrain the timing of the apparent drop in methane abundance; for instance, elevated methane levels late in this window would aid the argument that PBL extension and the accompanying transition to divergent flows are strongly linked to the daytime drop in abundance. Methane abundance noticeably higher than the baseline measurement near midnight would imply additional flux in the intervening morning hours based on our model. However, if the magnitude of the difference is not overly large, it could be difficult to parse out the effects of a morning flux pulse (e.g., Figure 5a,d), gradual overnight methane accumulation, or simply sol-to-sol abundance variation.

Window II encompasses the time between 18:00-21:00 LMST, and a sample therein would serve to characterize the hypothesized rise in methane levels at sunset, post-PBL collapse (∼17:00). A measurement early in this window (18:00-19:00) could provide useful information regarding potential surface release mechanisms. If methane builds up rapidly to concentrations consistent with or above nighttime values, it could be indicative of daytime methane emissions, such as those caused by barometric pumping, though not exclusively due to this mechanism. Along that line, methane abundance noticeably greater than nighttime values (e.g., Figure S19a,d) would suggest either the occurrence of mid-/late-afternoon flux pulses, or that the magnitude of nighttime emissions is less than that estimated in other studies (or is nonexistent), both of which would also be consistent with barometric pumping. Abundances lower than observed nighttime values, on the other hand, could suggest gradual evening/overnight methane accumulation, which may point to an emission mechanism other than barometric pumping, which produces primarily daytime fluxes.

4 Conclusions

This study investigates the transport of subsurface methane in fractured rock into Mars' atmosphere driven by barometric pressure fluctuations at Gale crater. The subsurface seepage model is coupled with an atmospheric mixing model in order to simulate atmospheric concentrations within an evolving planetary boundary layer column in response to transient surface emissions and compares them to MSL abundance measurements. Atmospheric transport variables are chosen by an optimization routine such that they minimize the error compared to SAM-TLS measurements, which include seasonal and sub-diurnal abundance variations. The simulations are evaluated based on how well they represented seasonal and diurnal variations in atmospheric methane concentrations, including daytime non-detections observed by MSL. Part of the investigation involves simulating subsurface transport in rocks covering a range of fracture densities. To that end, a lower bound on subsurface fracture density of 0.01% is established, below which the seasonal atmospheric variations driven by barometric pumping are out-of-phase with observations.

We examine the sub-diurnal atmospheric methane variations produced by our simulations in Mars' northern summer, a time period chosen due to its coincidence with previous measurements suggesting the presence of large diurnal abundance fluctuations. Several key features were identified in the best-performing simulations. Simulations indicated a pre-dawn methane surface flux pulse (4:00-6:00 LMST) that may be detectable before PBL thickness increases and upslope (divergent) circulation develops. Detection of a large methane spike would be suggestive of barometric pumping, and would add to the evidence supporting a localized emission source in the interior of Gale crater, such as the highly fractured Murray outcrops as mentioned in Viúdez-Moreiras et al. (2021). Another feature identified was a large abundance depression during mid-sol between 11:00 - 17:00 coincident with PBL extension and divergent slope flows, followed by a rapid rebound in methane abundance following PBL collapse in the early evening. As a way to test our proposed transport mechanism and extend the current characterization of diurnal methane variation, we propose a set of two SAM-TLS enrichment measurements for the middle of Mars' northern summer (L_s = 120-140°), with the option of either a mid-/late-morning or an early-evening measurement. Each measurement has high potential to better-constrain the current understanding of the timing of either the apparent morning drop in methane or evolution of nighttime methane increase, respectively, and the measurements both have modest potential to incrementally suggest or refute the influence of a barometric pumping mechanism on diurnal methane variations at Gale crater.

The modeled methane abundances presented in this work are controlled by two factors: the subsurface transport pattern driven by barometric pumping and the PBL dynamics. Though driven by the same barometric signal, surface methane flux patterns in our model varied significantly with subsurface architecture (i.e., fracture density). Fracture density controls the degree to which the atmospheric pressure signal propagates into the subsurface, both in terms of overall depth and phase response. So important is the communication of the atmospheric pressures with the subsurface that cases we considered with very low fracture density ($\leq$ 0.005%) produced surface flux and abundance patterns that were almost completely out of phase with SAM-TLS observations. In our coupled atmospheric mixing model, we chose a handful of atmospheric transport parameters to approximately describe the PBL mixing dynamics, which essentially controlled the rate at which mixing from the surface methane emission would occur in the atmospheric column at different times of day. The atmospheric methane abundance was highly sensitive to these parameters, which exerted a great influence on both the seasonal and sub-diurnal abundance patterns. Despite this, our sensitivity analysis showed that no combination of atmospheric transport parameters in our model could generate abundances that were in-phase with the observed patterns for the low fracture density cases ($\leq$ 0.005%). This implies an important interplay between the influence of subsurface geology and atmospheric conditions on methane fluctuations at Gale in that only specific surface flux patterns are capable of producing the observed atmospheric variations, at least in the case where the rover is located within the emission area. Three-dimensional atmospheric dispersion modeling investigating transport from more distant emission areas, such as that in Viúdez-Moreiras et al. (2021), might be able to further contextualize the extent of this relationship.

Acknowledgments

We thank C. R. Webster and D. Lo for their comments regarding technical details of the modified dual-enrichment run procedure.

This research was supported by the Los Alamos National Laboratory (LANL) through its Center for Space and Earth Science (CSES). CSES is funded by LANL's Laboratory Directed Research and Development (LDRD) program under project number 20210528CR.

Pressure and temperature data described in the paper are further described in the supplementary materials and were acquired from NASA's Planetary Data System (PDS) at the following address: `https://atmos.nmsu.edu/PDS/data/mslrem_1001/DATA/`.

Open Research

Data Availability Statement

PDS data products from the Mars Science Laboratory (MSL) Rover Environmental Monitoring Station (REMS) were used for the analysis in this paper. The MSL REMS Models Reduced Data Record (MODRDR) provided the atmospheric pressure measurements for our simulations.

Software Availability Statement

Figures were made with Matplotlib version 3.2.2 (Hunter, 2007) available under the Matplotlib license at `https://matplotlib.org/`. The FEHM software (Zyvoloski, 2007; Zyvoloski et al., 2017) version 3.4.0 (`https://fehm.lanl.gov`) associated with this manuscript for the simulation of gas flow and transport is published on GitHub `https://github.com/lanl/FEHM/tree/v3.4.0`.

References

Adamson, A. A. (1979). *A Textbook of Physical Chemistry (Second Edition)* (Second ed.). Academic Press. doi: 10.1016/B978-0-12-044262-1.50028-1

Atreya, S. K., Mahaffy, P. R., & Wong, A. S. (2007). Methane and related trace species on Mars: Origin, loss, implications for life, and habitability. *Planetary and Space Science*, *55*(3), 358–369. doi: 10.1016/j.pss.2006.02.005

Ballou, E. V., Wood, P. C., Wydeven, T., Lehwalt, M. E., & Mack, R. E. (1978). Chemical interpretation of Viking Lander 1 life detection experiment. *Nature*, *271*(5646), 644–645. doi: 10.1038/271644a0

Bevington, P. R. (1969). *Data Reduction and Error Analysis for the Physical Sciences.* New York: McGraw-Hill.

Birdsell, D. T., Rajaram, H., Dempsey, D., & Viswanathan, H. S. (2015). Hydraulic fracturing fluid migration in the subsurface: A review and expanded modeling results. *Water Resources Research*, *51*(9), 7159–7188. doi: 10.1002/2015WR017810

Bourret, S. M., Kwicklis, E. M., Harp, D. R., Ortiz, J. P., & Stauffer, P. H. (2020). Beyond Barnwell: Applying lessons learned from the Barnwell site to other historic underground nuclear tests at Pahute Mesa to understand radioactive gas-seepage observations. *Journal of Environmental Radioactivity*, *222*, 1–14. doi: 10.1016/j.jenvrad.2020.106297

Bourret, S. M., Kwicklis, E. M., Miller, T. A., & Stauffer, P. H. (2019). Evaluating the Importance of Barometric Pumping for Subsurface Gas Transport Near an Underground Nuclear Test Site. *Vadose Zone Journal*, *18*(1), 1–17. doi: 10.2136/vzj2018.07.0134

Carrigan, C. R., Heinle, R. A., Hudson, G. B., Nitao, J. J., & Zucca, J. J. (1996). Trace gas emissions on geological faults as indicators of underground nuclear testing. *Nature*, *382*(6591), 528–531. doi: 10.1038/382528a0

Carrigan, C. R., Heinle, R. A., Hudson, G. B., Nitao, J. J., & Zucca, J. J. (1997). *Barometric Gas Transport Along Faults and Its Application to Nuclear Test-Ban Monitoring* (Tech. Rep. No. May). Lawrence Radiation Laboratory.

Carroll, S. A., Keating, E., Mansoor, K., Dai, Z., Sun, Y., Trainor-Guitton, W., ... Bacon, D. (2014). Key factors for determining groundwater impacts due to leakage from geologic carbon sequestration reservoirs. *International Journal of Greenhouse Gas Control*, *29*, 153–168.

Carslaw, H. S., & Jaeger, J. C. (1959). *Conduction of Heat in Solids* (2nd ed.). Oxford: Clarendon Press.

Chaix, L., & Dominé, F. (1997). Effect of the thermal history of ice crushed at 77 K on its surface structure as determined by adsorption of CH4 at low surface coverage. *Journal of Physical Chemistry B*, *101*(32), 6105–6108. doi: 10.1021/jp963247k

Chaudhuri, A., Rajaram, H., & Viswanathan, H. (2013). Early-stage hypogene karstification in a mountain hydrologic system: A coupled thermohydrochemical model incorporating buoyant convection. *Water Resources Research*, *49*(9), 5880–5899. doi: 10.1002/wrcr.20427

Clemo, T. M., & Smith, L. (1997). A hierarchical model for solute transport in fractured media. *Water Resources Research*, *33*(8), 1763–1783.

Colwell, F. S., Boyd, S., Delwiche, M. E., Reed, D. W., Phelps, T. J., & Newby, D. T. (2008). Estimates of biogenic methane production rates in deep marine sediments at Hydrate Ridge, Cascadia margin. *Applied and Environmental Microbiology*, *74*(11), 3444–3452. doi: 10.1128/AEM.02114-07

Dempsey, D., Kelkar, S., & Pawar, R. (2014). Passive injection: A strategy for mitigating reservoir pressurization, induced seismicity and brine migration in geologic CO2 storage. *International Journal of Greenhouse Gas Control*, *28*, 96–113.

Etiope, G., Drobniak, A., & Schimmelmann, A. (2013). Natural seepage of shale gas and the origin of " eternal flames" in the Northern Appalachian Basin, USA. *Marine and Petroleum Geology*, *43*, 178–186. doi: 10.1016/j.marpetgeo.2013.02.009

Etiope, G., & Martinelli, G. (2002, feb). Migration of carrier and trace gases in the geosphere: An overview. *Physics of the Earth and Planetary Interiors*, *129*(3-4), 185–204. doi: 10.1016/S0031-9201(01)00292-8

Etiope, G., & Oehler, D. Z. (2019). Methane spikes, background seasonality and non-detections on Mars: A geological perspective. *Planetary and Space Science*, *168*(February), 52–61. doi: 10.1016/j.pss.2019.02.001

Fischer, H. B., List, E. J., Koh, R. C., Imberger, J., & Brooks, N. H. (1979). *Mixing in Inland and Coastal Waters*. San Diego: Academic Press.

Fu, P., Hao, Y., Walsh, S. D., & Carrigan, C. R. (2016). Thermal Drawdown-Induced Flow Channeling in Fractured Geothermal Reservoirs. *Rock Mechanics and Rock Engineering*, *49*(3), 1001–1024. doi: 10.1007/s00603-015-0776-0

Geier, J. E., Lee, K., & Dershowitz, W. S. (1988). Field validation of conceptual models for fracture geometry. *Transactions of American Geophysical Union*, *69*(44), 1177.

GEOS-Chem. (2023). [Software]. doi: 10.5281/zenodo.7696632

Giuranna, M., Viscardy, S., Daerden, F., Neary, L., Etiope, G., Oehler, D., ... Amoroso, M. (2019). Independent confirmation of a methane spike on Mars and a source region east of Gale Crater. *Nature Geoscience*, *12*(5), 326–335. doi: 10.1038/s41561-019-0331-9

Gloesener, E. (2019). *Methane clathrate hydrate stability in the martian subsurface and outgassing scenarios* (PhD thesis). Université Catholique de Louvain.

Gough, R. V., Tolbert, M. A., McKay, C. P., & Toon, O. B. (2010). Methane adsorption on a martian soil analog: An abiogenic explanation for methane variability in the martian atmosphere. *Icarus*, *207*(1), 165–174. Retrieved from http://dx.doi.org/10.1016/j.icarus.2009.11.030 doi: 10.1016/j.icarus.2009.11.030

Haagenson, R., & Rajaram, H. (2021). Seismic Diffusivity and the Influence of Heterogeneity on Injection-Induced Seismicity. *Journal of Geophysical Research: Solid Earth*, *126*(6). doi: 10.1029/2021JB021768

Harp, D. R., Bourret, S. M., Stauffer, P. H., & Kwicklis, E. M. (2020). Discriminating Underground Nuclear Explosions Leading To Late-Time Radionuclide Gas Seeps. *Geophysical Research Letters*, *47*(13), 1–8. doi: 10.1029/2019GL086654

Harp, D. R., Ortiz, J. P., Pandey, S., Karra, S., Anderson, D. N., Bradley, C. R., ... Stauffer, P. H. (2018). Immobile Pore-Water Storage Enhancement and Retardation of Gas Transport in Fractured Rock. *Transport in Porous Media*, 26. doi: 10.1007/s11242-018-1072-8

Holtslag, A. A. M., & Boville, B. A. (1993). Local versus nonlocal boundary-layer diffusion in a global climate model. *Journal of climate*, *6*(10), 1825–1842. doi: https://doi.org/10.1175/1520-0442(1993)006⟨1825:LVNBLD⟩2.0.CO;2

Hunter, J. D. (2007). Matplotlib: A 2D graphics environment [Software]. *Computing in Science & Engineering*, *9*(3), 90–95. doi: 10.5281/zenodo.3898017

Jones, E. G., Lineweaver, C. H., & Clarke, J. D. (2011). An extensive phase space for the potential Martian biosphere. *Astrobiology*, *11*(10), 1017–1033. doi: 10.1089/ast.2011.0660

Jordan, A. B., Stauffer, P. H., Knight, E. E., Rougier, E., & Anderson, D. N. (2015). Radionuclide Gas Transport through Nuclear Explosion-Generated Fracture Networks. *Nature Scientific Reports*, *5*(December), 1–10. doi: 10.1038/srep18383

Jordan, A. B., Stauffer, P. H., Zyvoloski, G. A., Person, M. A., MacCarthy, J. K., & Anderson, D. N. (2014). Uncertainty in Prediction of Radionuclide Gas Migration from Underground Nuclear Explosions. *Vadose Zone Journal*, *13*(10), 1–13. doi: 10.2136/vzj2014.06.0070

Klusman, R. W., Luo, Y., Chen, P., Yung, Y. L., & Tallapragada, S. (2022). Seasonality in Mars atmospheric methane driven by microseepage, barometric pumping, and adsorption. *Icarus*, *383*(May), 115079. Retrieved from https://doi.org/10.1016/j.icarus.2022.115079 doi: 10.1016/j.icarus.2022.115079

Lewis, K. W., Peters, S., Gonter, K., Morrison, S., Schmerr, N., Vasavada, A. R., & Gabriel, T. (2019). A surface gravity traverse on Mars indicates low bedrock density at Gale crater. *Science*, *363*(6426), 535–537. doi: 10.1126/science.aat0738

Lin, J. T., & McElroy, M. B. (2010). Impacts of boundary layer mixing on pollutant vertical profiles in the lower troposphere: Implications to satellite remote sensing. *Atmospheric Environment*, *44*(14), 1726–1739. Retrieved from http://dx.doi.org/10.1016/j.atmosenv.2010.02.009 doi: 10.1016/j.atmosenv.2010.02.009

Lin, J. T., Youn, D., Liang, X. Z., & Wuebbles, D. J. (2008). Global model simulation of summertime U.S. ozone diurnal cycle and its sensitivity to PBL mixing, spatial resolution, and emissions. *Atmospheric Environment*, *42*(36), 8470–8483. Retrieved from http://dx.doi.org/10.1016/j.atmosenv.2008.08.012 doi: 10.1016/j.atmosenv.2008.08.012

Luo, Y., Mischna, M. A., Lin, J. C., Fasoli, B., Cai, X., & Yung, Y. L. (2021). Mars Methane Sources in Northwestern Gale Crater Inferred From Back Trajectory Modeling. *Earth and Space Science*, *8*(11). doi: 10.1029/2021EA001915

Lyons, J. R., Manning, C. E., & Nimmo, F. (2005). Formation of methane on Mars by fluid-rock interaction in the crust. *Geophysical Research Letters*, *32*(13), 1–4. doi: 10.1029/2004GL022161

Mahaffy, P. R., Webster, C. R., Cabane, M., Conrad, P. G., Coll, P., Atreya, S. K., ... Others (2012). The sample analysis at Mars investigation and instrument suite. *Space Science Reviews*, *170*(1-4), 401–478.

Manning, C. E., & Ingebritsen, S. E. (1999). Permeability of the Continental Crust: Implications of Geothermal Data and Metamorphic Systems. *Reviews of Geophysics*, *37*(1), 127–150.

Martínez, G., Valero, F., & Vázquez, L. (2009). Characterization of the Martian surface layer. *Journal of the Atmospheric Sciences*, *66*(1), 187–198. doi: 10.1175/2008JAS2765.1

Martínez, G. M., Newman, C. N., De Vicente-Retortillo, A., Fischer, E., Renno, N. O., Richardson, M. I., ... Vasavada, A. R. (2017). The Modern Near-Surface Martian Climate: A Review of In-situ Meteorological Data from Viking to Curiosity. *Space Science Reviews*, *212*(1-2), 295–338. Retrieved from `http://dx.doi.org/10.1007/s11214-017-0360-x` doi: 10.1007/s11214-017-0360-x

Massmann, J., & Farrier, D. F. (1992). Effects of atmospheric pressures on gas transport in the vadose zone. *Water Resources Research*, *28*(3), 777–791. doi: 10.1029/91WR02766

Meslin, P. Y., Gough, R., Lefvre, F., & Forget, F. (2011). Little variability of methane on Mars induced by adsorption in the regolith. *Planetary and Space Science*, *59*(2-3), 247–258. doi: 10.1016/j.pss.2010.09.022

Moores, J. E., Gough, R. V., Martinez, G. M., Meslin, P. Y., Smith, C. L., Atreya, S. K., ... Webster, C. R. (2019). Methane seasonal cycle at Gale Crater on Mars consistent with regolith adsorption and diffusion. *Nature Geoscience*, *12*(5), 321–325. doi: 10.1038/s41561-019-0313-y

Moores, J. E., King, P. L., Smith, C. L., Martinez, G. M., Newman, C. E., Guzewich, S. D., ... Schuerger, A. C. (2019, aug). The Methane Diurnal Variation and Microseepage Flux at Gale Crater, Mars as Constrained by the ExoMars Trace Gas Orbiter and Curiosity Observations. *Geophysical Research Letters*, *46*(16), 9430–9438. doi: 10.1029/2019GL083800

Myers, T. (2012). Potential contaminant pathways from hydraulically fractured shale to aquifers. *Groundwater*, *50*(6), 872–882.

National Research Council. (1997). *Rock fractures and fluid flow: contemporary understanding and applications.* National Academies Press. doi: 10.1029/97eo00345

Neeper, D. A., & Stauffer, P. H. (2012a). Transport by Oscillatory Flow in Soils with Rate-Limited Mass Transfer: 1. Theory. *Vadose Zone Journal*, *11*(2), 1–14. doi: 10.2136/vzj2011.0093

Neeper, D. A., & Stauffer, P. H. (2012b). Transport by Oscillatory Flow in Soils with Rate-Limited Mass Transfer: 2. Field Experiment. *Vadose Zone Journal*, *11*(2), 1–12. doi: 10.2136/vzj2011.0093

Newman, C. E., Gómez-Elvira, J., Marin, M., Navarro, S., Torres, J., Richardson, M. I., ... Bridges, N. T. (2017). Winds measured by the Rover Environmental Monitoring Station (REMS) during the Mars Science Laboratory (MSL) rover's Bagnold Dunes Campaign and comparison with numerical modeling using MarsWRF. *Icarus*, *291*(December 2016), 203–231. Retrieved from `http://dx.doi.org/10.1016/j.icarus.2016.12.016` doi: 10.1016/j.icarus.2016.12.016

Newman, C. E., Kahanpää, H., Richardson, M. I., Martínez, G. M., Vicente-Retortillo, A., & Lemmon, M. T. (2019). MarsWRF Convective Vortex and Dust Devil Predictions for Gale Crater Over 3 Mars Years and Comparison With MSL-REMS Observations. *Journal of Geophysical Research: Planets*, *124*(12), 3442–3468. doi: 10.1029/2019JE006082

Nilson, R. H., Peterson, E. W., Lie, K. H., Burkhard, N. R., & Hearst, J. R. (1991). Atmospheric Pumping: A Mechanism Causing Vertical Transport of Contaminated Gases Through Fractured Permeable Media. *Journal of Geophysical Research: Solid Earth*, *96*(B13), 933–948. doi: 10.2752/147597509112541

Onstott, T. C., McGown, D., Kessler, J., Lollar, B. S., Lehmann, K. K., & Clifford, S. M. (2006). Martian CH4: Sources, Flux, and Detection. *Astrobiology*, *6*(2), 377–395.

Ordóñez-Etxeberria, I., Hueso, R., & Sánchez-Lavega, A. (2020). Strong increase in dust devil activity at Gale crater on the third year of the MSL mission and suppression during the 2018 Global Dust Storm. *Icarus*, *347*(February). doi: 10.1016/j.icarus.2020.113814

Ortiz, J. P., Rajaram, H., Stauffer, P. H., Harp, D. R., Wiens, R. C., & Lewis, K. W. (2022). Barometric pumping through fractured rock: A mechanism for venting deep methane to Mars' atmosphere. *Geophysical Research Letters*, *49*(14), e2022GL098946. doi: 10.1029/2022GL098946

Pan, L., Oldenburg, C. M., Pruess, K., & Wu, Y.-S. (2011). Transient CO2 leakage and injection in wellbore-reservoir systems for geologic carbon sequestration. *Greenhouse Gases: Science and Technology*, *1*(4), 335–350.

Pandey, S., & Rajaram, H. (2016). Modeling the influence of preferential flow on the spatial variability and time-dependence of mineral weathering rates. *Water Resources Research*, *52*(12), 9344–9366. doi: 10.1111/j.1752-1688.1969.tb04897.x

Parro, L. M., Jiménez-Díaz, A., Mansilla, F., & Ruiz, J. (2017). Present-day heat flow model of Mars. *Scientific Reports*, *7*(March 2017), 1–9. doi: 10.1038/srep45629

Pick, M. A. (1981). Kinetics of hydrogen absorption-desorption by niobium. *Physical Review B*, *24*(8), 4287.

Pla-García, J., Rafkin, S. C. R., Karatekin, O., & Gloesener, E. (2019). Comparing MSL Curiosity Rover TLS - SAM Methane Measurements With Mars Regional Atmospheric Modeling System Atmospheric Transport Experiments. *Journal of Geophysical Research : Planets*, *124*(8), 2141–2167. doi: 10.1029/2018JE005824

Press, W. H., Teukolsky, S. A., Vetterling, W. T., & Flannery, B. P. (2007). *Numerical Recipes: The Art of Scientific Computing* (3rd ed.). New York: Cambiridge University Press.

Putzig, N. E., & Mellon, M. T. (2007). Apparent thermal inertia and the surface heterogeneity of Mars. *Icarus*, *191*(1), 68–94. doi: 10.1016/j.icarus.2007.05.013

Rey, A., Belelli-Marchesini, L., Etiope, G., Papale, D., Canfora, E., Valentini, R., & Pegoraro, E. (2014, apr). Partitioning the net ecosystem carbon balance of a semiarid steppe into biological and geological components. *Biogeochemistry*, *118*(1-3), 83–101. doi: 10.1007/s10533-013-9907-4

Richardson, M. I., Toigo, A. D., & Newman, C. E. (2007). PlanetWRF: A general purpose , local to global numerical model for planetary atmospheric and climate dynamics. *Journal of Geophysical Research*, *112*(E9), 1–29. doi: 10.1029/2006JE002825

Rodrigo, R., Garcia-Alvarez, E., & Lopez-Gonzalez, M. (1990). Estimates of eddy diffusion coefficient in the Mars' atmosphere. *Atmosfera*, *3*(1), 31–43.

Stauffer, P. H., Rahn, T. A., Ortiz, J. P., Joseph, S. L., Boukhalfa, H., & Snyder, E. E. (2018). *Summary of a Gas Transport Tracer Test in the Deep Cerros Del Rio Basalts, Mesita del Buey, Los Alamos NM* (Tech. Rep.). Los Alamos National Laboratory.

Stauffer, P. H., Rahn, T. A., Ortiz, J. P., Salazar, L. J., Boukhalfa, H., Behar, H. R., & Snyder, E. E. (2019). Evidence for High Rates of Gas Transport in the Deep Subsurface. *Geophysical Research Letters*, *46*, 3773– 3780. doi: 10.1029/2019GL082394

Stevens, A. H., Patel, M. R., & Lewis, S. R. (2015). Numerical modelling of the transport of trace gases including methane in the subsurface of Mars. *Icarus*, *250*, 587–594.

Sun, Y., & Carrigan, C. R. (2014). Modeling Noble Gas Transport and Detection for The Comprehensive Nuclear-Test-Ban Treaty. *Pure and Applied Geophysics*, *171*, 735–750. doi: 10.1007/s00024-012-0514-4

Takle, E. S., Massman, W. J., Brandle, J. R., Schmidt, R. A., Zhou, X., Litvina, I. V., … Rice, C. W. (2004, aug). Influence of high-frequency ambient pressure pumping on carbon dioxide efflux from soil. *Agricultural and Forest Meteorology*, *124*(3-4), 193–206. doi: 10.1016/j.agrformet.2004.01.014

Tsang, Y. W., & Narasimhan, T. N. (1992). Effects of periodic atmospheric pressure variation on radon entry into buildings. *Journal of Geophysical Research: Solid Earth*, *97*(B6), 9161–9170.

Viswanathan, H. S., Pawar, R. J., Stauffer, P. H., Kaszuba, J. P., Carey, J. W., Olsen, S. C., … Guthrie, G. D. (2008). Development of a Hybrid Process and System Model for the Assessment of Wellbore Leakage at a Geologic CO2 Sequestration Site. *Environmental Science & Technology*, *42*(19), 7280–7286. doi: 10.1021/es800417x

Viúdez-Moreiras, D. (2021). A three-dimensional atmospheric dispersion model for Mars. *Progress in Earth and Planetary Science*, *8*(1). Retrieved from `https://doi.org/10.1186/s40645-021-00445-4` doi: 10.1186/s40645-021-00445-4

Viúdez-Moreiras, D., Arvidson, R. E., Gómez-Elvira, J., Webster, C., Newman, C. E., Mahaffy, P., & Vasavada, A. R. (2020). Advective Fluxes in the Martian Regolith as a Mechanism Driving Methane and Other Trace Gas Emissions to the Atmosphere. *Geophysical Research Letters*, *47*(3), 1–8. doi: 10.1029/2019GL085694

Viúdez-Moreiras, D., Richardson, M. I., & Newman, C. E. (2021). Constraints on Emission Source Locations of Methane Detected by Mars Science Laboratory. *Journal of Geophysical Research: Planets*, *126*(12). doi: 10.1029/2021JE006958

Webster, C. R., Mahaffy, P. R., Atreya, S. K., Flesch, G. J., Mischna, M. A., Meslin, P. Y., … Lemmon, M. T. (2015). Mars methane detection and variability at Gale crater. *Science*, *347*(6220), 415–417. doi: 10.1126/science.1261713

Webster, C. R., Mahaffy, P. R., Atreya, S. K., Moores, J. E., Flesch, G. J., Malespin, C., … Navarro-Gonzalez, R. (2018a). Background levels of methane in Mars' atmosphere show strong seasonal variations. *Science*, *360*(6393), 1093–1096.

Webster, C. R., Mahaffy, P. R., Atreya, S. K., Moores, J. E., Flesch, G. J., Malespin, C., … Vasavada, A. R. (2018b). [Supplementary Material] Background levels of methane in Mars' atmosphere show strong seasonal variations. *Science*, *360*(6393), 1093–1096. doi: 10.1126/science.aaq0131

Webster, C. R., Mahaffy, P. R., Pla-Garcia, J., Rafkin, S. C., Moores, J. E., Atreya, S. K., … Vasavada, A. R. (2021). Day-night differences in Mars methane suggest nighttime containment at Gale crater. *Astronomy and Astrophysics*, *650*(December 2019), 1–14. doi: 10.1051/0004-6361/202040030

Yoshida, N., Nakagawa, H., Aoki, S., Erwin, J., Vandaele, A. C., Daerden, F., … Patel, M. (2022). Variations in Vertical CO/CO2 Profiles in the Martian Mesosphere and Lower Thermosphere Measured by the ExoMars TGO/NOMAD: Implications of Variations in Eddy Diffusion Coefficient. *Geophysical Research Letters*, *49*(10), 1–9. doi: 10.1029/2022GL098485

Yung, Y. L., Chen, P., Nealson, K., Atreya, S. K., Beckett, P., Blank, J. G., … Worden, J. (2018). Methane on Mars and Habitability: Challenges and Responses. *Astrobiology*, *18*(10), 1221–1242. doi: 10.1089/ast.2018.1917

Zimmerman, R. W., & Bodvarsson, G. S. (1996). Hydraulic Conductivity of Rock Fractures. *Transport in Porous Media*, *23*(1), 1–30.

Zyvoloski, G. A. (2007). *FEHM: A control volume finite element code for simulating subsurface multi-phase multi-fluid heat and mass transfer* (Tech. Rep.). Los

Alamos, NM: Los Alamos National Laboratory.

Zyvoloski, G. A., Robinson, B. A., Dash, Z. V., Chu, S., & Miller, T. A. (2017). *FEHM: Finite Element Heat and Mass Transfer Code.* [Software] GitHub. Retrieved from https://github.com/lanl/FEHM/tree/v3.4.0

Zyvoloski, G. A., Robinson, B. A., Dash, Z. V., Kelkar, S., Viswanathan, H. S., Pawar, R. J., . . . Chu, S. (2021). *Software users manual (UM) for the FEHM application version 3.1-3X.* Los Alamos, NM: Los Alamos National Laboratory Report LA-UR-12-24493.

Zyvoloski, G. A., Robinson, B. A., Dash, Z. V., & Trease, L. L. (1999). *Models and Methods Summary for the FEHM Application* (Tech. Rep.). Los Alamos, NM: Los Alamos National Laboratory.

Journal of Geophysical Research: Planets

Supporting Information for

Sub-diurnal methane variations on Mars driven by barometric pumping and planetary boundary layer evolution

J. P. Ortiz[1,2], H. Rajaram[2], P. H. Stauffer[1], K. W. Lewis[3], R. C. Wiens[4], D. R. Harp[5]
[1]Energy and Natural Resources Security, Los Alamos National Laboratory, Los Alamos, NM, USA
[2]Dept. of Environmental Health and Engineering, The Johns Hopkins University, Baltimore, MD, USA
[3]Dept. of Earth and Planetary Sciences, The Johns Hopkins University, Baltimore, MD, USA
[4]Earth, Atmospheric, and Planetary Sciences, Purdue University, West Lafayette, IN, USA
[5]The Freshwater Trust, Portland, OR 97205, USA

Contents of this file

1. Generating Synthetic Pressures and Temperatures

To treat the problem more generally, we generated synthetic pressures and temperatures to use as boundary conditions in the simulations. Our first step in processing was to perform an elevation-pressure correction due to change in *Curiosity* rover's position in time. We gathered rover positional data, then calculated the relative pressure offset caused by elevation change using a simple air-static condition: $p(z) = p_0 + \rho_{air} g z$, where $p(z)$ is the adjusted air pressure [Pa], p_0 is the air pressure [Pa] at the landing site, ρ_{air} is approximate air density [kg m^{-3}] at the landing site, g is acceleration due to gravity [m s^{-2}], and z is the elevation [m] relative to the landing site. This procedure is described in detail in Ortiz et al. (2022).

We then performed an initial decomposition of the pressure and temperature data into the frequency domain using a Fast Fourier Transform (FFT) algorithm (Cooley & Tukey, 1965) to get a preliminary estimate of the dominant harmonic components. Plots showing the results of spectral decomposition are shown in Figure S1 and Figure S2.

To generate synthetic pressure and temperature records, we compose a summation of sinusoidal components described by their frequency (ω), amplitude ($\mathcal{A}$), and phase (γ). We determined the exact components to use by optimizing the root mean squared error of the synthetic data to the observed (elevation-adjusted) pressures and temperatures. We started with the dominant periods determined from the FFT decomposition above, and then and calibrated ω, $\mathcal{A}$, and γ by minimizing the root mean squared error (RMSE) using the differential evolution algorithm (Storn & Price, 1997). An initial calibration used a single diurnal amplitude for the barometric pressures (i.e., pressure amplitude of the diurnal component did not vary seasonally), which caused significant mismatch because the diurnal amplitudes are not constant throughout the Mars year. We therefore used a seasonally modulated synthetic barometric pressure signal, following Harp, Ortiz, and Stauffer (2019):

$$P_s(\theta) = \left(\mathcal{A}_d + \mathcal{A}_s \sin\left(\omega_s t + \gamma_s\right)\right) \sin\left(\omega_d t + \gamma_d\right), \tag{1}$$

where P_s is the synthetic signal, $\mathcal{A}_d$ is the mean diurnal amplitude of given frequency, $\mathcal{A}_s$ is the amplitude of the seasonal modulation, ω_d is the diurnal frequency, ω_s is the seasonal modulation frequency (seasonal period, $T_s = 1$ Mars year, where $\omega_s = 2\pi/T_s$), γ_d and γ_s are the phase shift of the dominant frequency and seasonal modulation, respectively, and $\theta = [\mathcal{A}_d, T_d, \gamma_d, \mathcal{A}_s, \gamma_s]$ is a vector containing the calibration parameters, for which we aim to minimize an objective function $F(\theta)$ comparing the measured pressures/temperatures to the synthetic values. It is the $(\mathcal{A}_d + \mathcal{A}_s \sin(\omega_s t + \gamma_s))$ term that captures the seasonal modulation about the mean dominant frequency. The objective function F minimized in the calibration is the root mean squared error.

2. Heat Flow Verification

In this section, we describe several heat flow verification tests that we performed. The purpose of these tests is two-fold: to ensure that the physics are represented correctly in the FEHM simulator, and to generate confidence in the formulation of our model, which sequentially coupled the heat model to the flow and transport model.

2.1. Conductive Heat Flow Verification

The first step in implementing temperature-dependent adsorption in FEHM is to verify that the heat flow model behaves as expected. We perform a heat flow verification test using a simple problem in a 1-meter square domain (Figure S5) with initial, uniform temperature $T_0 = 200°$C. From time $t > 0$, the top and right boundaries of the box are assigned a constant $T = 100°$C, with zero heat flux boundary conditions on the left and bottom boundaries. We then observe the temperature decay two observation points (Figure S5).

The analytical solution for the temperatures in this 2-D heat conduction problem is given by Carslaw and Jaeger (1959):

$$T = T_s + \frac{16(T_0 - T_s)}{\pi^2} \sum_{m=0}^{\infty} \sum_{n=0}^{\infty} \frac{(-1)^{m+n}}{(2m+1)(2n+1)} \cos\frac{(2m+1)\pi x}{2a} \cos\frac{(2n+1)\pi y}{2b} e^{-\alpha_{m,n} t} \tag{2}$$

where $\alpha_{m,n} = \frac{\kappa\pi^2}{4}\left[\frac{(2m+1)^2}{a^2} + \frac{(2n+1)^2}{b^2}\right]$ and the region is taken to be $-a < x < a$, $-b < y < b$.

2.2. Verification of Subsurface Temperatures

We then verify that we are able to reproduce the expected subsurface temperature variations driven by surface temperature changes predicted by an analytical solution. As thermal waves propagate through the subsurface, their amplitude diminishes exponentially with depth from the surface. In the analytical solution discussed in Jones, Lineweaver, and Clarke (2011), the surface heat variations can be modeled as sinusoidal curves:

$$T_s(t) = T_0 + \Delta T \cos(\omega t) \tag{3}$$

where T_s is the surface temperature, T_0 is the mean surface temperature, ΔT is the amplitude of temperature variation about the mean, and ω is the angular frequency ($\omega = 2\pi f$, where f is the frequency (i.e., cycles per sol, cycles per year) of the temperature signal. The subsurface temperatures are then given by:

$$T_{sub}(y,t) = T_0 + \Delta T \exp\left(-\frac{y}{d_\omega}\right) \cos\left(\omega t - \frac{y}{d_\omega}\right) \tag{4}$$

where y is depth beneath the surface [m], d_ω is the thermal skin depth ($d_\omega = \sqrt{\frac{2\alpha}{\omega}}$) where the thermal diffusivity $\alpha = \frac{\kappa}{\rho c_p}$, where κ is thermal conductivity, ρ is density, and c_p is specific heat capacity.

We simulated surface thermal wave propagation in to the subsurface using a homogeneous domain with the following properties: $\kappa = 2.5$ W/(m · K), $\rho = 2900$ kg m^{-3}, $c_p = 800$ J/(kg · K). For the surface forcing, we used a period of 1 day (period $= \frac{\omega}{2\pi}$), and $\Delta T = 10$ °C. Our results in Figure S7 show good agreement between simulated and analytical subsurface temperatures. We performed verification at several longer periods (up to annual) for temperature forcing that are not shown here, but likewise indicated good agreement with the analytical solution.

2.3. Pure Conduction vs Conduction-Convection

The adsorption mechanism is dependent on temperature, which is dependent on depth below ground surface and time. Using the surface temperatures collected by *Curiosity*, we simulate transient 2D heat flow in the subsurface by comparing simple conduction to matrix conduction/fracture convection in a single-fracture model. Because of the high level of mesh refinement required for accurate representation of heat flow, we wanted to be able to simulate the subsurface temperatures (with a fine mesh) using a 1-D model, implicitly ignoring the effects of fractures. To determine if this can be done with without sacrificing accuracy, we needed to show that convective heat transfer effects is negligible compared to the overall effects of conduction.

We compared the subsurface temperature perturbation depths for these cases to determine whether subsurface convection can be considered negligible. In the case that convection is negligible, we can likely perform separate simulations for heat flow and methane transport (sequential coupling) rather than perform a fully-coupled thermo-physico-chemical simulation, which would be more computationally demanding. It is likely that a pure conduction model will sufficiently capture the subsurface temperature behavior; previous work has estimated that the seasonal thermal skin depth does not extend down to more than a few meters (Mellon & Phillips, 2001; Meslin et al., 2011; Moores et al., 2019; Gough et al., 2010). Nevertheless, it was important for us to perform this check since the presence of fractures may cause the thermal skin depth to be deeper than previous estimates, at least along the fractures.

The pure, single-phase heat conduction equation is as follows:

$$\frac{\partial T}{\partial t} = \alpha \nabla^2 T \tag{5}$$

where T is the temperature [K], t is time [s], and α is the thermal diffusivity coefficient [m^2 s^{-1}] ($\alpha = \frac{\kappa}{c\rho}$, where κ is the thermal conductivity of the material [J s^{-1} m^{-1} K^{-1}], c is the specific heat capacity [J K^{-1} kg^{-1}], and ρ is the density of the material [kg m^{-3}]).

In the case where flowing air currents in porous media transport significant amounts of heat, the energy conservation equation for conduction-diffusion is as follows:

$$[(1-\phi)\rho_r c_{pr} + \phi \rho_v c_{pv}] \frac{\partial T}{\partial t} = \nabla \cdot (\kappa \nabla T) - \nabla \cdot (\vec{v} \rho_v h_v) \tag{6}$$

where ϕ is matrix porosity [–], ρ_i is the density for rock (r) or vapor (v) [kg m^{-3}], respectively, c_{pi} is the specific heat capacity for constituent i [J K^{-1} kg^{-1}], T is temperature [K], t is time [s], κ is thermal conductivity of the rock [J s^{-1} m^{-1} K^{-1}], h_v is the specific enthalpy of the vapor [m^2 s^{-2}], and ∇ is the gradient operator. The fluid velocity vector $\vec{v}$ is assumed to follow Darcy's law:

$$\vec{v} = -\frac{k}{\mu_v}\left(\nabla P - \rho_v \vec{g}\right), \tag{7}$$

where k is the rock permeability [m^2], μ_v is the dynamic vapor viscosity [Pa s], P is pressure [Pa], and $\vec{g}$ is the gravitational acceleration vector [m s^{-2}]. In (6), we assume instantaneous thermal equilibration between the rock and the fluid.

2.3.1. Thermal Péclet Number Analysis

The above result makes intuitive sense if we consider the thermal Péclet number, a dimensionless number that quantifies the relative importance of conduction and convection:

$$\mathrm{Pe}_T = \frac{uL}{\alpha} \tag{8}$$

where u is the fluid flow velocity [m s^{-1}], L is the characteristic length [m], and α is the thermal diffusivity [m^2 s^{-1}] ($\alpha = \frac{\kappa}{\rho c_p}$, where κ is the thermal conductivity, ρ is the bulk density, and c_p is the specific heat capacity).

We calculate an approximate velocity of air flow (u) in the subsurface using the single-fracture, double-porosity pressure response solution in (Equation 8 in Nilson et al., 1991). The air flow velocity is the key quantity in heat convection for this problem, and we assume that the air flow is driven by the barometric pressure gradient at ground surface. We use representative values for a diurnal pressure perturbation (period = 1 sol, $\Delta P = 40$ Pa, mean pressure $P_0 = 800$ Pa). For the subsurface we use properties representative of our flow and transport simulations: fracture aperture $\delta_f = 1$ mm, fracture spacing $\delta_m = 5$ m, matrix permeability $k_m = 10^{-14}$ m^2, and matrix porosity $\phi_m = 0.35$. To estimate the air flow velocity using equation 8 from Nilson et al. (1991), we calculate the pressure gradient at 30 m and 5 m depth, with 2 mm lateral displacement from the fracture. We set the characteristic length L to the respective depth at which we calculated the flow velocity.

Rock Thermal Properties:

Rock thermal properties were taken as: density $\rho_r = 2900$ kg m^{-3}, thermal conductivity $\kappa_r = 2.7$ W / (m $\cdot$ K), and specific heat capacity $c_p = 800$ J / (kg $\cdot$ K). The rock thermal diffusivity α_r, then, is 1.16×10^{-6} m^2 s^{-1}.

Air Thermal Properties:

Mars air thermal properties were taken as: density $\rho_a = 0.018$ kg m^{-3}, thermal conductivity $\kappa_a = 0.01663$ W / (m $\cdot$ K), and specific heat capacity $c_p = 849$ J / (kg $\cdot$ K). The air thermal diffusivity α_a, then, is 1.03×10^{-3} m^2 s^{-1}.

Bulk Thermal Properties:

To estimate the thermal response of the subsurface as a whole, we calculate thermal properties of the subsurface in bulk, taking into account both the fluid (air) volume (V_a) and the solid volume (V_r). The bulk density $\rho_b = 1884$ kg m^{-3}, bulk thermal conductivity ($\kappa_b = (\kappa_a V_a + \kappa_r V_r)/V_{total}$) is 1.76 W / (m $\cdot$ K), and bulk specific heat capacity $c_p = 817$ J / (kg $\cdot$ K). The bulk thermal diffusivity α_b, then, is 1.14×10^{-6} m^2 s^{-1}.

At 30 m depth, the maximum velocity, u, in the matrix is 1.1×10^{-9} m s^{-1}. Using this depth for L, we calculate a thermal Péclet number of ~ 0.027, which indicates that conduction should dominate over convection. At 5 m depth, the maximum velocity $u = 3.1 \times 10^{-9}$ m s^{-1}. Using this depth for L, we calculate a thermal Péclet number of ~ 0.011, which similarly indicates that conduction should dominate over convection. This result is not surprising; one would expect that the heat capacity in the system is dominated by the matrix/rock solids rather than the low-density CO_2 carrier gas. Although air flow velocities in the fractures are orders of magnitude greater than the velocity in the rock matrix, the fractures make up a relatively small portion of the total porosity and, thus, a small portion of the energy transport. If the flowing fluid were a liquid, rather than a gas, a much greater portion of heat transport would be due to convection, and likely could not be considered negligible.

2.4. Effect of Temperature on Air Flow Properties

Due to increased computational costs associated with performing fully-coupled thermo-physico-chemical simulations, we chose to perform sequentially-coupled simulations by running heat flow first, then applying the calculated subsurface temperatures as boundary conditions for the adsorption mechanism in the flow and transport model. The temperatures are applied to the isothermal flow and transport simulations by varying the Langmuir adsorption coefficients in the adsorption process based on the ambient temperature. In reality, temperature would also affect fluid properties such as density and viscosity, which could affect flow and transport. From the CO_2 equation of state, we calculated that a 50 °C change in temperature results in only a 0.96% change in density from reference conditions $T = -50$°C and $P = 700$ Pa. The same temperature change results in a 22% change in viscosity. Although this seems like a large effect, the actual amplitude of the temperature changes in the subsurface is much smaller.

3. Modified Dual-Enrichment Run Procedure

The typical dual-enrichment run is described in Webster et al. (2018a). It involves first the evacuation of the Herriott cell, followed by opening of an inlet to the ambient atmosphere. The ingested atmospheric sample is passed through scrubbers to remove CO_2 and H_2O before entering the Herriott cell, eventually reaching 5–6 mbar after 2 hours. This results in an enrichment in the CH_4 by a factor of 25. The valve to the Herriott cell is then closed and 26 spectra are taken of the sample over ∼75 min. The Herriott cell is then evacuated and another 26 spectra are taken to record "empty cell" spectra to allow subtraction of any methane contribution from the foreoptics chamber. Finally, the Herriott cell is again filled up by opening another inlet to make a direct ingest of the atmosphere without passing the sample through scrubbers. A final 26 spectra are taken of the sample before the instrument is powered down (Figure S1 in Webster et al., 2018b). The entire process takes ∼8.5 hours (shorter in daytime from less heating required).

Prior to each run, the scrubbers are cleaned up by heating. This cleanup process typically takes 2 hours 21 min.

A slightly modified procedure would introduce two changes to the typical dual-enrichment run:

1. The direct ingest segment would be dropped. The direct ingest measurements were a low-resource way to observe CH_4 spikes in coordination with TGO measurements, but this is not expected to be very useful in answering the question at hand. Leaving out the direct ingest segment would conserve pump life and reduce the runtime of the experiment by ∼100 min to ∼7 hours.

2. Spectra would be taken over the two hours as the Herriott cell is being filled for the enriched measurements ("ingest scans"). These scans would be taken at the same cadence as the sets of 26 scans. These ingest scans serve two purposes. Firstly, they can also provide another way of quantifying the background CH_4 levels. Secondly, the scans could be used to detect any drastic changes in the ambient VMR that may occur.

The long duration of the enrichment run and the scrubber cleanup, in addition to the large power requirements, make it difficult to conduct more than one run within a single sol. The next best thing would be to conduct both of our proposed dual-enrichment runs as close together as possible in order to reduce the likelihood of significant changes in local weather conditions or other factors that could impact the assumed diurnal cycle of methane at Gale.

4. Diffusive Atmospheric Mixing Model

We attempt to visually illustrate the implementation of the atmospheric diffusion model within an expanding/contracting domain (Figure S10).

We initially took a more simplified approach to the atmospheric mixing model by assuming that methane released into the column mixed instantaneously across its entire height, as was done in Moores et al. (2019). The atmospheric methane concentration is then controlled predominantly by the PBL height varying in time, as this controls the mixing volume. An issue with this approach is that the mixing time is so fast that individual methane flux pulses are not observable in terms of the resulting abundance that would be measured by SAM-TLS. While instantaneous mixing may be a reasonable approximation for when PBL conditions are extremely unstable (Lin & McElroy, 2010), a partial mixing diffusive model is likely more representative of mixing under general atmospheric conditions in response to highly transient surface flux pulses.

5. Dust Devil-Induced Flux Simulations

A gradual increase in dust devil activity has been predicted by previous research (Richardson et al., 2007) as *Curiosity* climbs the slopes of *Aeolis Mons* for the remainder of its campaign. rooted in the mechanisms behind dust devil formation. Dust devils are convective vortices that occur during periods of strong convective heating of the ground surface, specifically when the ground temperature exceeds the ambient air temperature. Heating of the ground surface warms the air directly above it, causing the air to rise. As the air rises, any existing vorticity becomes more vertical and more intense, developing a low-pressure zone at the vortex core surrounded by strong tangential winds. The winds can be assisted by the suction effect imbued by the pressure drop. Lower thermal inertias, a property representing the ability of a material to conduct and store heat, of the ground surface can be a contributing factor to increased dust devil activity, since such conditions favor larger differences between the ground and air temperatures. However, Newman et al. (2019) found that this effect was less important overall than the increase in topographic elevation, which encourages vortex formation because of the cooler near-surface daytime air temperatures.

To investigate the effects of dust devils on surface methane flux, we simulated methane transport induced by pressure drops with a range of properties representative of the REMS pressure drop data analyzed by Ordóñez-Etxeberria, Hueso, and Sánchez-Lavega (2020). From Ordonez-Etxeberria, Hueso, and Sánchez-Lavega (2018), pressure drops in the REMS record are defined by two parameters: intensity of the pressure drop, and its duration. Individual pressure drop events are extracted by numerically describing the data in terms of these parameters by fitting the pressure data with a Gaussian function in a moving window of 60 s:

$$P(t) = P_0 - \Delta P \cdot \exp\left[-\left(\frac{t-t_0}{\sigma}\right)^2\right] \tag{9}$$

where $P(t)$ is the pressure as a function of time [Pa], P_0 is the baseline/ambient pressure [Pa], ΔP is the intensity of the pressure drop [Pa] computed as the difference between P_0 and the minimum pressure value, t_0 is the time corresponding to the pressure minimum [s], and σ is related to the duration, or Full Width at Half Maximum (FWHM) of the Gaussian through $FWHM = 2\sqrt{\ln 2}\sigma$.

5.1. Boundary and Initial Conditions: Dust Devil Simulations

Because pressure drops measured by REMS typically last on the order of seconds, they require highly refined temporal resolution to simulate properly, which is numerically intensive. Therefore, rather than run multi-year scenarios with sub-second temporal resolution, we estimate the upper bounds of fluxes that could be generated by performing truncated simulations (120 s) with high temporal resolution using conditions ideal for inducing subsurface gas flux (i.e., the best case scenario for generating flux). We performed the dust devil simulations after our running our preliminary subsurface-atmosphere model simulations so that we would only have to consider fracture-rock architectures that best matched the observed atmospheric methane abundances. We populate the subsurface initially with a uniform methane concentration equal to the maximum near-surface concentration achieved in the corresponding subsurface-atmospheric transport model at steady-state. So doing essentially represents the time of year with the highest methane concentrations in the shallow subsurface, and thus the chance for the greatest fluxes vented to the atmosphere for a given drop in pressure. We prescribe an initial atmospheric pressure equal to the mean surface pressure at Gale crater. We then perform a suite of simulations with dust devil duration (FWHM) ranging from 5 to 25 s, and pressure drops ranging from 1 to 5 Pa. The timing of the pressure drop minimum (t_0) occurs halfway through the 120 s simulation.

5.2. Dust Devil Pressure Drop Results

6. Fracture Network

6.1. Fracture Generation Algorithm

We randomly generated orthogonal discrete fractures using the 2-D Lévy-Lee algorithm (Clemo & Smith, 1997), a fractal-based fracture model (Geier et al., 1988). In this model, fracture centers are created sequentially by a "Lévy flight" process, – a termed coined by Benoît Mandelbrot and named for Paul Lévy – in which the step lengths in a random walk follow the heavy-tailed Lévy distribution

(Viswanathan et al., 1999). In a similar manner, fracture center locations in the Lévy-Lee algorithm are produced by random walk, and the distance between fracture centers L' is sampled from the power law distribution:

$$P_L(L' > L) = L^{-D} \tag{10}$$

where D is a specified fractal dimension. The direction of the separation between fracture centers is uniformly distributed between 0° and 360°. Fracture length and the variation in orientation are proportional to the distance from the previous fracture. The Lévy-Lee model generates a fracture network with a continuum of scales for both fracture length and spacing between fractures and uses the same exponent for fracture trace length and spacing. Structurally, the fracture networks generated by the Lévy-Lee algorithm tend to have clusters of fractures, with tighter clusters resulting from larger values of D. Since individual fracture lengths are assigned stochastically, we generated fracture networks with the desired fracture densities using a differential evolution optimization approach (Storn & Price, 1997) to determine the number of fractures required in each domain.

This mesh was then mapped onto a 3-D grid and extended across the width of the domain in the y direction – a single cell across – since FEHM does not solve true 2-D problems. This mapping essentially embeds the fractures in the rock matrix via upscaling of properties, allowing transfer of fluids and tracers to occur at the fracture-matrix interface. This mesh was then mapped onto a uniform grid.

6.2. Fracture Network Topology

The fracture network used in this study was designed to be representative of a fractured subsurface on Mars. Without rock cores or detailed logs, we know very little about fracture networks on Mars below the surface, though it is believed to be highly fractured (Figure S12). We want to generate a fracture network such that it would have a fracture density (i.e., the ratio of fracture volume to bulk rock volume) comparable to that in Mars' subsurface. Because the subsurface on Mars is so poorly characterized, we have made estimates of the fracture density based on rover photographs depicting surface expressions of fracture networks at Gale crater using a fracture trace method (Figure S13). Because the observed surface is roughly two-dimensional – and also due to the 2-D nature of our model – we calculate an "areal fracture density" (the ratio of fracture area to bulk rock area) and assume a similar fracture distribution in cross-section. We track the area of the fracture traces relative to the total image area using a script in Adobe Illustrator (Adobe Inc., 2019). The calculated areal fracture density of the fracture network in Figure S13 was $\sim 0.1\%$. In reality, the subsurface on average will be less fractured than this view of the surface, so we consider fracture densities in our simulations in the range 0.0% to 0.035%.

7. Additional Results

To conserve space in the main text, we here include several results additional from the coupled subsurface-atmospheric mixing model, as well as results examining parameter combinations within the candidate solution space.

7.1. Out-of-Phase Methane Variations

We observed that subsurface architectures with fracture density $\leq 0.005\%$ produced seasonal methane variations that were out of phase with the SAM-TLS observations. We here include the "best" scenarios associated with of these fracture density cases.

7.2. Seasonal Methane Variation

7.2.1. Fracture Density 0.02% and 0.035%

Other subsurface fracture cases that performed well were 0.035% (Figure S18) and 0.02% (Figure S17) fracture density, in that order. Compared to 0.01% fracture density, both of these higher fracture density cases better match the abundance observations in Northern Spring (L_s 0-90°). These cases also tended to better capture the increase in methane abundance that seems to occur in Northern Winter (L_s 270-360°), especially the case with fracture density 0.035%. That being said, methane abundance in these higher fracture density cases tends to fall off quicker as Northern Summer transitions into Northern Autumn, generally underpredicting methane concentrations relative to the apparent gradual decline in methane observed. The rapid fall-off is less pronounced for fracture density 0.02% versus 0.035%, which can be seen when comparing the fit to the SAM-TLS observation at $L_s = 189.2°$.

7.3. Sub-diurnal Methane Variation

7.3.1. Fracture Density 0.02% and 0.035%

Fracture networks that are less sparse (e.g., fracture density 0.02 and 0.035%, which compared to the 0.01% case have 2 and 3.5 times greater volume of fractures, respectively) produce flux patterns that are more diffuse (Figures S20f, S19f). The surface emissions in such cases are characterized by more frequent pulses of methane because transport through individual fracture pathways is less important than the overall contribution of multiple connected pathways. The resulting atmospheric abundances are, likewise, necessarily different than for cases with more sparse fracture networks (Figures S19, S20).

For fracture density 0.02%, smaller values of D_c (≤ 0.2 m^2 s^{-1}) better matched the inferred diurnal abundance variation. Such scenarios were in general agreement with SAM-TLS observations, with the exception of the intermediate positive detection on L_s 126.3° (at 23:56 LMST) mentioned in the previous section. Early-evening methane (17:00 - 21:00) pulses at certain L_s create methane abundance spikes that tend to quickly decay to background as the evening progresses. It is worth noting that the candidate parameter space for this fracture case was relatively small with regard to the range of D_c ($0.06 < D_c < 1.2$).

For fracture density 0.035%, larger values of D_c (≥ 1 m^2 s^{-1}) tended to better match the inferred diurnal abundance variation, though this relationship was not firm, as evidence by scenario c. As above, however, it is worth noting that the candidate parameter space for this fracture case was relatively small with regard to the range of D_c ($0.10 < D_c < 1.4$). In terms of surface methane flux, the majority of mass emitted occurs mid-sol, between the hours of 10:00 and 17:00 LMST (Figure S20f). A rising limb of methane abundance culminating in a sharp "lip" occurs just prior to PBL expansion due to a late morning methane flux pulse. There is also a smaller, less pronounced lip and falling limb that occurs just after PBL collapse, which is primarily due a sharp methane pulse occurring at that time. The lip and falling limb is due to this pulse and not because the bulk of methane is emitted mid-sol during the expanded PBL state, as evidenced by the late-season abundance ($L_s = 156.3°$), which has no corresponding pulse and likewise, no early-evening falling limb.

7.4. Analysis of Candidate Parameter Space

We further interrogated the candidate solution parameter space generated by the differential evolution optimization algorithm in order to understand the interaction between atmospheric mixing parameters, with results below. We analyzed the parameter space for fracture density cases where the overall χ^2_ν for the "best" set of parameters was less than 4.0. This choice of error value was somewhat arbitrarily chosen, as it appeared to be the cutoff error, over which the seasonal abundance variations were out of phase with the observations. This cutoff thereby limited the best fracture densities to 0.01%, 0.02%, and 0.035%. Candidate solutions in each case were populated from the results of the differential evolution optimization by including results with error $\chi^2_\nu \leq \min \chi^2_\nu + 0.5$ – this defines the "candidate solution parameter space".

7.4.1. Fracture Density 0.01%

The entire candidate solution parameter space is shown in Figure S21. Diffusion coefficients D_c and D_e, unsurprisingly, are correlated such that smaller D_c begets a smaller D_e. The candidate solution space contains diffusion coefficient values such that range of the ratio D_e/D_c is between 59 and 678 (Figure S22), with a mean value of 351. We initially provided bounds to the algorithm for this ratio of $1 \leq D_e/D_c \leq 1000$, so the atmospheric mixing model apparently favors comparatively large daytime eddy diffusivities compared to those during the collapsed state, although the absolute magnitudes of these diffusivities do not overly affect the results. A linear regression on $D_e = f(D_c)$ yields a slope of 10.8, with an adjusted R^2 value of 0.85. Also unsurprisingly, first-order methane loss terms k_c and k_e are inversely correlated in order to preserve mass balance in time. The range in the ratio of k_e/k_c is 1.01 to 3.21 having mean value 1.46, with the overall best scenarios in terms of error coming out of ratios close to unity. A linear regression on $k_e = f(k_c)$ yields a slope of -1.1, with an adjusted R^2 value of 0.67.

7.4.2. Fracture Density 0.02%

The candidate solution space contains diffusion coefficient values such that range of the ratio of D_e/D_c is between 848 and 873 (Figure S24), with a mean value of 862. A linear regression on $D_e = f(D_c)$ yields a slope of 9.91, with an adjusted R^2 value of 1.00. The range in the ratio of k_e/k_c is 1.00 to 1.52 having mean value 1.12, with the overall best scenarios in terms of error coming out of ratios close to unity. First-order methane loss terms k_c and k_e do not have a clear linear correlation.

7.4.3. Fracture Density 0.035%

The candidate solution space for the case where fracture density is 0.035% contains diffusion coefficient values such that range of the ratio D_e/D_c is between 469 and 994 (Figure S26), with a mean value of 729. We initially provided bounds to the algorithm for this ratio of $1 \leq D_e/D_c \leq 1000$, so the atmospheric mixing model apparently favors comparatively large daytime eddy diffusivities compared to those during the collapsed state. A linear regression on $D_e = f(D_c)$ yields a slope of 9.5, with an adjusted R^2 value of 0.95. Also unsurprisingly, first-order methane loss terms k_c and k_e are inversely correlated (though to a lesser degree than in the fracture density 0.01$ case) in order to preserve mass balance in time. The range in the ratio of k_e/k_c is 1.02 to 1.66, having mean value 1.22, with the overall best scenarios in terms of error coming out of ratios close to unity. A linear regression on $k_e = f(k_c)$ yields a slope of -0.48, with an adjusted R^2 value of 0.27.

References

Adobe Inc. (2019). *Adobe Illustrator.* [Software]. Retrieved from `https://adobe.com/products/illustrator`

Carslaw, H. S., & Jaeger, J. C. (1959). *Conduction of Heat in Solids* (2nd ed.). Oxford: Clarendon Press.

Clemo, T. M., & Smith, L. (1997). A hierarchical model for solute transport in fractured media. *Water Resources Research*, *33*(8), 1763–1783.

Cooley, J. W., & Tukey, J. W. (1965). An Algorithm for the Machine Calculation of Complex Fourier Series. *Mathematics of Computation*, *19*(90), 297–301. doi: 10.2307/2003354

Geier, J. E., Lee, K., & Dershowitz, W. S. (1988). Field validation of conceptual models for fracture geometry. *Transactions of American Geophysical Union*, *69*(44), 1177.

Gough, R. V., Tolbert, M. A., McKay, C. P., & Toon, O. B. (2010). Methane adsorption on a martian soil analog: An abiogenic explanation for methane variability in the martian atmosphere. *Icarus*, *207*(1), 165–174. Retrieved from `http://dx.doi.org/10.1016/j.icarus.2009.11.030` doi: 10.1016/j.icarus.2009.11.030

Harp, D. R., Ortiz, J. P., & Stauffer, P. H. (2019). Identification of dominant gas transport frequencies during barometric pumping of fractured rock. *Scientific Reports*, *9*(1), 9537. doi: 10.1038/s41598-019-46023-z

Jones, E. G., Lineweaver, C. H., & Clarke, J. D. (2011). An extensive phase space for the potential Martian biosphere. *Astrobiology*, *11*(10), 1017–1033. doi: 10.1089/ast.2011.0660

Kronyak, R. E., Kah, L. C., Edgett, K. S., VanBommel, S. J., Thompson, L. M., Wiens, R. C., ... Nachon, M. (2019). Mineral-Filled Fractures as Indicators of Multigenerational Fluid Flow in the Pahrump Hills Member of the Murray Formation, Gale Crater, Mars. *Earth and Space Science*, *6*(2), 238–265. doi: 10.1029/2018EA000482

Lin, J. T., & McElroy, M. B. (2010). Impacts of boundary layer mixing on pollutant vertical profiles in the lower troposphere: Implications to satellite remote sensing. *Atmospheric Environment*, *44*(14), 1726–1739. Retrieved from `http://dx.doi.org/10.1016/j.atmosenv.2010.02.009` doi: 10.1016/j.atmosenv.2010.02.009

Mellon, M. T., & Phillips, R. J. (2001). Recent gullies on Mars and the source of liquid water. *Journal of Geophysical Research E: Planets*, *106*(E10), 23165–23179. doi: 10.1029/2000JE001424

Meslin, P. Y., Gough, R., Lefvre, F., & Forget, F. (2011). Little variability of methane on Mars induced by adsorption in the regolith. *Planetary and Space Science*, *59*(2-3), 247–258. doi: 10.1016/j.pss.2010.09.022

Moores, J. E., Gough, R. V., Martinez, G. M., Meslin, P. Y., Smith, C. L., Atreya, S. K., ... Webster, C. R. (2019). Methane seasonal cycle at Gale Crater on Mars consistent with regolith adsorption and diffusion. *Nature Geoscience*, *12*(5), 321–325. doi: 10.1038/s41561-019-0313-y

Newman, C. E., Gómez-Elvira, J., Marin, M., Navarro, S., Torres, J., Richardson, M. I., ... Bridges, N. T. (2017). Winds measured by the Rover Environmental Monitoring Station (REMS) during the Mars Science Laboratory (MSL) rover's Bagnold Dunes Campaign and comparison with numerical modeling using MarsWRF. *Icarus*, *291*(December 2016), 203–231. Retrieved from `http://dx.doi.org/10.1016/j.icarus.2016.12.016` doi: 10.1016/j.icarus.2016.12.016

Newman, C. E., Kahanpää, H., Richardson, M. I., Martínez, G. M., Vicente-Retortillo, A., & Lemmon, M. T. (2019). MarsWRF Convective Vortex and Dust Devil Predictions for Gale Crater Over 3

Mars Years and Comparison With MSL-REMS Observations. *Journal of Geophysical Research: Planets*, *124*(12), 3442–3468. doi: 10.1029/2019JE006082

Nilson, R. H., Peterson, E. W., Lie, K. H., Burkhard, N. R., & Hearst, J. R. (1991). Atmospheric Pumping: A Mechanism Causing Vertical Transport of Contaminated Gases Through Fractured Permeable Media. *Journal of Geophysical Research: Solid Earth*, *96*(B13), 933–948. doi: 10.2752/147597509112541

Ordonez-Etxeberria, I., Hueso, R., & Sánchez-Lavega, A. (2018). A systematic search of sudden pressure drops on Gale crater during two Martian years derived from MSL/REMS data. *Icarus*, *299*, 308–330. doi: 10.1016/j.icarus.2017.07.032

Ordóñez-Etxeberria, I., Hueso, R., & Sánchez-Lavega, A. (2020). Strong increase in dust devil activity at Gale crater on the third year of the MSL mission and suppression during the 2018 Global Dust Storm. *Icarus*, *347*(February). doi: 10.1016/j.icarus.2020.113814

Ortiz, J. P., Rajaram, H., Stauffer, P. H., Harp, D. R., Wiens, R. C., & Lewis, K. W. (2022). [SI] Barometric Pumping Through Fractured Rock: A Mechanism for Venting Deep Methane to Mars' Atmosphere. *Geophysical Research Letters*, *49*(14), 1–25. doi: 10.1029/2022GL098946

Richardson, M. I., Toigo, A. D., & Newman, C. E. (2007). PlanetWRF: A general purpose , local to global numerical model for planetary atmospheric and climate dynamics. *Journal of Geophysical Research*, *112*(E9), 1–29. doi: 10.1029/2006JE002825

Storn, R., & Price, K. (1997). Differential Evolution – A Simple and Efficient Heuristic for global Optimization over Continuous Spaces. *Journal of Global Optimization*, *11*(4), 341–359. Retrieved from `http://dx.doi.org/10.1023/A:1008202821328` doi: 10.1023/A:1008202821328

Viswanathan, G. M., Buldyrev, S. V., Havlin, S., Da Luz, M. G., Raposo, E. P., & Stanley, H. E. (1999). Optimizing the success of random searches. *Nature*, *401*(6756), 911–914. doi: 10.1038/44831

Webster, C. R., Mahaffy, P. R., Atreya, S. K., Moores, J. E., Flesch, G. J., Malespin, C., ... Navarro-Gonzalez, R. (2018a). Background levels of methane in Mars' atmosphere show strong seasonal variations. *Science*, *360*(6393), 1093–1096.

Webster, C. R., Mahaffy, P. R., Atreya, S. K., Moores, J. E., Flesch, G. J., Malespin, C., ... Vasavada, A. R. (2018b). [Supplementary Material] Background levels of methane in Mars' atmosphere show strong seasonal variations. *Science*, *360*(6393), 1093–1096. doi: 10.1126/science.aaq0131

Webster, C. R., Mahaffy, P. R., Pla-Garcia, J., Rafkin, S. C., Moores, J. E., Atreya, S. K., ... Vasavada, A. R. (2021). Day-night differences in Mars methane suggest nighttime containment at Gale crater. *Astronomy and Astrophysics*, *650*(December 2019), 1–14. doi: 10.1051/0004-6361/202040030

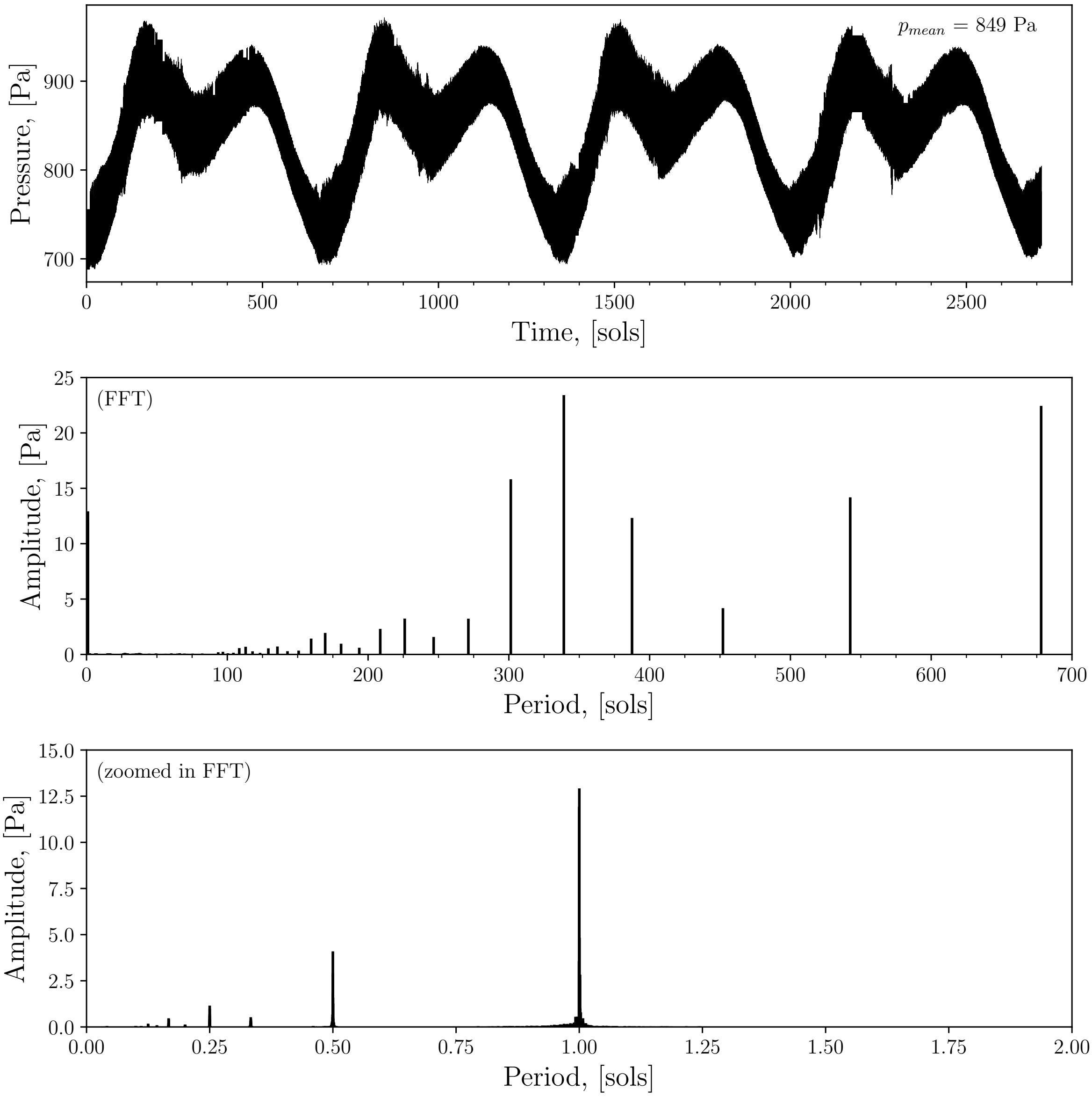

Figure S1. Spectral decomposition of the elevation-corrected barometric pressure data collected by *Curiosity* rover through mission sol 2713: (top) barometric record time series with data gaps filled using the procedure outlined previously; (middle) spectral decomposition of the barometric record into its associated amplitude/period pairs, showing the relative strength of each periodic component; (bottom) zoomed in portion of the spectral decomposition to highlight the roughly diurnal barometric component.

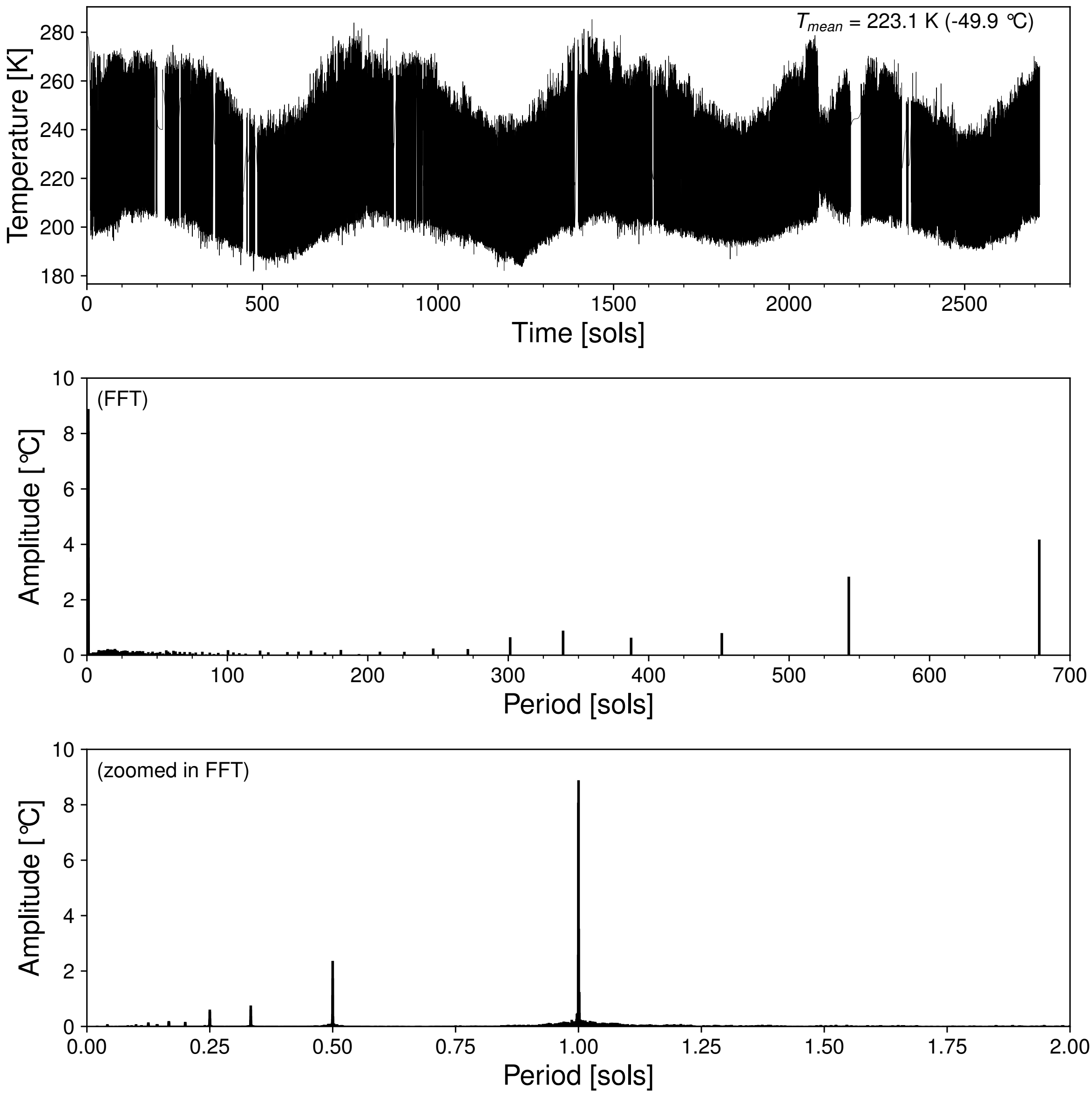

Figure S2. Spectral decomposition of the ambient temperature data collected by *Curiosity*: (top) temperature record time series; (middle) spectral decomposition of the temperature record into its associated amplitude/period pairs, showing the relative strength of each periodic component; (bottom) zoomed in portion of the spectral decomposition to highlight the roughly diurnal temperature component.

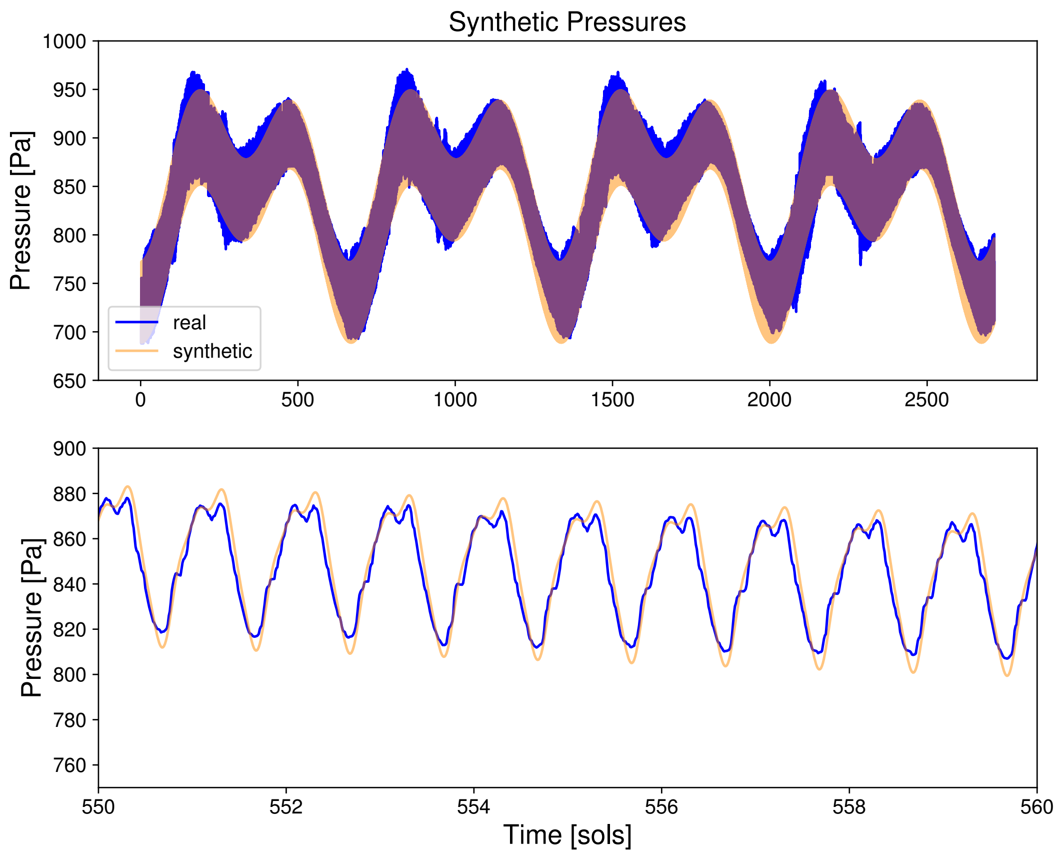

Figure S3. Generated synthetic pressures compared to elevation-corrected observed pressures for the first four Mars years of the MSL mission. (Top) The 1-year synthetic pressures repeated to match the extent of the observed pressures. (Bottom) Zooming in on a 10-sol segment of the barometric record to illustrate diurnal variations.

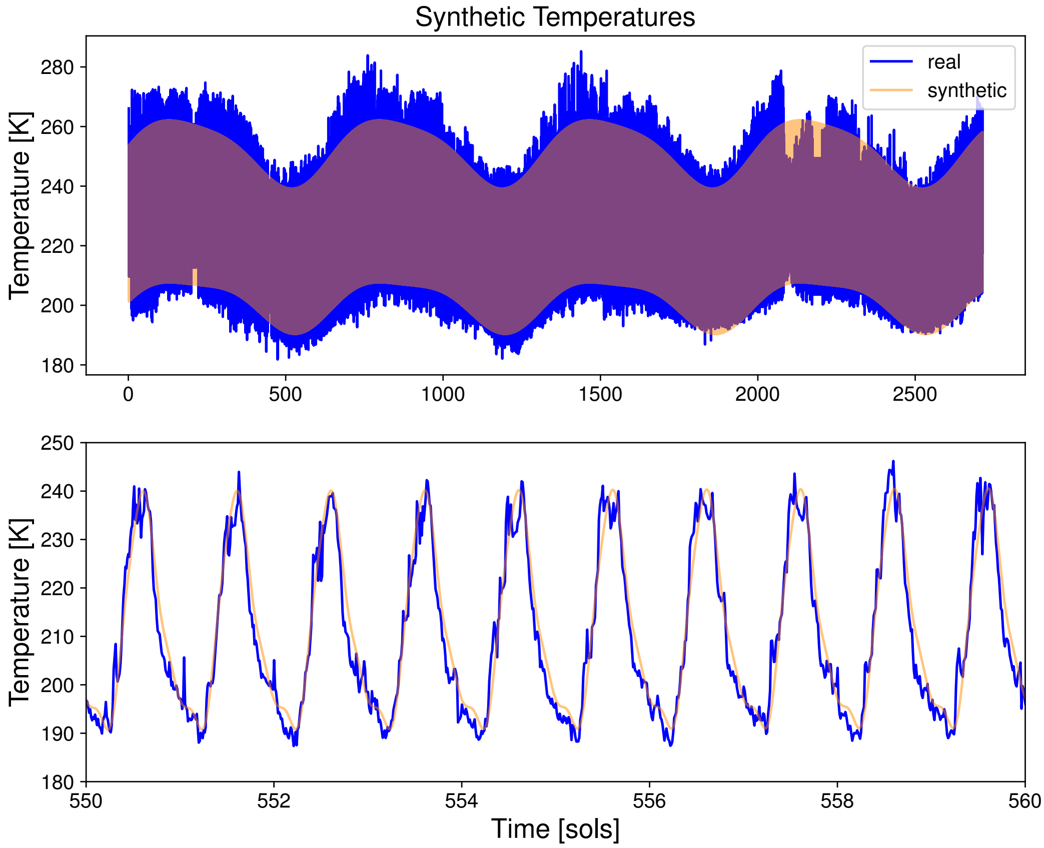

Figure S4. Generated synthetic surface temperatures compared to observed temperatures for the first four Mars years of the MSL mission. (Top) The 1-year synthetic temperatures repeated to match the extent of the observed temperatures. (Bottom) Zooming in on a 10-sol segment of the barometric record to illustrate diurnal variations.

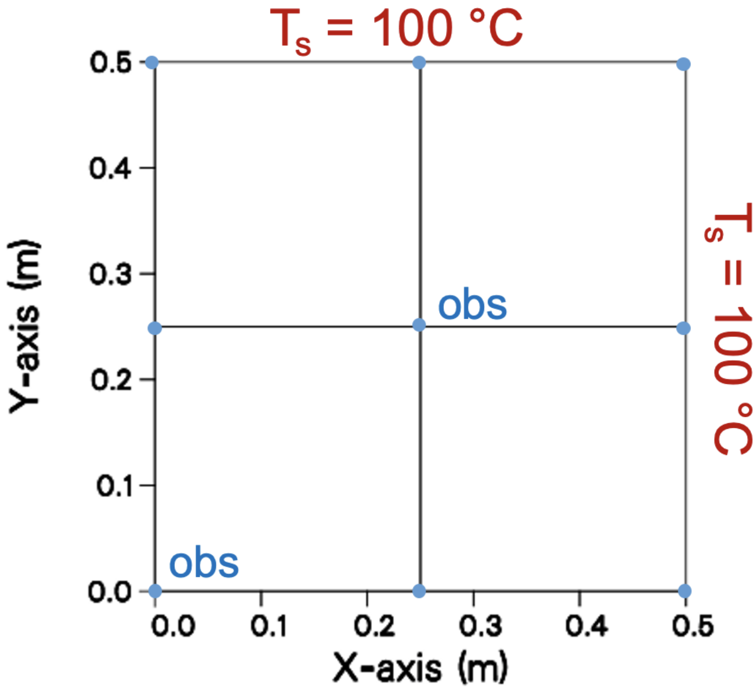

Figure S5. Schematic of the simple heat conduction verification problem set up in FEHM.

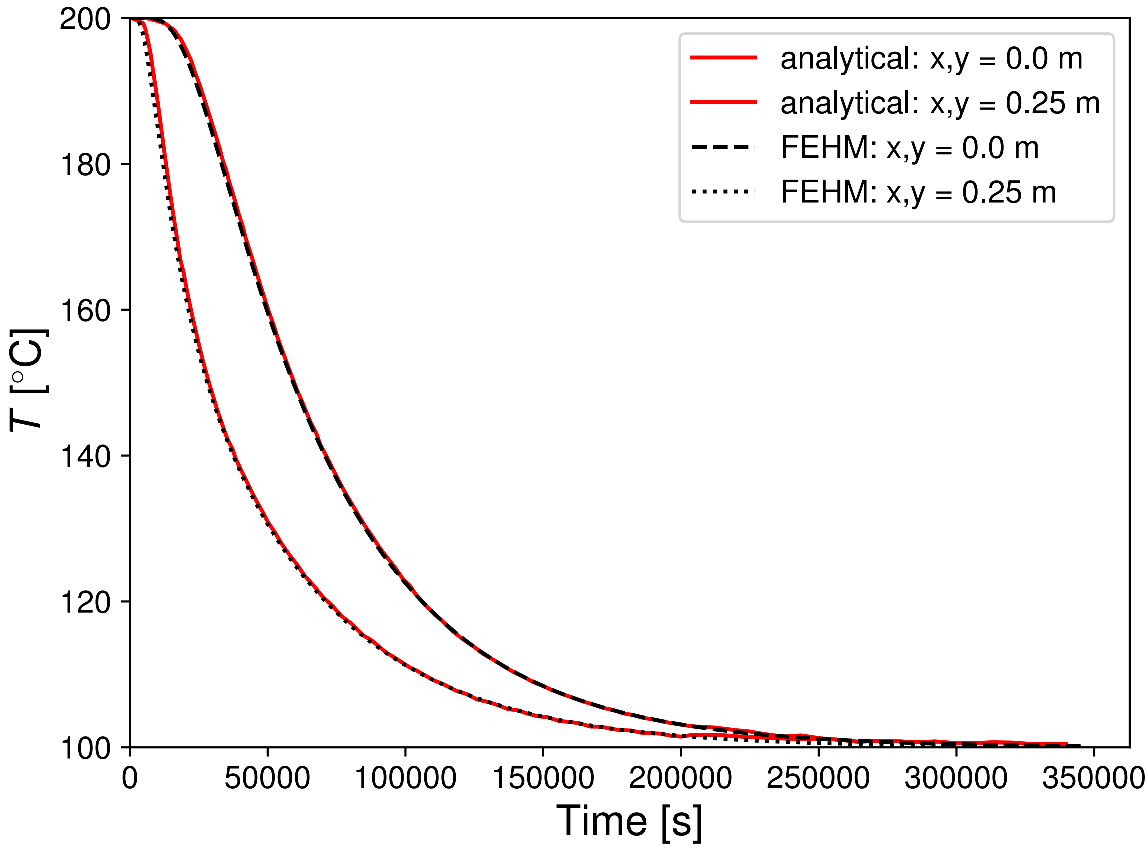

Figure S6. Results of the simulated simple heat conduction verification problem compared to the corresponding analytical solution.

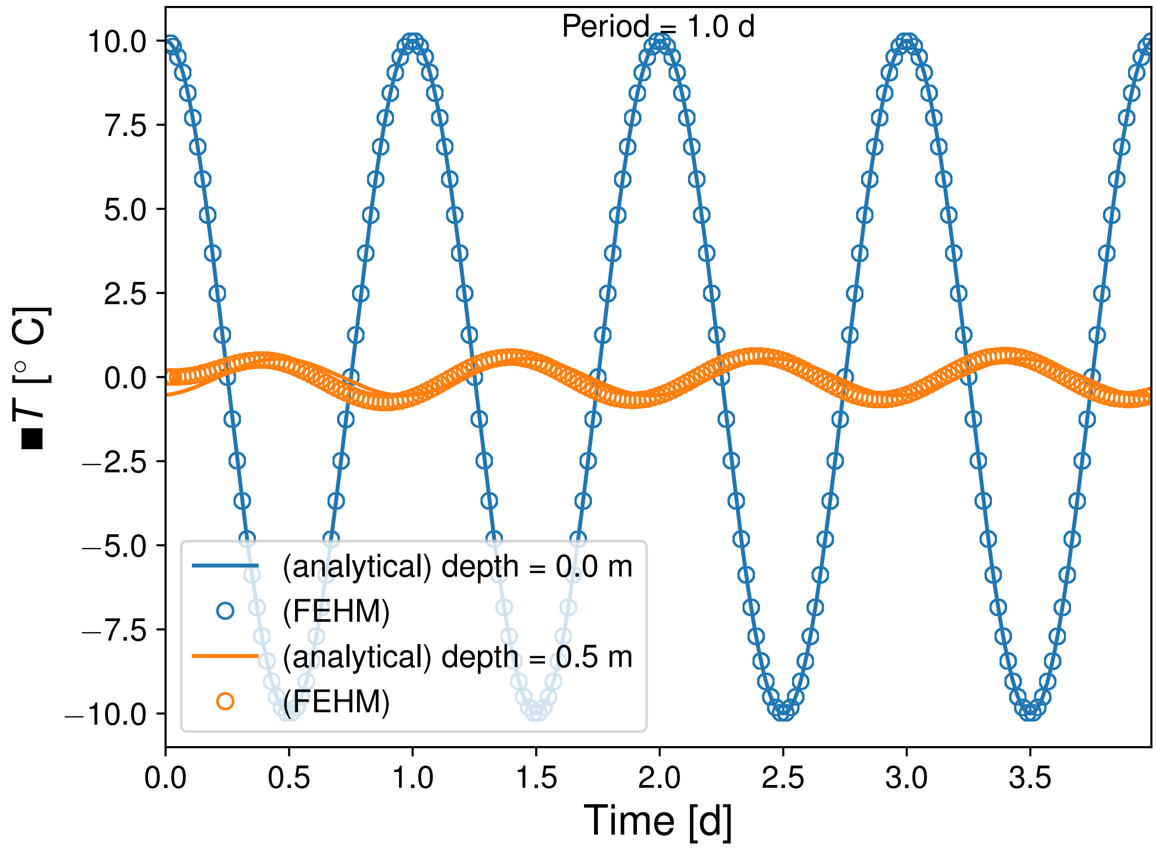

Figure S7. Comparison of simulated to analytical subsurface oscillatory thermal wave propagation.

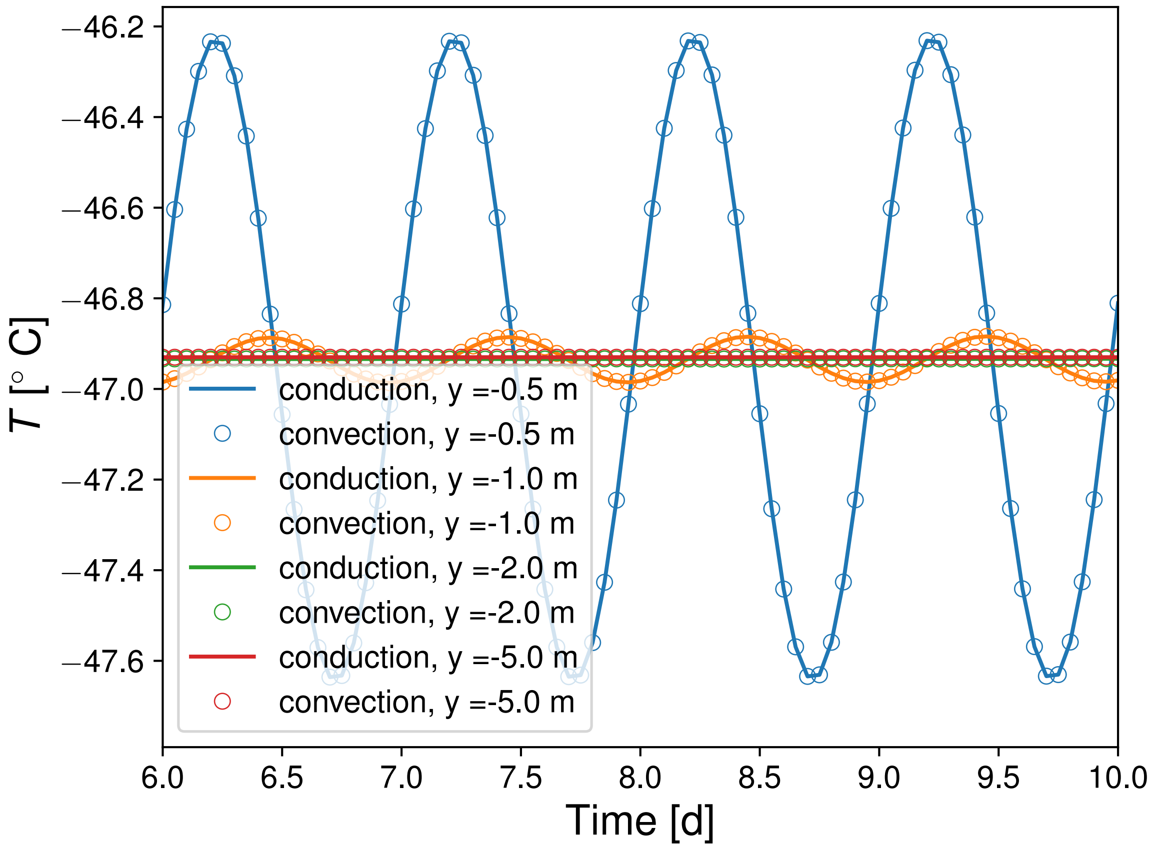

Figure S8. Comparison of subsurface temperature oscillations in purely conductive and conductive-convective regimes. The difference in subsurface temperatures is negligible due to the low density of CO_2 gas in Mars' atmosphere.

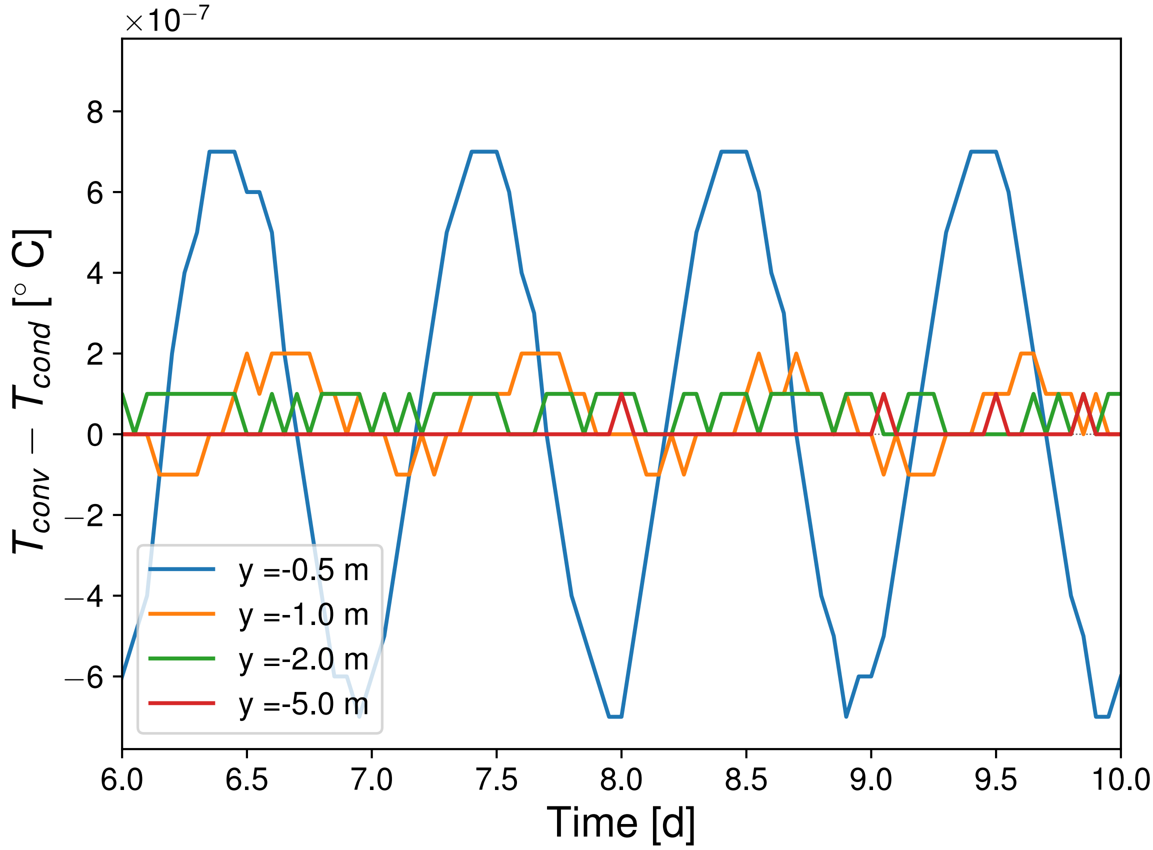

Figure S9. Difference between subsurface temperatures in time for convective and conductive heat flow using diurnal forcing. Results indicate very small differences in temperatures.

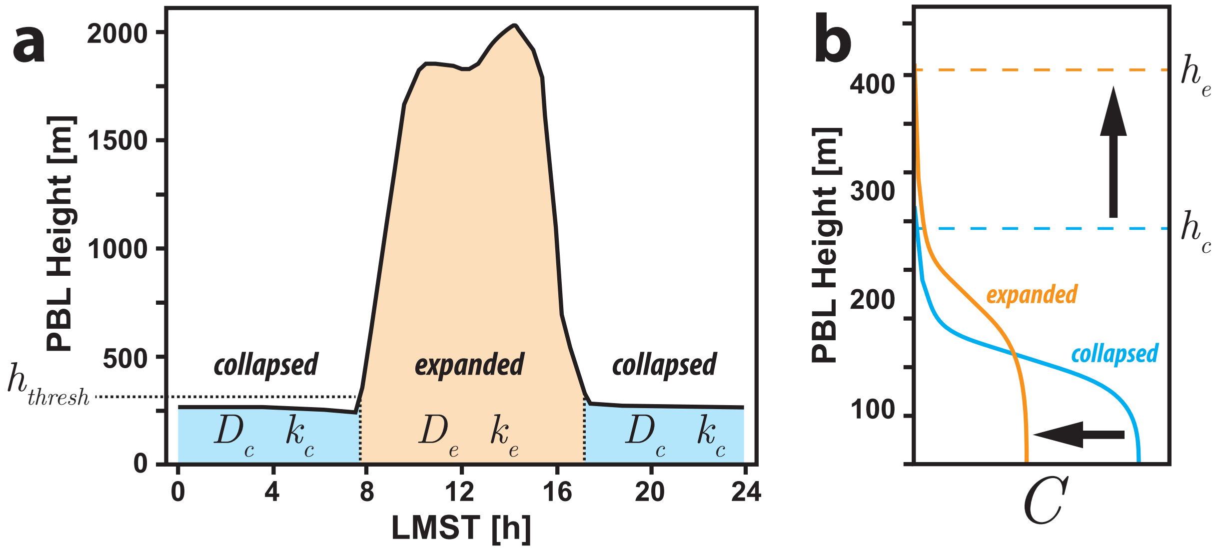

Figure S10. Schematic of the implementation of the diffusive atmospheric mixing model. (a) Delineation of the modeled atmospheric transport variables D_n and k_n based on PBL state change, where subscript n represents either c or e to indicate collapsed or expanded PBL states, respectively. PBL time series shown is representative of N. Summer, and varies throughout the Mars year in 30° L_s increments according to Newman et al. (2017). Transition from collapsed to expanded-state conditions is demarcated by PBL height cross threshold column height h_{thresh}. (b) Illustration showing the transition of initial state of the vertical concentration profile $C(z)$ in the model for an expanding PBL column (i.e., going from collapsed to expanded state). Total CH_4 mass in the atmospheric column is conserved during this transition.

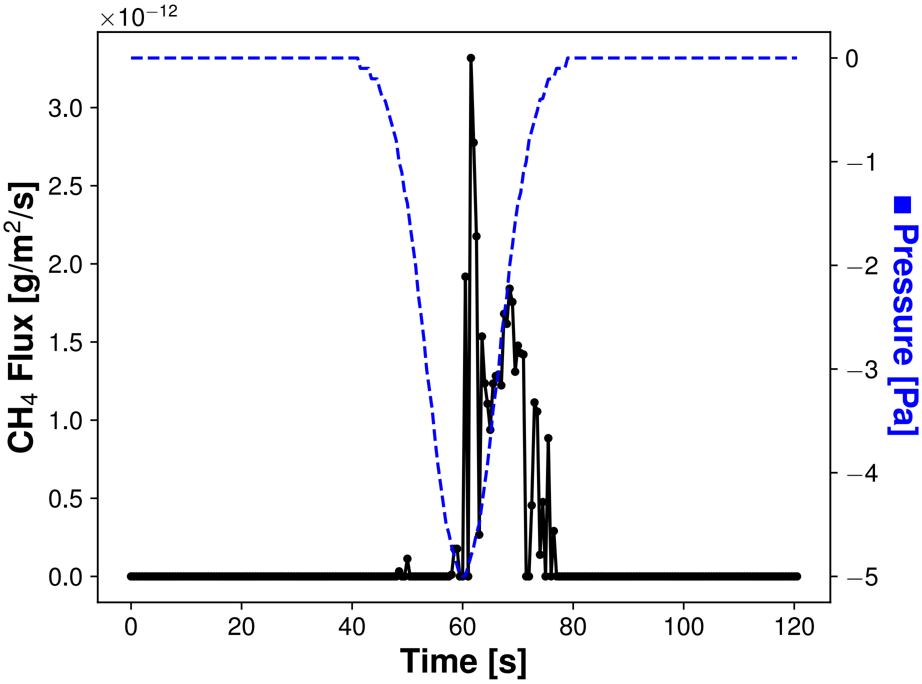

Figure S11. Surface methane fluxes induced by a large dust devil detected by MSL-REMS. Duration of the pressure drop was 25 s, with a drop in pressure (ΔP) of 5 Pa.

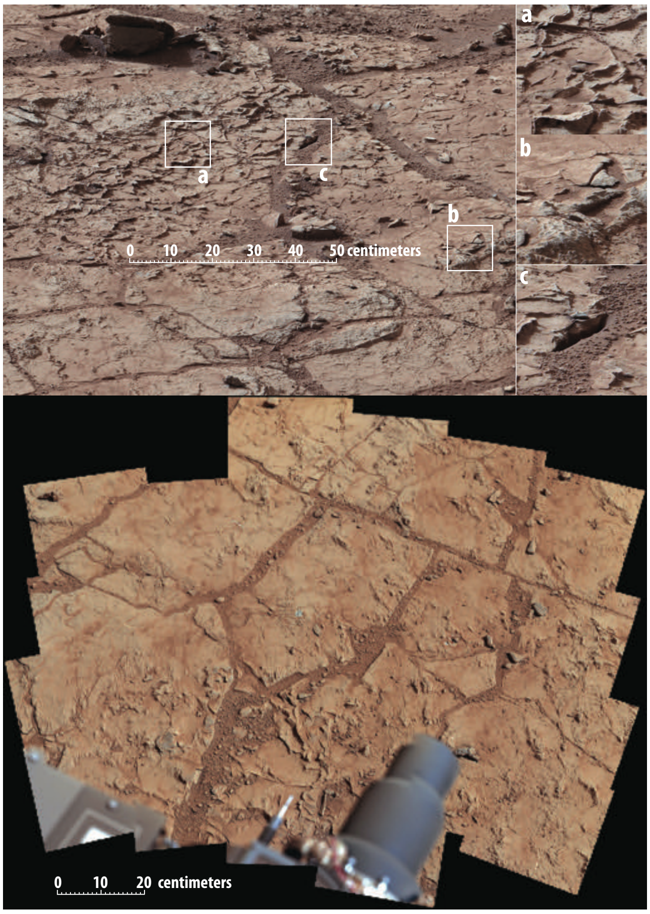

Figure S12. Examples of macroscopic surface fractures at Gale crater photographed by *Curiosity*'s Mastcam. (Top) A view of a patch of veined, flat-lying rock selected as the first drilling site for *Curiosity*, taken on sol 153 in the Yellowknife Bay geologic formation. Three boxes, each about 10 cm across, designate enlargements illustrating attributes of the area: (a) a high concentration of ridge-like veins protruding above the surface, with some veins having two walls and an eroded interior; (b) a horizontal discontinuity a few centimeters beneath the surface, which may be a bed, a fracture, or a horizontal vein; (c) a hole developed in the sand overlying a fracture, which implies a shallow infiltration of sand down into the fracture system. (Bottom) mosaic of the area, called "John Klein", where the rover performed its first sample drilling. Surface expression of these fractures show apertures on the scale of 1-2 cm, with most of the fracture volume occupied by unconsolidated material filling. Image credits: (top) NASA/JPL-Caltech/MSSS; (bottom) NASA/JPL-Caltech/MSSS.

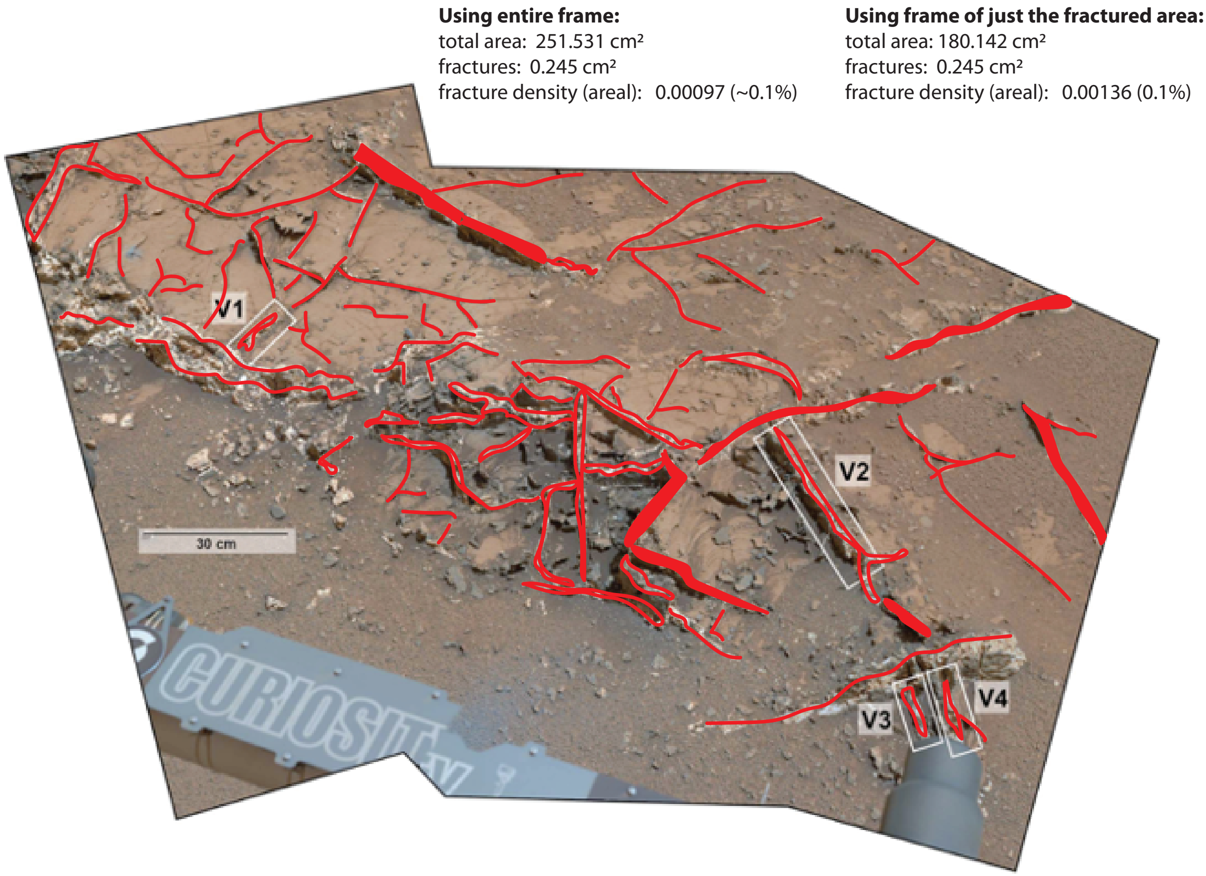

Figure S13. Fracture trace method used to approximate the areal "fracture density" of Mars' subsurface, applied to a Mastcam-34 mosaic (Kronyak et al., 2019) of the Garden City vein (mineral-filled fracture) complex at Gale crater. Centimeter-thick sandwich veins comprise the positive-relief intersecting network. Note that annotated areal dimensions are based on screen dimensions rather than the physical outcrop.

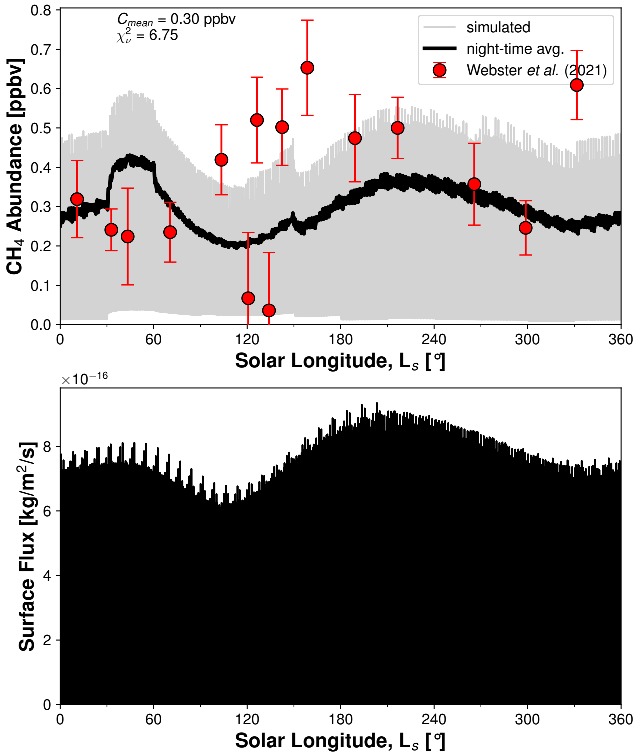

Figure S14. “Best” scenario atmospheric methane abundance and surface flux for scenario with fracture density 0.0%. (Top) Comparison of simulated (gray) to measured (circles) atmospheric methane abundance values plotted against solar longitude, L_s [°]. Night-time averages of the simulated abundance (thick black line) is plotted to aid visualization because of the large diurnal variations present (gray band). Measured abundances are from Webster et al. (2021). Note that some measurements were taken in different Mars years. (Bottom) Surface methane fluxes generated by barometric pumping over the same time period. These surface fluxes are input to the coupled atmospheric mixing model to generate the atmospheric mixing ratios above.

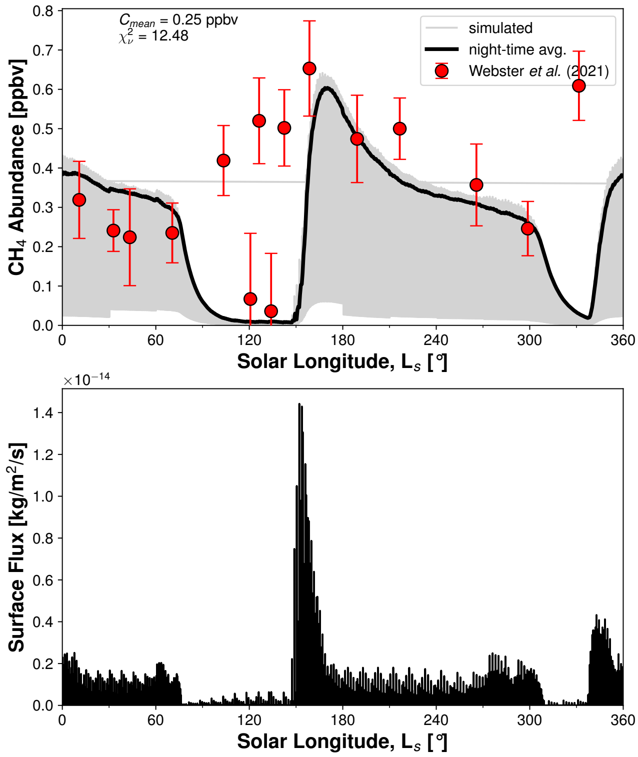

Figure S15. Same as Figure S14, but for fracture density 0.001%.

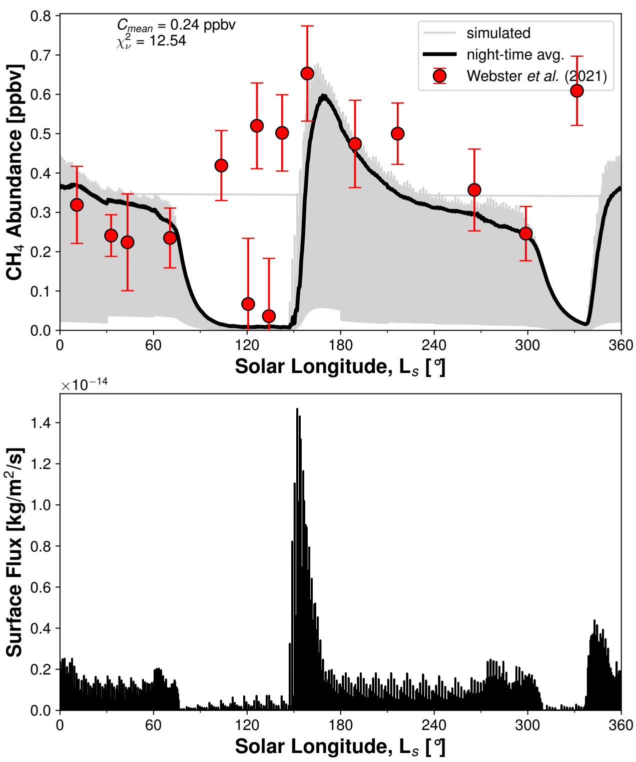

Figure S16. Same as Figure S14, but for fracture density 0.005%.

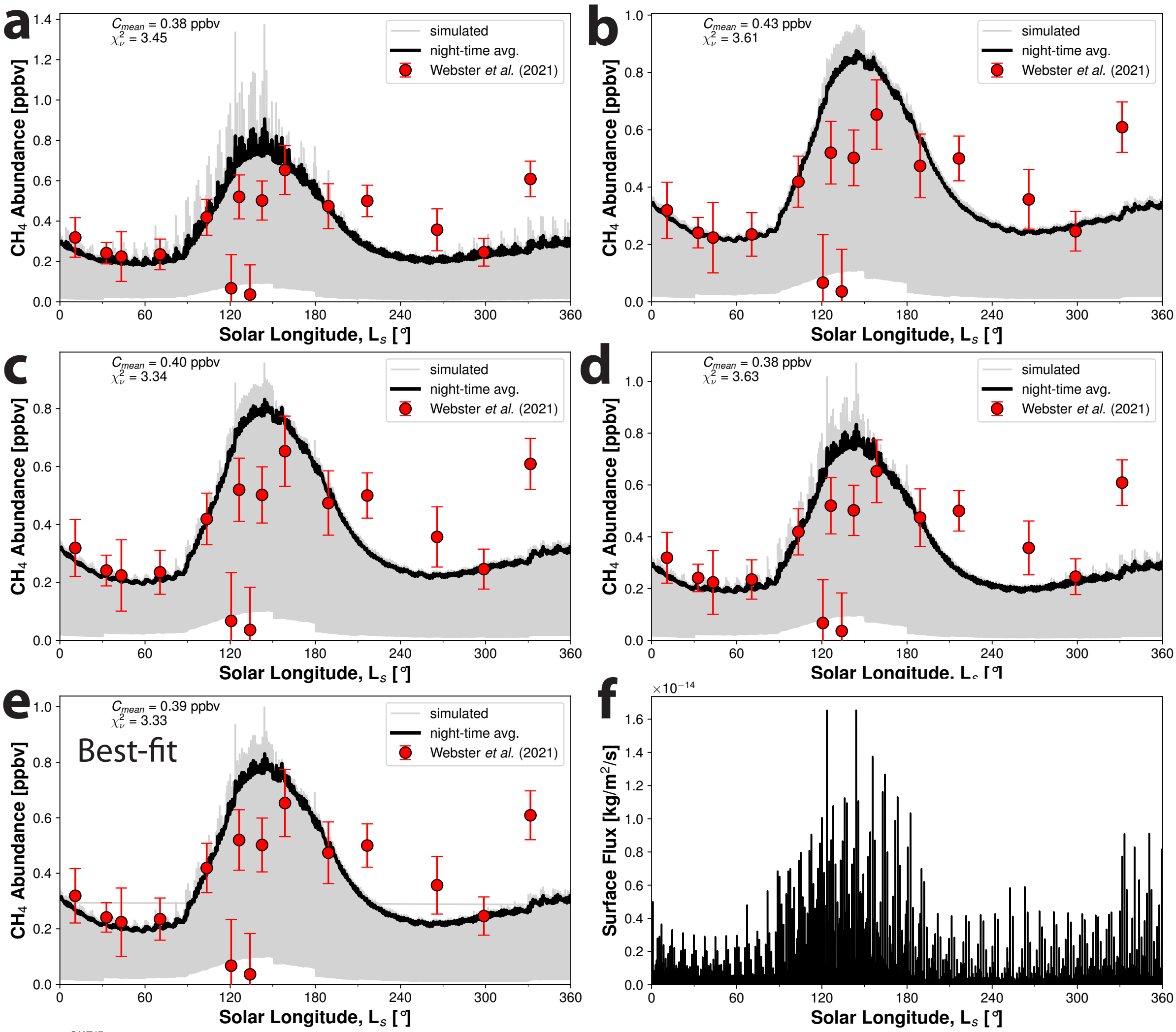

Figure S17. Composite of atmospheric methane abundance simulations for end-member scenarios analyzed for the case with fracture density 0.020%. Panel letters **a-d** correspond to lettering of atmospheric transport parameter end-member scenarios. Panel **e** is the "best" fitting scenario, and panel **f** is the surface methane flux. Comparison of simulated (gray) to measured (circles) atmospheric methane abundance values plotted against solar longitude, L_s [°]. Night-time averages of the simulated abundance (thick black line) is plotted to aid visualization because of the large diurnal variations present (gray band). Measured abundances are from Webster et al. (2021). Note that some measurements were collected in different Mars years.

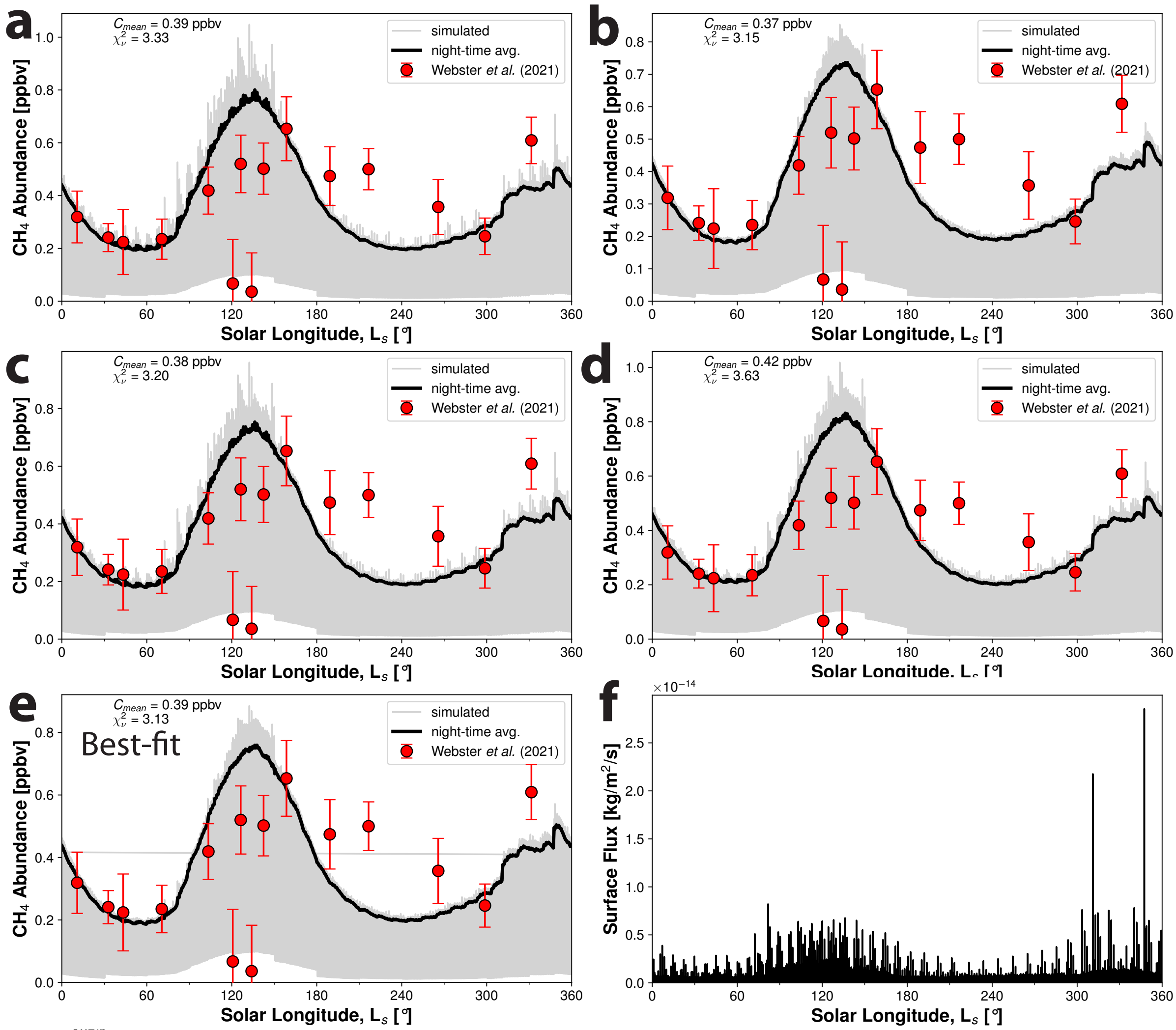

Figure S18. Same as in Figure S17, but for the case with fracture density 0.035%.

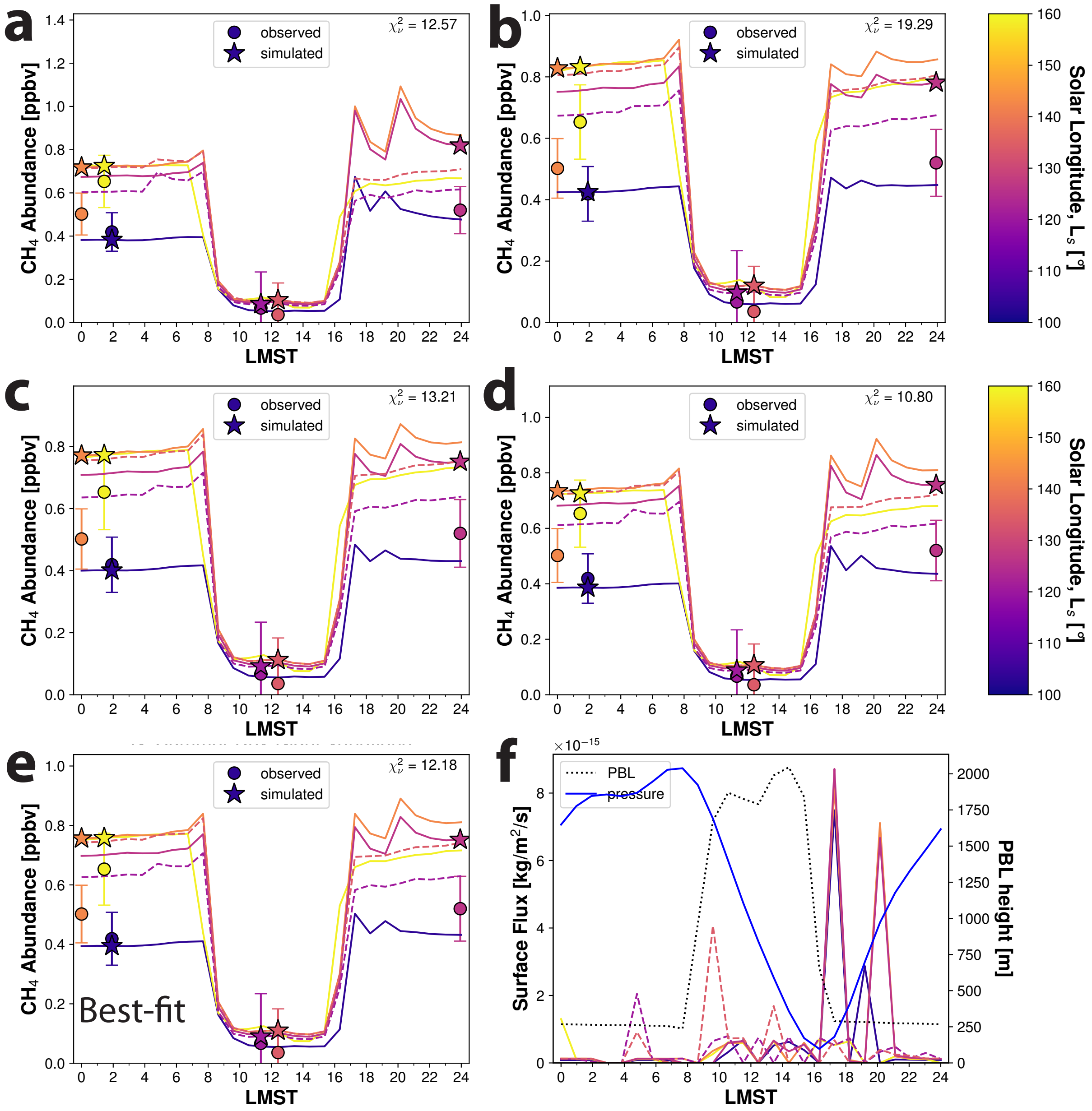

Figure S19. Composite of atmospheric mixing end-member scenarios simulating atmospheric methane abundance for the case with fracture density 0.020%. Panels **a-e** compare simulated (stars, lines) to measured (circles) atmospheric abundance values in local time, LMST, for Northern Summer, which highlights the day-night difference in abundance largely caused by the elevated planetary boundary layer (PBL) height h_{PBL}. Simulated abundances of the sols with non-detections are indicated by dashed lines. Measured abundances from Webster et al. (2021). Note that all measurements were taken on different sols and, in some cases, different Mars years, with the solar longitude, L_s [°] of the measurement indicated on the plot by its color. Panel letters **a-d** correspond to lettering of end-member scenarios. Panel **e** is the "best" fitting scenario, and panel **f** is the surface methane flux. Surface flux in local time (solid and dashed lines as above) plotted

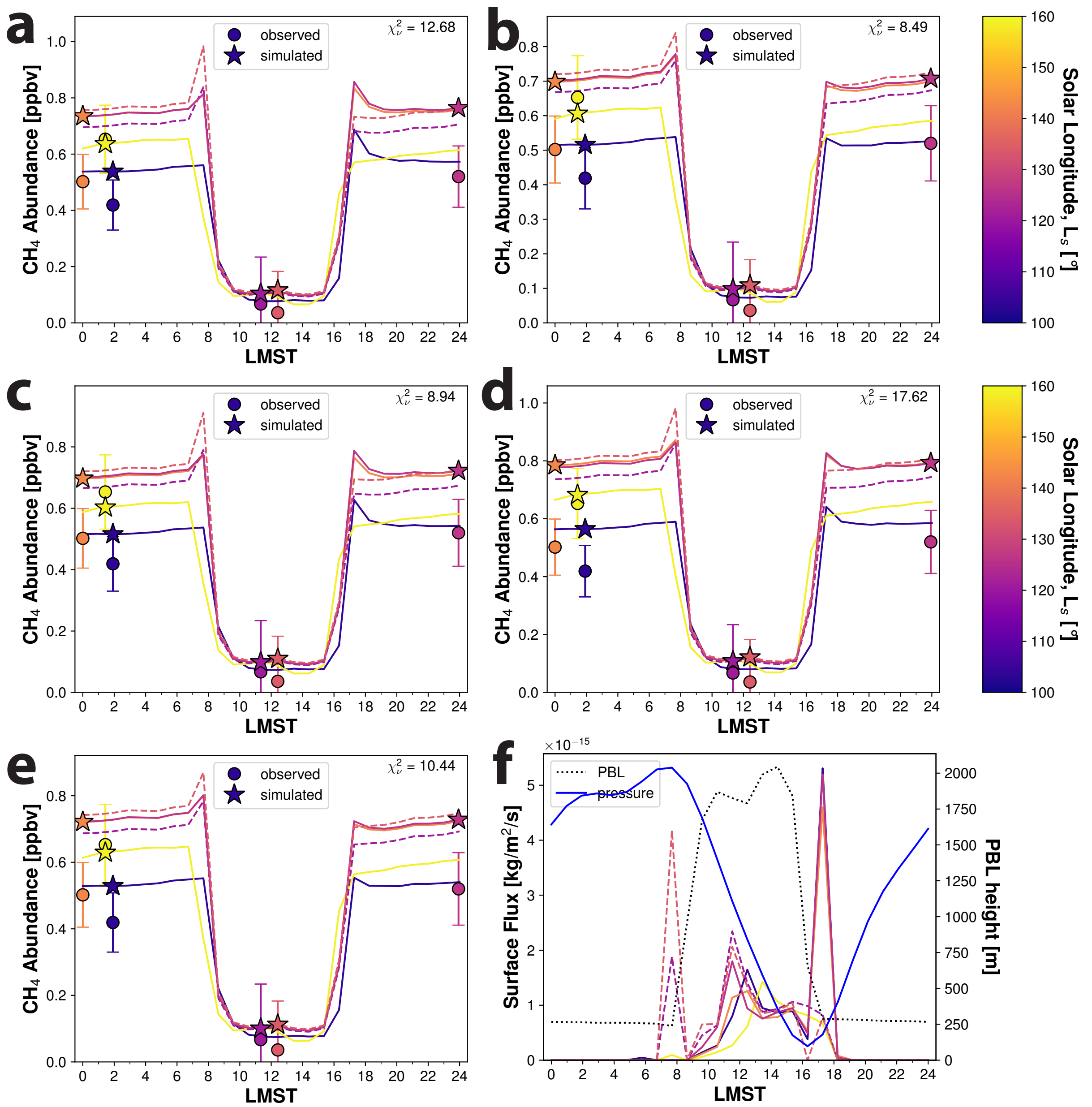

Figure S20. Same as in Figure S19, but for the case with fracture density 0.035%.

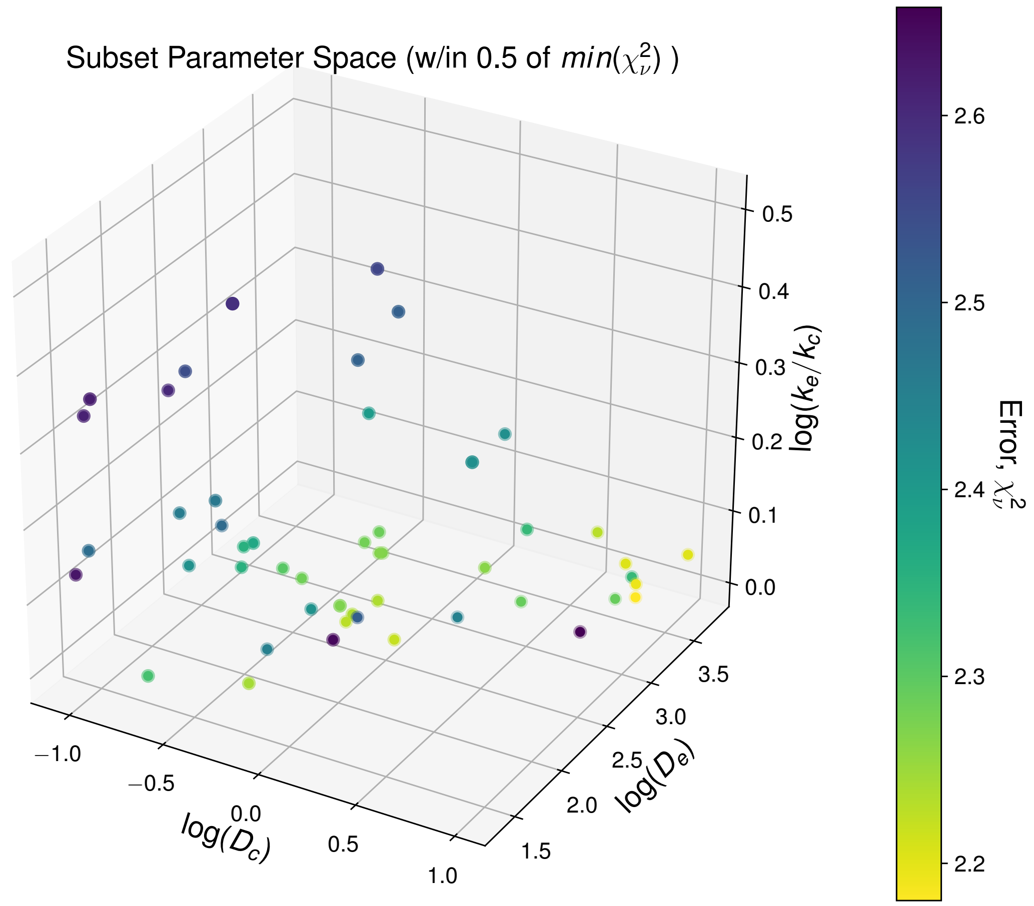

Figure S21. Candidate solution parameter space for the case with fracture density 0.010%.

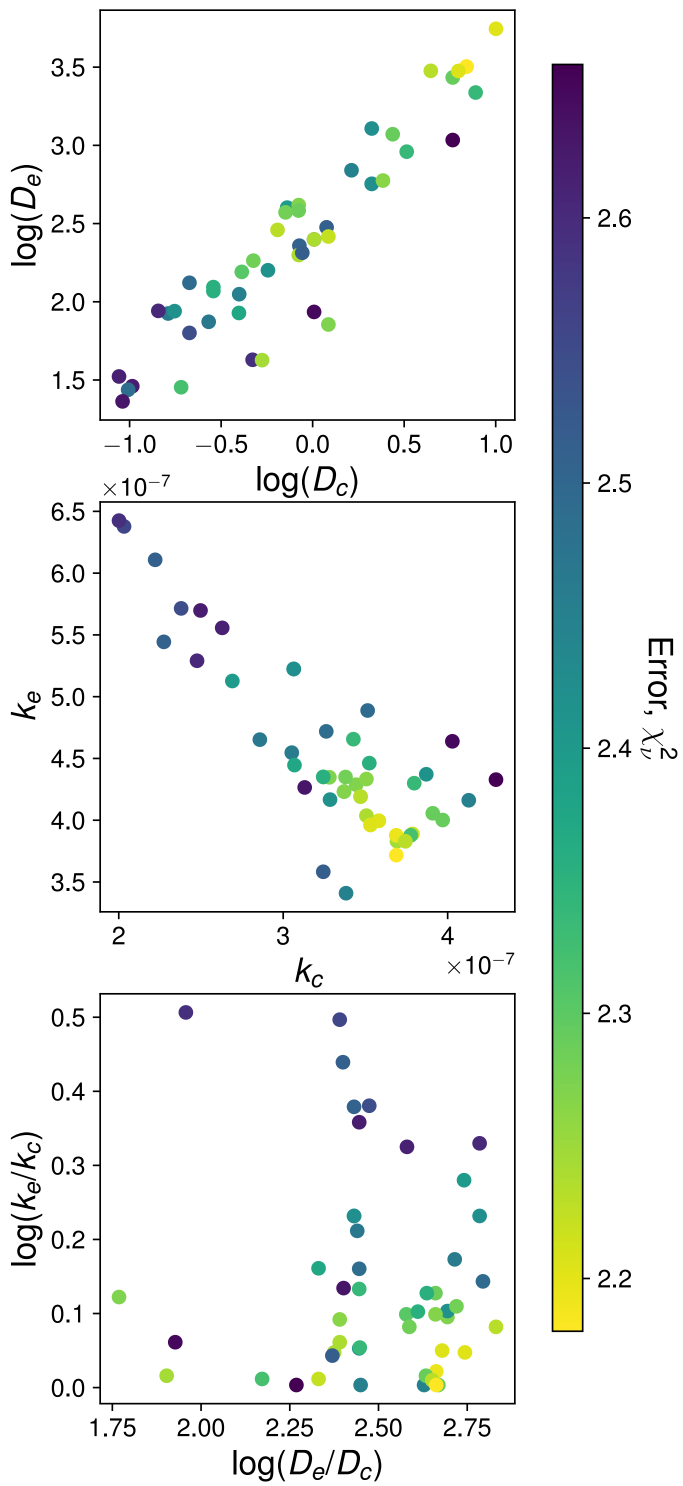

Figure S22. Comparison of individual atmospheric mixing parameters within the candidate solution parameter space for fracture density 0.010%.

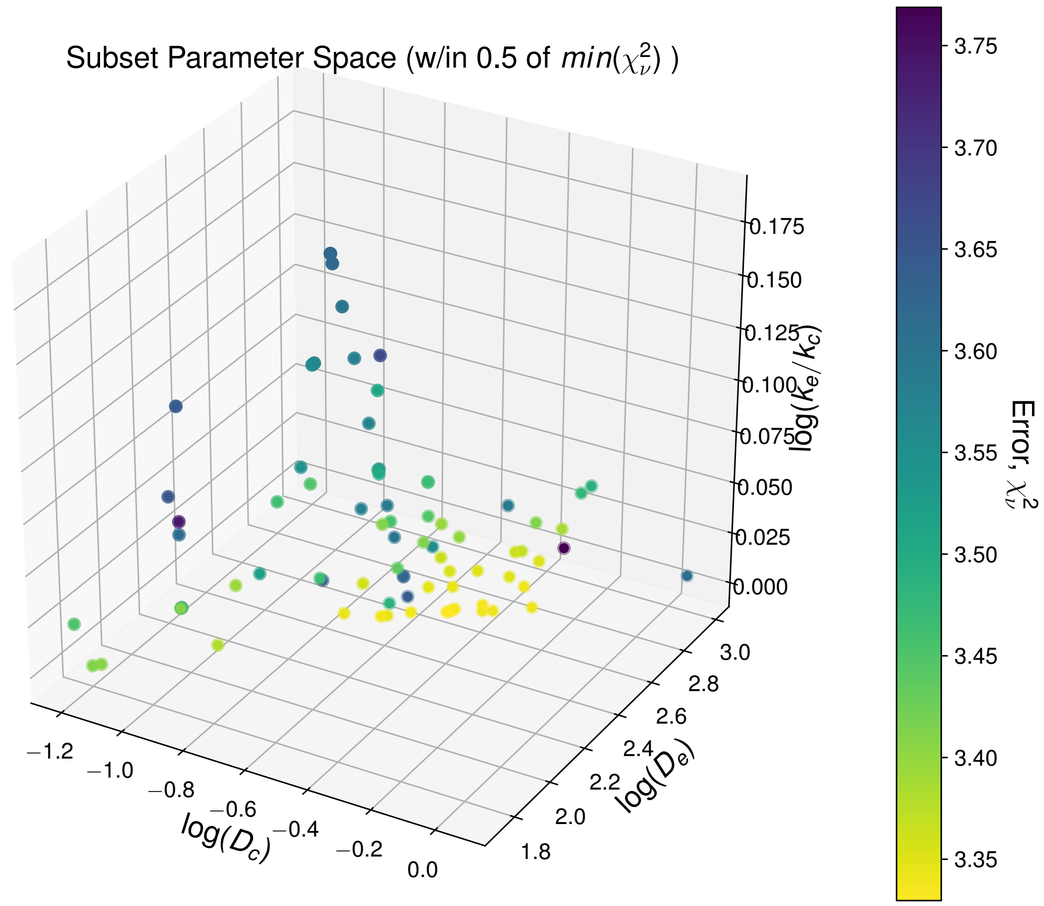

Figure S23. Candidate solution parameter space for the case with fracture density 0.020%.

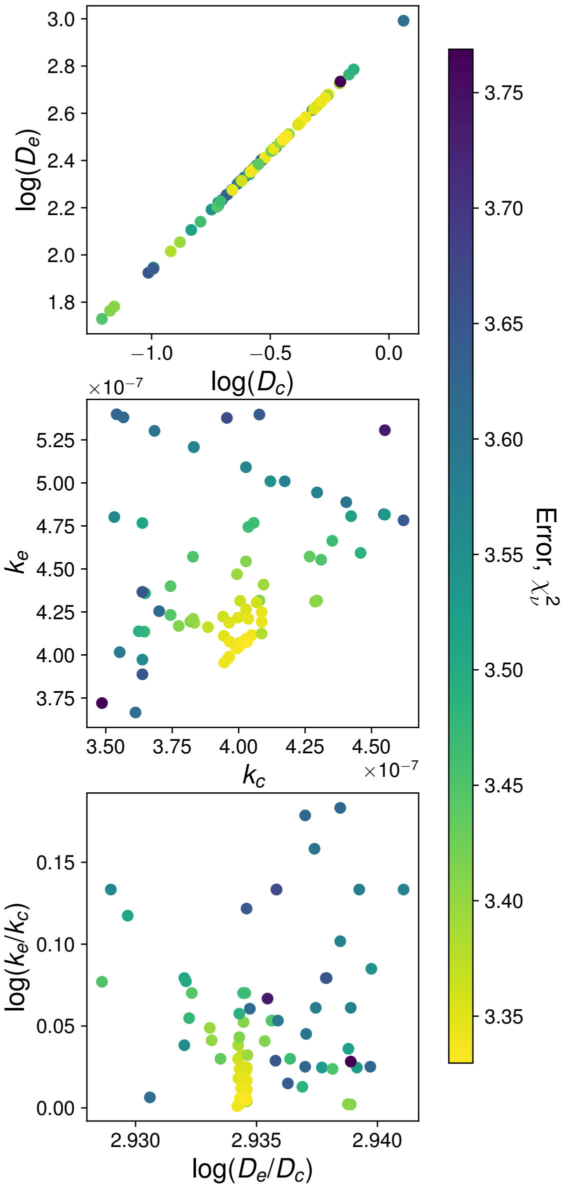

Figure S24. Comparison of individual atmospheric mixing parameters within the candidate solution parameter space for fracture density 0.020%.

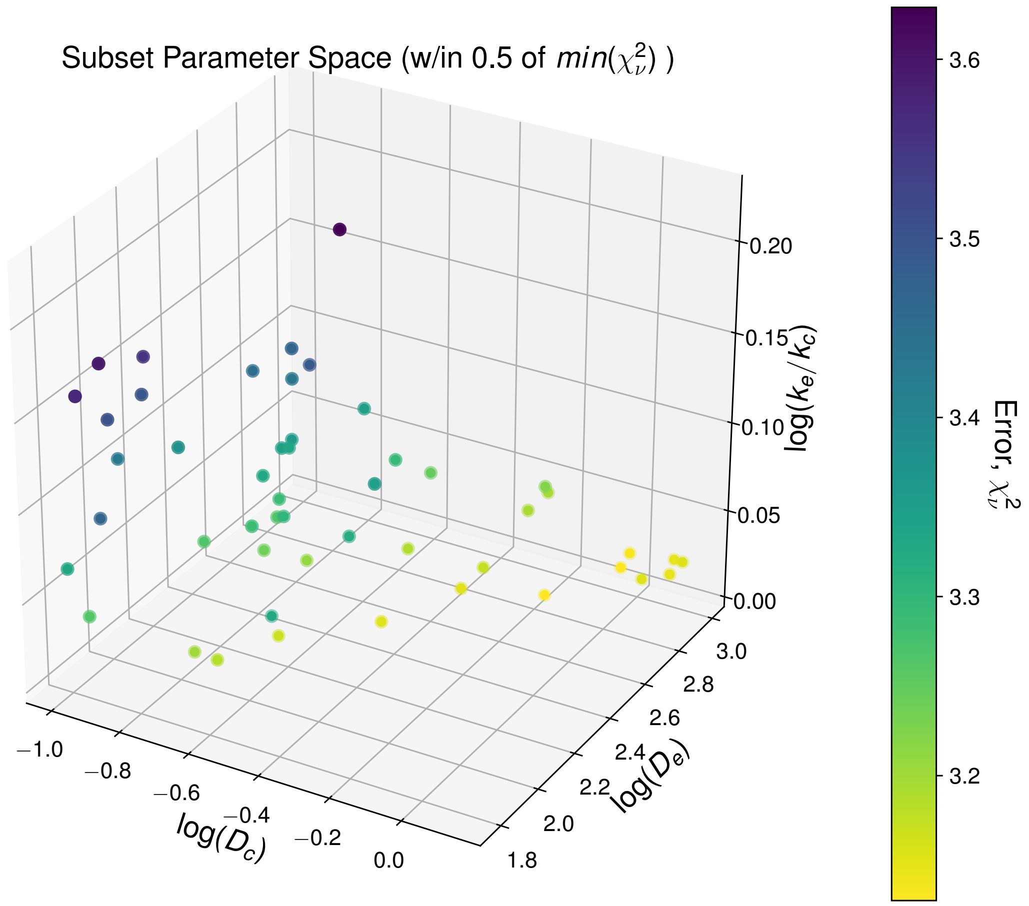

Figure S25. Candidate solution parameter space for the case with fracture density 0.035%.

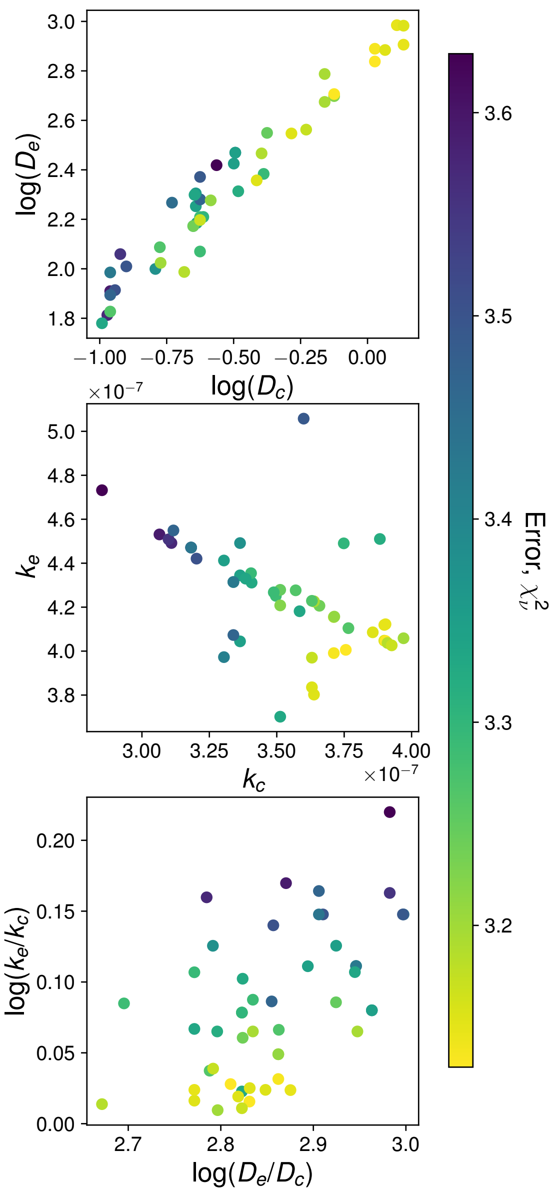

Figure S26. Comparison of individual atmospheric mixing parameters within the candidate solution parameter space for fracture density 0.035%.